Characterizing Nanoparticle Interactions at the Cellular Membrane

By

Arielle Christen Mensch

A dissertation submitted in partial fulfillment of

the requirements for the degree of

Doctor of Philosophy

(Chemistry)

at the

UNIVERSITY OF WISCONSIN-MADISON

2017

Date of final oral examination: 10/13/2017

The dissertation is approved by the following members of the Final Oral Committee:

Robert J. Hamers, Professor, Chemistry
Joel A. Pedersen, Professor, Soil Science
Qiang Cui, Professor, Chemistry
Silvia Cavagnero, Professor, Chemistry
Galya Orr, Senior Research Scientist-Team Lead, Pacific Northwest National Laboratory

Characterizing Nanoparticle Interactions at the Cellular Membrane

Arielle Christen Mensch

Under the supervision of Professor Robert J. Hamers

University of Wisconsin – Madison

Abstract

As the use of nanotechnology continues to rise, the release of engineered nanomaterials into the environment becomes inevitable. A need exists to understand the implications of engineered nanomaterials and to develop sustainable alternatives as adverse impacts are uncovered. In order to reduce any negative impacts of nanomaterials and exploit any beneficial impacts, the field of environmental nanotechnology must aim to understand the behavior of nanomaterials in complex environments through the use of *in situ* analytical methods and utilize model systems (both in terms of nanomaterials and organisms) to determine the chemical factors that drive nanoparticle behavior. The work presented here focuses on the cellular membrane, which is hypothesized to be the first point of contact between a nanomaterial and an organism. The characterization of different models cellular membranes and the characterization of nanoparticle interactions at these model membranes are presented.

First, we investigated the impact of natural organic matter (NOM), which is found ubiquitously in the environment, on the interactions between polymer wrapped diamond nanoparticles (DNPs) and lipopolysaccharide-containing supported lipid bilayers, a model for Gram-negative bacteria cell membranes. To demonstrate the relevance of our model system we extended our study to include experiments using a Gram-negative bacterium, *Shewanella oneidensis* MR-1.We found that NOM impacted the hydrodynamic and electrokinetic properties of DNPs in a concentration dependent manner, which altered subsequent interactions with both model and actual biological membranes. Our results demonstrate that the effects of NOM coronas

on nanoparticle properties and interactions with biological surfaces can depend on the relative amounts of NOM and nanoparticles.

We then examined the impact of polymer wrapped quantum dots (QDs) on supported lipid bilayers containing important biomolecules found in the outer membrane of eukaryotic cells (cholesterol and sphingomyelin). We used *in situ* analytical methods to study these interactions in real time and found that the QDs caused structural changes to the bilayers studied. Quartz crystal microbalance with dissipation monitoring coupled with nanoplasmonic sensing revealed favorable interaction between the QDs and the bilayers. Increases in dissipation and apparent mass gains upon rinse suggested structural rearrangement was occurring. Time-lapsed atomic force microscopy confirmed this hypothesis and revealed the disappearance of phase-segregated domains upon interaction with the QDs. Our results demonstrate the importance of using complementary *in situ* analytical methods to understand the complex interactions that occur at the cellular membrane.

We next demonstrate the powerful capabilities of atomic force microscopy for imaging and characterizing biological membranes. We investigate the impact of the substrate in the formation and characteristics of phase-segregated domains in supported lipid bilayers. We considered commonly used substrates in different analytical techniques (e.g., mica, silica, and glass). We discussed the importance of considering the substrate in drawing conclusions across different techniques. We also demonstrated the spatial and temporal correlation of atomic force and fluorescence microscopy.

Finally, we extended our work using atomic force microscopy and developed a protocol to image and characterize the mechanical properties of fixed and live rainbow trout (*Oncorhynchus mykiss*) gill epithelial cells. We discussed various experimental variables such as instrumental

parameters, type of AFM probe used, and the confluency of the cells on the substrate. We found that the ideal imaging conditions included using an AFM probe with a low spring constant and relatively dull tip, working with cells grown to ~75% confluency, and scanning at low speeds, high amplitudes, and minimal forces. We showed that fixed trout gill cells had an increased height and modulus value as compared to live cells. This work demonstrated the first example of AFM imaging and mechanical mapping on either fixed or live trout gill cells and set a protocol to examine the impacts of different stressors, such as nanomaterials, on trout gill cells.

.

Acknowledgments

Well, deep down I'm not sure I can say that I ever thought the day would come where I finally "finished" school. But hey – I did it! However, there is no way I could have done this alone. I am forever indebted to all of my wonderful family, friends, mentors, mentees, and colleagues who have all played a crucial role in getting me where I am today.

First and foremost, to my family – mom, dad, Jordan, and Cole. Your continued support and love drives me every day. I miss you all terribly, but the Facetimes, text message chains, and visits push me to do my best and I know you've all been there rooting for me. To my extended family – your love and support definitely doesn't go unnoticed. I love you all.

To Bob thank you for allowing me to be a part of the Hamers group and part of the CSN. Thank you for your support and guidance, and for providing me the freedom to tinker in the lab. To Joel thank you for your experimental advice, letting me use your instruments, and your mentorship. I appreciate all of the feedback and discussions. To QC thanks for being on my committee since TBO, your comments and questions are always insightful and fun. To Silvia thank you for serving on my committee. To Galya thank you for all of the support and letting me conduct research at PNNL – I look forward to working with you over the next couple of years!

To all the great teachers and mentors I've had throughout my journey – know that you're an inspiration and drive students to accomplish things they never knew they could. To Ms. Phinney-Foreman – thank you for sparking my interest in chemistry way back when. Your passion and excitement for both chemistry and education has definitely never been forgotten. To Mrs. Talada, Mrs. Stevens, Mrs. Gray, Mrs. Pan, and Mrs. Zeller you have inspired so many students to greatness all while providing laughs and great memories along the way. To Coach Gavich the life lessons you provided have guided me to this point. To the chemistry faculty at St. John Fisher College – Dr. Lantzky, Dr. Chichester, Dr. Kimaru, Dr. Piccolo, Dr. Walczak, Dr. Douglas, and Dr. Kraft – I could never thank you enough for the education and research experience you provided. The support and guidance from a small school definitely helps to shape the lives of many, never forget the positive impact you've had on so many.

To the Hamers (and Pedersen) group – past and present – you all made/make coming to lab fun. To Becca, Jamie, (B)Linghong, Caroline, and Mercedes thanks for making the early years easier. To Marco, Tom, and Eric thanks for being great mentors and more importantly, great friends. Your insights and guidance will never be forgotten. To office 3357 ('12-'17) you all are the best. The memories we've shared in this office are unforgettable and the

friendships we've made are irreplaceable. Keep doing great things and being great people. To my cohort – Laura, Margy, and Mimi – through the ups and downs, we did this together and I 100% could not have done it without you. To Liz and Zack keep morale up and the office 3357 vibes alive. To Alex thank you for being my favorite Kiwi. Your positive outlook on life, great sense of humor, and willingness to share Christmas with my family are unforgettable. To the rest of the Hamers group keep striving for greatness, but also remember to have some fun. To Lindy and Matt may you never forget your ticket to ride, find your skull crack or missing teeth, forget that it's Jonah's turn, or choose pizza other than Pizza Di's. Your friendship has meant more than you know. I wish you both the best in everything. To Matthew I'm glad we got to TA analytical together our first year and be friends through it all. To the tailgating crew, game days are some of my favorite memories. You all are great.

To my Center for Sustainable Nanotechnology collaborators, the unique and diverse expertise you all provide is extraordinary. I'm humbled and honored to be part of such an amazing collaboration. The science is obviously great, but the people are even better. I've really enjoyed my time working with and getting to know all of you. To Lee Bishop and Miriam Krause thank you for your education/outreach efforts and providing me an opportunity to learn how to edit and write blogs. To Mike Schwartz the passion and excitement you have for science is contagious. I appreciate all of the great science discussions we've had. To the breakfast club, keep it going, it's worth it. You all are great.

For experimental support in this work I must thank Rodrigo Tapia Hernandez, Joshua Kuether, Dr. Marco Torelli, Joe Buchman, Autumn Qiu, Kyoungtea Kim, Isabel Foreman-Ortiz, Dr. Eric Melby, Dr. Tom Kuech, and Dehong Hu. To all the undergrads I've had the opportunity to either mentor or work with, your efforts are much appreciated and I wish you all the best. Steve Meyers in the machine shop provided countless flow cells and good discussions. To Sue thank you for all the work you do, know that your efforts are always appreciated. To Mike Bradley I always look forward to shipping items and having a good laugh with you. To Chad thanks for dealing with all of my constant requests. You all, among many, many others truly keep this department running smoothly.

To Jack, thanks for being my best friend through all of this. I can't imagine this process without you by my side. Thanks for SnuggleFest 2017 and all of the other memories we've shared. I look forward to seeing what our future brings.

Table of Contents

Chapter 1: Background and Introduction

"Experience is the teacher of all things" – Julius Caesar (c. 52 B.C.)

History has shown that the uninformed release of materials may have detrimental consequences on the environment and on human health. One example is the use of 1, 1, 1-trichloro-2,2,-bis(4-chlorophenyl) ethane (more commonly known as DDT); an insecticide used on crops and for disease control from 1945 until its ban by the United States Environmental Protection Agency in 1972.[1] While it had many benefits as an insecticide, many adverse effects were uncovered after its use and release into the environment. It was found to bioaccumulate in the food chain,[1] cause eggshell thinning in various birds,[2] and is hypothesized to be a human carcinogen.[3] The persistence of DDT in the environment still leaves concern over the effects it and its degradation products may have today.[1,3] There are many other examples of using new technologies before uncovering adverse impacts. The sedative and morning sickness alleviator, thalidomide, was deemed safe, but after distributed use around the world was found to cause substantial birth defects.[4] The physical properties of asbestos made it a promising construction material with widespread use dating back to the ancient Greeks, but it was not until the late 1980s when the adverse impacts of the material (e.g., links to asbestosis, lung cancer, and mesothelioma) were recognized and its worldwide production declined.[5] Similarly, the unintentional presence of numerous chemicals found in personal care products (e.g., triclosan, bisphenol A, phthalates) in different environmental compartments leave scientists with rising concerns over their potential adverse impacts.[6] A need exists to understand the consequences of new technologies on the environment prior to mainstream use. We must learn from past experiences to reduce any adverse impacts, while maximizing the potential benefits of new technologies.

1.1 Engineered nanomaterials, nanotechnology, and environmental nanotechnology

Nanomaterials are defined as materials having at least one dimension less than 100 nanometers.[7] The unique size of these materials, falling between bulk materials and atomic/molecular structures, leads to interesting properties due to their high surface area to volume ratio and/or quantum effects.[8] While naturally occurring nanomaterials exist and are formed by various chemical, photochemical, thermal, mechanical, and biological processes,[9] the scope of this thesis focuses on engineered nanomaterials – nano-sized materials created and manufactured with an intended purpose. The enhanced functionalities of nanomaterials compared to their bulk materials has led to an increase in their use in various fields, including engineering, chemistry, biology, and materials science. Nanotechnology combines knowledge from all of these fields to focus on the manipulation of matter at the molecular level, on the scale of atoms or molecules.[10] Nanotechnology is being used in emerging technologies and consumers goods with applications in imaging,[11] sensing,[11] drug delivery,[12] catalysis,[13] cosmetics,[14] textiles,[15] electronics,[16] and renewable energy.[17] However, with the increase in production and use, there is also the increased risk that nanomaterials may be released into the environment, where they may interact with different organisms.[7,18] As a result, the field of environmental nanotechnology has evolved to focus on research areas at the interface of nanotechnology and the environment. These research areas include the development of novel nanomaterials with environmental benefits, the design and synthesis of "greener" and safer nanomaterials, and the assessment of any adverse ecological effects of nanomaterials.[10] Our current understanding of the impact of nanotechnology on the environment is limited and warrants investigation to avoid detrimental impacts, like in the cases discussed above. Ultimately, maximizing the benefits of engineered nanomaterials, while

minimizing any adverse impacts on the environment will result in the safe and sustainable use of nanotechnology.

1.2 Impact of environmental release of nanomaterials

Given the increase in the use, production, and disposal of engineered nanomaterials, we must consider the impact released nanomaterials may have on different biological systems. It is crucial to consider both the quantities released and the different routes of exposure of nanomaterials to organisms. Furthermore, the complexity of the environment and the biological systems needs to be considered in order to understand the impact of nanomaterials.

1.2.1 Potential routes of environmental release

Nanomaterials may reach various environmental compartments through both intentional and unintentional release. The release of nanomaterials may occur at various stages of their life cycle including, production, manufacturing, use (either direct use or use in various consumer products), and disposal (wastewater treatment, waste incineration, landfills, and recycling processes).[19] The exact quantity of nanomaterials released to the environment and in what form will ultimately determine their environmental fate and impact.[19] Determining the concentration of nanomaterials released to and present in the environment is difficult and a key challenge facing the field of environmental nanotechnology.[10] However, even without exact quantities known it is still important to consider how nanomaterials will interact with different biological systems throughout their life cycle.

1.2.2 Interactions with biological systems

Microbes, such as bacteria, algae, multicellular protozoa, and viruses, are found in all compartments within the environment (e.g., water, soil, sediment, air).[20] These microorganisms catalyze major environmental chemical reactions (including bioremediation, element cycling, and

nitrogen fixation) and contribute to overall function of various ecosystems.[21-22] The abundance, diversity, and significance of microbes in the environment necessitates understanding the potential impact of nanomaterials on these organisms in order to minimize any adverse effects.[20] Furthermore, if we can understand the fundamental interactions between nanomaterials and various organisms, we can redesign nanomaterials with reduced biological impact.

The biological impact of a nanomaterial will depend on the organisms, the physicochemical properties of the nanoparticle, and on the environmental compartment of the interaction. Nanomaterials may be designed to purposely cause adverse impacts on microbes, for example, in disinfection[22] or disease prevention applications.[23] Microbes also have the potential to physically or chemically transform nanomaterials, which may complicate our understanding of the fate and behavior of nanomaterials in the environment.[20] However, this thesis focuses around the idea that essential microbe processes may be impacted by interaction with released nanomaterials into ecosystems.

Nanomaterials may impact an organism through direct or indirect interactions. In direct interactions, a physical contact is made between the nanomaterial and the organism. One direct interaction that is common amongst different types of microbes is nanoparticle contact at the cellular membrane. After the initial contact at the cellular membrane is made, damage can arise from mechanical disruption due to the nanomaterial or through the disruption of essential membrane components.[20] Furthermore, membrane damage can result in membrane permeability and nanoparticle internalization.[20] Indirect methods of exposure may arise from the production of reactive oxygen species by nanomaterials,[24] the dissolution of toxic metals,[20,25] or the sorption of key nutrients by nanomaterials that reduce their bioavailability by the organisms.[20]

The diversity of microbes makes the generalization of modes of toxicity between nanomaterials and organisms difficult to state. One must recognize that the dimensions of microbes vary considerably, especially when comparing their length scale to that of a nanomaterial. Viruses are on the nanometer scale, bacteria are microns in length, whereas protozoa can range up to many microns.[20] As discrete particles the size range of nanomaterials is <100 nm; however, upon agglomeration in the environment their length scales may reach or exceed those of different microbes.[20] Furthermore, one must consider the chemical complexity of these organisms. The variability of biomolecules, receptors, and proteins both within and between microbes is high. While direct organismal study is crucial to fully understanding the adverse impacts that nanomaterials may pose, having means to simplify these interactions will ultimately allow us to gain molecular level insights into factors that drive the interactions between nanomaterials and organisms.

1.2.3 Environmental transformations of nanomaterials

The fate and transport of released engineered nanomaterials depends on both the chemical properties of the pristine nanomaterial prior to its release as well as different factors in the environment. Following release into the environment, a nanomaterial will exist in an unstable thermodynamic state, and as a result may undergo rapid physical and/or chemical transformations (e.g., surface transformations, sedimentation, agglomeration, dissolution).[26] These processes may occur upon release into wastewater treatment plants, natural waters, or sequentially in both, which complicates the understanding of the fate of nanomaterials in the environment. Consideration needs to be given to different environmental parameters such as, pH and ionic strength, as well as the presence of other species (e.g., surfactants, metals, natural organic matter) as all can dictate the fate of engineered nanomaterials.[26-27] The different types of interaction that a nanomaterial may

experience can be simplified to agglomeration (homo- and heteroagglomeration with naturally occurring species), surface interactions (adsorption of biomolecules, natural organic matter, ions, etc.), or transport processes (sedimentation, flow).[26] Ultimately, it is important to recognize that the pristine nanomaterial in a consumer good may be very different chemically and physically than that nanomaterial in the environment. These transformation processes can complicate the ways in which nanomaterials interact with different organisms as demonstrated in Chapter 2 of this thesis. Developing methods to be able to understand the transformations and behavior of nanomaterials in complex environments is crucial to understanding the ultimate impact of nanotechnology on the environment.

1.3 Studying interactions at the nano-bio interface

Ultimately, identifying fundamental, chemical mechanisms of interaction between nanomaterials and organisms and developing predictive guidelines to determine the biological impact of nanomaterials is crucial in order to minimize any adverse impact of nanomaterials while still exploiting their beneficial properties. In order to begin to develop this level of understanding, we need model systems that allow us to have chemical control over the systems that we study. This includes using model nanoparticle systems, where we can control the factors that are hypothesized to dictate interactions with organisms such as core composition, size, charge, and shape. It also includes using model biological systems such as supported lipid bilayers, where we can systematically control the chemical composition, charge, and packing structure of the model membrane systems. By chemically controlling both the particles we use and the biological systems we investigate, we can begin to focus on the use of *in situ* analytical techniques to study these interactions as naturally as possible in a laboratory setting.

1.3.1 Supported lipid bilayers as a model system for the cellular membrane

The diversity of microbes and environmental compartments makes it necessary to use model systems to represent the varied environments or organisms of interest. For example, *Shewanella oneidensis* is a good model bacterium to consider for interactions occurring in soils or sediments,[25] whereas the water flea, *Daphnia magna*, is a better model system for interactions occurring in freshwater environments.[28] However, even by generalizing groups of organisms together, the chemical complexity of different organisms is large, which makes studying fundamental interactions between nanomaterials and organisms difficult. One way to "simplify" the study of these interactions is to consider the first point of contact between a nanomaterial and an organism, likely the cellular membrane. Interaction with the cellular membrane has been shown as a critical process that precedes toxicity in various microorganisms,[29-30] and thus presents an important interaction to study. If we can understand interactions between nanomaterials and cellular membranes, we may be able to determine fundamental factors that drive the interactions between nanomaterials and organisms.

One common approach to studying interactions between nanoparticles and the cellular membrane is through the use of model membranes.[31] Solid-supported lipid bilayers (SLBs), or bilayers constructed on a substrate, are often used as a model system and are studied as our model membrane system in the work presented here. The benefits of using SLBs include ease of sample preparation,[32] ability to use various surface-sensitive, *in situ* characterization techniques, and the ability to incorporate various phospholipids and biomolecules, such as lipopolysaccharides[33-34] and cholesterol,[35] into the membranes to make them more representative of actual cellular membranes. In addition to natural relevance, we can control fundamental factors of the bilayers such as charge, structure, and hydrophobicity to study how these factors impact interactions with nanomaterials.

While it is still important to study interactions between nanomaterials and whole organisms, the use of SLBs provides a more controlled route to study the factors that influence these interactions using various analytical tools.

1.3.2 *in situ* analytical methods

Despite the knowledge that nanomaterials are released into the environment, their small size, low concentrations, and potential transformations limit our ability to quantify their emissions into the environment and detect and characterize them in complex environments.[10,26] A need exists to study these interactions in controlled ways while still maintaining the complexity of the environment. Current efforts in the field of environmental nanotechnology focus on improved and novel methods for detecting nanomaterials in complex environments, characterizing the physicochemical properties of nanomaterials before and after transformations, and methods to better characterize interactions between nanomaterials and biological systems.[10] Furthermore, to fully develop a mechanistic understanding of nanoparticle-microbe interactions, we need to, in real time, gain information on the dynamics of these interactions.[36]

Ultimately, the complexity of the nanomaterials, the organisms, and the interactions that occur between the two are difficult phenomena to study. It is likely that one analytical tool may provide some details into these interactions; however, it will likely not be enough to completely understand these complex interactions. A suite of *in situ* analytical approaches are necessary to uncover fundamental, molecular level factors that drive nanomaterial-organism interactions.[36-37] Through the use of model systems as well as *in situ* analytical approaches, we can start to make strides towards the safe and sustainable use of nanotechnology.

1.4 Scope of thesis

As nanotechnology continues to be implemented for various applications, the field of environmental nanotechnology will face many challenges in ensuring we minimize any adverse effects. Their release into the environment will lead to exposure to organisms. However, what that nanomaterials "looks like" to that organism, due to the potential transformations it may encounter through its life cycle, is unknown. As such, we must understand the fundamental chemical factors that drive interactions between nanomaterials and organisms, understand the ways in which nanomaterials can transform in the environment, and develop and utilize *in situ* analytical approaches to characterize nanomaterials and their interactions with various model systems. While these tasks are faced for the field as a whole, the scope of this thesis is focused particularly on the use of *in situ* analytical characterization methods to begin to understand the complex interactions between nanomaterials and cellular membranes.

Chapter two begins by examining the interaction between functionalized diamond nanoparticles and supported lipid bilayers containing lipopolysaccharides, an important biomolecule found in the outer membrane of Gram-negative bacteria. We extended these studies to include a model Gram-negative bacterium, *Shewanella oneidensis*, to validate our findings with the model membrane system. The study considers the complexity and the potential for nanomaterials to transform in the environment by characterizing these interactions in the presence and absence of natural organic matter (NOM), which is found ubiquitously in the environment. We show that NOM induces changes to the properties of nanodiamond in a concentration dependent manner, which in turn alters interactions with both model membranes and with *S. oneidensis*. These results highlight the need to consider the impact of NOM on the interactions of nanomaterials with bacterial membranes.

Chapter three uses a suite of *in situ* analytical techniques, including atomic force microscopy (AFM), quartz crystal microbalance with dissipation monitoring (QCM-D), and nanoplasmonic sensing (NPS) to characterize the interactions between positively charged quantum dots and supported lipid bilayers of various composition in real time, under environmentally relevant conditions. These complementary approaches show that the quantum dots induce structural rearrangement of the supported membranes, which could not have been explained solely by one technique alone. Emphasis is placed on how information is gained from each technique and how it comes together to present a mechanistic understanding of these interactions.

Chapter four presents considerations when correlating and corroborating the information gained from AFM measurements to other techniques. Supported lipid bilayers are used as a model system and special consideration is placed on the role that the substrate plays in these studies. Furthermore, AFM was temporally and spatially correlated with fluorescence microscopy to provide a platform for conducting both AFM and fluorescence measurements at the same time.

Chapter five utilizes a new AFM technique, PeakForce Quantitative Nanomechanical Mapping (PFQNM), to characterize the mechanical properties of a model epithelial cell, gill cells from a rainbow trout (*Oncorhynchus mykiss*). The mechanical structure of a cell is a good indicator of the overall health of a cell. As such, having an analytical method to characterize the mechanical properties of cellular membranes ultimately provides a means to probe the impact of various stressors on the mechanical properties of the cell. In this chapter, imaging was optimized and the mechanical properties (deformation, DMT modulus, adhesion, and dissipation), in addition to topography, were measured on both fixed and live cells.

Finally, chapter six considers future directions of the work presented here and the outlook on the field as a whole.

1.6 References

1. Mansouri, A.; Cregut, M.; Abbes, C.; Durand, M. J.; Landoulsi, A.; Thouand, G. The environmental issues of DDT pollution and bioremediation: A multidisciplinary review. *Appl. Biochem. Biotechnol.,* **2017,** *181,* 309-339.

2. Hellou, J.; Lebeuf, M.; Rudi, M. Review on DDT and metabolites in birds and mammals of aquatic ecosystems. *Envrion. Rev.,* **2013,** *21,* 53-69.

3. Beard, J.; Australian Rural Health Research, C. DDT and human health. *Sci. Total Environ.,* **2006,** *355,* 78-89.

4. Vargesson, N. Thalidomide embryopathy: An enigmatic challenge. *ISRN Developmental Biology,* **2013,** *2013,* 1-18.

5. Oury, T. D.; Sporn, T. A.; Roggli, V. L., *Pathology of asbestos-associated diseases*. Springer: New York, 2014.

6. Ebele, A. J.; Abou-Elwafa Abdallah, M.; Harrad, S. Pharmaceuticals and personal care products (PPCPs) in the freshwater aquatic environment. *Emerging Contaminants,* **2017,** *3,* 1-16.

7. Nel, A.; Xia, T.; Madler, L.; Li, N. Toxic potential of materials at the nanolevel. *Science,* **2006,** *311,* 622-627.

8. Farré, M.; Sanchís, J.; Barceló, D. Analysis and assessment of the occurrence, the fate and the behavior of nanomaterials in the environment. *Trends Anal. Chem.,* **2011,** *30,* 517-527.

9. Sharma, V. K.; Filip, J.; Zboril, R.; Varma, R. S. Natural inorganic nanoparticles--formation, fate, and toxicity in the environment. *Chem. Soc. Rev.,* **2015,** *44,* 8410-8423.

10. Louie, S. M.; Dale, A. L.; Casman, E. A.; Lowry, G. V., Challenges facing the environmental nanotechnology research enterprise. In *Engineered nanoparticles and the environment: Biophysicochemical processes and toxicity*, Xing, B.; Vectis, C. D.; Senesi, N., Eds. 2016; Vol. 4, pp 3-19.

11. Bogart, L. K.; Pourroy, G.; Murphy, C. J.; Puntes, V.; Pellegrino, T.; Rosenblum, D.; Peer, D.; Levy, R. Nanoparticles for imaging, sensing, and therapeutic intervention. *ACS Nano,* **2014,** *8,* 3107-3122.

12. Wilczewska, A. Z.; Niemirowicz, K.; Markiewicz, K. H.; Car, H. Nanoparticles as drug delivery systems. *Pharmacol. Rep.,* **2012,** *64,* 1020-1037.

13. Schauermann, S.; Nilius, N.; Shaikhutdinov, S.; Freund, H.-J. Nanoparticles for heterogeneous catalysis: New mechanistic insights. *Acc. Chem. Res.,* **2013,** *46,* 1673-1681.

14. DeLouise, L. A. Applications of nanotechnology in dermatology. *J. Invest. Dermatol.,* **2012,** *132,* 964-975.

15. Rivero, P. J.; Urrutia, A.; Goicoechea, J.; Arregui, F. J. Nanomaterials for functional textiles and fibers. *Nanoscale Res. Lett.,* **2015,** *10,* 501.

16. Wu, W. Inorganic nanomaterials for printed electronics: A review. *Nanoscale,* **2017,** *9,* 7342-7372.

17. Chen, X.; Li, C.; Gratzel, M.; Kostecki, R.; Mao, S. S. Nanomaterials for renewable energy production and storage. *Chem. Soc. Rev.,* **2012,** *41,* 7909-7937.

18. Maurer-Jones, M. A.; Gunsolus, I. L.; Murphy, C. J.; Haynes, C. L. Toxicity of engineered nanoparticles in the environment. *Anal. Chem.,* **2013,** *85,* 3036-3049.

19. Gottschalk, F.; Nowack, B. The release of engineered nanomaterials to the environment. *J. Environ. Monit.,* **2011,** *13,* 1145-1155.

20. Ge, Y.; Horst, A. M.; Kim, J.; Priester, J. H.; Welch, Z. S.; Holden, P. A., Toxicity of manufactured nanomaterials to microorganisms. In *Engineered nanoparticles and the environment: Biophysicochemical processes and toxicity*, Xing, B.; Vectis, C. D.; Senesi, N., Eds. 2016; pp 320-346.

21. Falkowski, P. G.; Fenchel, T.; Delong, E. F. The microbial engines that drive earth's biogeochemical cycles. *Science,* **2008,** *320,* 1034-1039.

22. Hajipour, M. J.; Fromm, K. M.; Ashkarran, A. A.; Jimenez de Aberasturi, D.; de Larramendi, I. R.; Rojo, T.; Serpooshan, V.; Parak, W. J.; Mahmoudi, M. Antibacterial properties of nanoparticles. *Trends Biotechnol.,* **2012,** *30,* 499-511.

23. Taki, A.; Smooker, P. Small wonders-the use of nanoparticles for delivering antigen. *Vaccines,* **2015,** *3,* 638-661.

24. Nel, A. E.; Madler, L.; Velegol, D.; Xia, T.; Hoek, E. M.; Somasundaran, P.; Klaessig, F.; Castranova, V.; Thompson, M. Understanding biophysicochemical interactions at the nano-bio interface. *Nat. Mater.,* **2009,** *8,* 543-557.

25. Hang, M. N.; Gunsolus, I. L.; Wayland, H.; Melby, E. S.; Mensch, A. C.; Hurley, K. R.; Pedersen, J. A.; Haynes, C. L.; Hamers, R. J. Impact of nanoscale lithium nickel manganese cobalt oxide (NMC) on the bacteriumshewanella oneidensismr-1. *Chem. Mater.,* **2016,** *28,* 1092-1100.

26. Praetorius, A.; Arvidsson, R.; Molander, S.; Scheringer, M. Facing complexity through informed simplifications: A research agenda for aquatic exposure assessment of nanoparticles. *Environ. Sci.: Processes Impacts,* **2013,** *15,* 161-168.

27. Wagner, S.; Gondikas, A.; Neubauer, E.; Hofmann, T.; von der Kammer, F. Spot the difference: Engineered and natural nanoparticles in the environment--release, behavior, and fate. *Angew. Chem. Int. Ed. Engl.,* **2014,** *53,* 12398-12419.

28. Stollewerk, A. The water flea *Daphnia* - a 'new' model system for ecology and evolution? *J. Biol.,* **2010,** *9,* 1-4.

29. Lesniak, A.; Salvati, A.; Santos-Martinez, M. J.; Radomski, M. W.; Dawson, K. A.; Aberg, C. Nanoparticle adhesion to the cell membrane and its effect on nanoparticle uptake efficiency. *J. Am. Chem. Soc.,* **2013,** *135,* 1438-1444.

30. Chen, K. L.; Bothun, G. D. Nanoparticles meet cell membranes: Probing nonspecific interactions using model membranes. *Environ. Sci. Technol.,* **2014,** *48,* 873-880.

31. Rascol, E.; Devoisselle, J. M.; Chopineau, J. The relevance of membrane models to understand nanoparticles-cell membrane interactions. *Nanoscale,* **2016,** *8,* 4780-4798.

32. Richter, R.; Mukhopadhyay, A.; Brisson, A. Pathways of lipid vesicle deposition on solid surfaces: A combined QCM-D and AFM study. *Biophys. J.,* **2003,** *85,* 3035-3047.

33. Kaufmann, S.; Ilg, K.; Mashaghi, A.; Textor, M.; Priem, B.; Aebi, M.; Reimhult, E. Supported lipopolysaccharide bilayers. *Langmuir,* **2012,** *28,* 12199-12208.

34. Jacobson, K. H.; Gunsolus, I. L.; Kuech, T. R.; Troiano, J. M.; Melby, E. S.; Lohse, S. E.; Hu, D.; Chrisler, W. B.; Murphy, C. J.; Orr, G.; Geiger, F. M.; Haynes, C. L.; Pedersen, J. A. Lipopolysaccharide density and structure govern the extent and distance of nanoparticle interaction with actual and model bacterial outer membranes. *Environ. Sci. Technol.,* **2015,** *49,* 10642-10650.

35. Melby, E. S.; Mensch, A. C.; Lohse, S. E.; Hu, D.; Orr, G.; Murphy, C. J.; Hamers, R. J.; Pedersen, J. A. Formation of supported lipid bilayers containing phase-segregated domains and their interaction with gold nanoparticles. *Environ. Sci.: Nano,* **2016,** *3,* 45-55.

36. Murphy, C. J.; Vartanian, A. M.; Geiger, F. M.; Hamers, R. J.; Pedersen, J.; Cui, Q.; Haynes, C. L.; Carlson, E. E.; Hernandez, R.; Klaper, R. D.; Orr, G.; Rosenzweig, Z. Biological responses to engineered nanomaterials: Needs for the next decade. *ACS Cent. Sci.,* **2015,** *1,* 117-123.

37. Troiano, J. M.; Olenick, L. L.; Kuech, T. R.; Melby, E. S.; Hu, D.; Lohse, S. E.; Mensch, A. C.; Dogangun, M.; Vartanian, A. M.; Torelli, M. D.; Ehimiaghe, E.; Walter, S. R.; Fu, L.; Anderton, C. R.; Zhu, Z.; Wang, H.; Orr, G.; Murphy, C. J.; Hamers, R. J.; Pedersen, J. A.; Geiger, F. M. Direct probes of 4 nm diameter gold nanoparticles interacting with supported lipid bilayers. *J. Phys. Chem. C,* **2015,** *119,* 534-546.

Chapter 2: Natural Organic Matter Concentration Impacts the Interaction of Functionalized Diamond Nanoparticles with Model and Actual Bacterial Membranes

The following chapter is adapted from the article published in *Environmental Science & Technology*, **2017**, *51*, 11075-11084 (DOI: 10.1021/acs.est.7b02823), with the following co-authors Rodrigo Tapia Hernandez, Joshua E. Kuether, Marco D. Torelli, Z. Vivian Feng, Robert J. Hamers, and Joel A. Pedersen

2.1 Introduction

Rapid growth in the production and use of engineered nanomaterials has been accompanied by an increase in the potential for these materials to be released into the environment and for organisms to be exposed to them.[1-2] The large surface-to-volume ratio of nanomaterials as well as their high surface energy promotes the acquisition of a coating or "corona" of natural organic matter (NOM)[3-5] upon entry into wastewater treatment plants, natural waters, aquatic sediments, and soils. Natural organic matter is comprised of a complex mixture of relatively low molecular mass organic compounds resulting primarily from microbial degradation of vegetation, algae, and bacterial biomass.[6] Natural organic matter is found in natural waters at organic carbon (oc) concentrations ranging from ~0.5 $mg_{oc} \cdot L^{-1}$ in seawater and groundwater to over 30 $mg_{oc} \cdot L^{-1}$ in wetlands.[7] Over the pH range typical for environmental systems (4 to 9), NOM bears a net negative charge due to the deprotonation of carboxyl and phenolic groups.[8-9] Acquisition of a NOM "corona" alters the physical and chemical properties of nanomaterials and impacts their transport and fate in the environment.[10-13] Interaction with NOM can stabilize nanoparticle suspensions electrostatically or through a combination of electrostatic and steric interactions.[13] Natural organic matter can induce aggregation of nanoparticles in the presence of elevated concentrations of

divalent metal cations and when neutralizing nanoparticle charge.[14-16] Such nanoparticle aggregation in the presence of NOM depends on the nanoparticle coating,[14,17] NOM properties (e.g., polarity fraction,[18-21] molecular mass[22-25]), and NOM concentration.[16,26-27] Natural organic matter-induced changes to nanoparticle surface charge, colloidal stability, and hydrodynamic properties warrant consideration in assessing the potential for these materials to adversely impact organisms in the environment.

The initial point of contact between nanoparticles and cells is often a lipid membrane, yet the impact of NOM on nanoparticle interactions with cell membranes has received little study. One previous study showed that humic acid decreased fullerene accumulation in zwitterionic and negatively charged solid-supported lipid membranes and reduced uptake by Caco-2 cells.[28] The reduction in cellular uptake was attributed to electrostatic repulsion between the negatively charged humic acid-coated fullerene surface and the negatively charged Caco-2 cytoplasmic membrane.[28] Similarly, NOM prevented adhesion of nanoscale zero-valent iron to the outer membrane of *Escherichia coli* through electrostatic and steric repulsion, decreasing toxicity.[29] These studies demonstrate that NOM coatings can modulate the interaction of nanoparticles with cellular membranes.

Solid-supported lipid bilayers are often used as model systems to understand the complex interactions that occur between nanomaterials and cellular membranes.[30-36] The majority of these studies have employed bilayers composed of a single phospholipid or binary mixtures of phospholipids. Such bilayers do not include cell surface components expected to be important for the interaction of nanoparticles with bacteria. For example, the outer membrane of Gram-negative bacteria is complex and its outer leaflet contains up to 75% lipopolysaccharides (LPS), a class of glycolipids.[37] The construction of model membranes incorporating LPS has been recently

reported.[33,38] Nanoparticle interactions with model membranes incorporating LPS are expected to correspond more closely to results obtained using bacteria than are those with bilayers lacking these important cell-surface molecules.[33] Identification of the impacts of NOM on nanoparticle hydrodynamic and electrokinetic properties as well as on their interactions with model and actual bacterial membranes is needed to better elucidate the role NOM plays in interactions between nanomaterials and bacteria.

The objectives of this study were to investigate the impact of NOM-to-nanoparticle concentration ratio on the interaction of cationic nanoparticles with model cell membranes, including those incorporating LPS, and with the Gram-negative bacterium *Shewanella oneidensis* MR-1. To achieve these objectives, we used diamond nanoparticles (DNPs) functionalized with the polycation poly(allylamine HCl) (PAH) and Suwannee River NOM as model systems. Nanodiamond is used as a polishing material,[39] an additive in rubbers[40] and lubricants,[39] and in drug delivery and bioimaging.[41] Use of DNPs in the present study was motivated by their chemical stability and the ease with which they can be functionalized, allowing us to probe interactions with NOM and model and actual bacterial surfaces without complications arising from dissolution of the nanoparticle core material.[42] We chose the PAH polymer to functionalize the DNPs to investigate the impact of NOM on a capping agent previously shown to be toxic to bacteria and the microcrustacean *Daphnia magna* when mounted on nanogold.[43-44] We used quartz crystal microbalance with dissipation monitoring (QCM-D) to investigate nanoparticle interaction with model membranes lacking or incorporating LPS. We further examined the impact of NOM on membrane damage and toxicity to *S. oneidensis* induced by PAH-DNP. The results presented here provide new insights into how NOM affects the interaction of nanomaterials with bacterial membranes.

2.2 Materials and Methods

2.2.1 Functionalization of diamond nanoparticles.

Diamond nanoparticles (Monocrystalline Synthetic Diamond, MSY 0-0.03 μm) were obtained from Microdiamant (Legwil, Switzerland). As-received DNPs were oxidized by reflux in a 3:1 (v/v) mixture of concentrated H_2SO_4 and HNO_3 for 3 d (Caution: extremely caustic). After oxidation the nanodiamond was diluted (10×) in ultrapure water (18.2 MΩ·cm resistivity, MilliQ-Advantage A10, Millipore) and centrifuged (5 min, 4696*g*) to sediment the particles. After an additional wash (centrifugation and resuspension in ultrapure water), the pellet was resuspended in 3:1 (v/v) H_2SO_4:HNO_3 and refluxed for another 3 d. The resulting nanoparticle suspension was diluted, centrifuged (5 min, 4696*g*), and resuspended repeatedly until the pH was neutral and the particles did not sediment. The dispersed particles were electrostatically wrapped with PAH polymer (15 kDa, Sigma Aldrich) by mixing particles (1 $mg \cdot mL^{-1}$ as determined by gravimetric analysis) with polymer solution (1 $mg \cdot mL^{-1}$ in 0.001 M NaCl) at a 1:1 ratio overnight. Particles were dialyzed (Spectrum Labs, nominal molecular weight cut-off 50 kDa) against 4 L of ultrapure water three times (4 h the first time and 24 hr each for the two subsequent times) to remove excess polymer.

2.2.2 Natural organic matter.

Suwannee River NOM was obtained from the International Humic Substances Society (1R101N, St. Paul, MN). Stock solutions of NOM (200 $mg_{oc} \cdot L^{-1}$) were prepared in ultrapure water (18.2 MΩ·cm resistivity, Barnstead GenPure Pro) adjusted to pH 10 with 6 M NaOH. The solution was allowed to stir overnight in the dark, filtered through a 0.22 μm Teflon® filter, and stored at 4 °C. The total organic content in the stock solution was determined after filtration using the UV/persulfate oxidation method with membrane conductometric detection of CO_2 (GE

Instruments/Sievers Model 900 TOC analyzer, 186 ± 13 $mg_{oc} \cdot L^{-1}$). Prior to use in experiments, NOM solutions were buffered to pH 7.4 with 0.002 M 4-(2-hydroxyethyl)-1-piperazineethanesulfonic acid (HEPES, Fisher Scientific) and the ionic strength was adjusted to 0.025 M with NaCl.

2.2.3 Hydrodynamic and electrokinetic characterization.

We determined diffusivities and electrophoretic mobilities of PAH-DNPs over a range of NOM-to-DNP concentration ratios, by dynamic light scattering and laser Doppler microelectrophoresis (75 V; Malvern ZetaSizer Nano ZS, Worcestershire, UK). Unless otherwise noted, experiments were conducted at a 1 nM number concentration of PAH-DNP in 0.025 M NaCl buffered to pH 7.4 with 0.002 M HEPES (ionic strength and pH values within the ranges encountered in natural freshwater systems).[45] After addition of PAH-DNP to a buffered NOM solution, the mixture was vortexed and analyzed immediately. (Experiments were conducted to evaluate the effect of contact time on DLS and ζ potential measurements, and we saw no significant differences between immediate analysis and analysis after 1 h of contact time, here we report findings for the case where the particles were mixed and immediately analyzed). Diffusivity and electrophoretic mobility measurements represent averages of five measurements. We calculated intensity-averaged hydrodynamic diameters from the particle diffusivities using the Stokes−Einstein equation. Hydrodynamic diameter (d_h) number distributions were estimated from the intensity measurements using Mie theory.[46] We estimated DNP ζ-potentials from the electrophoretic mobility using the Smoluchowski approximation.[47-48] The Smoluchowski approximation assumes the particle is a hard sphere; however, the polyelectrolyte coatings on the nanodiamond used here renders a relatively soft, ion-penetrable shell on a hard particle core, making the ζ-potential derived from the Smoluchowski approximation an apparent value.[48]

2.2.4 Quantification of free NOM in solution.

Ultraviolet-visible (UV-Vis) absorption spectroscopy was used to determine the amount of chromophoric NOM bound to the surface of the PAH-DNPs (Shimadzu UV-2401PC). Samples varying in NOM-to-DNP ratio were prepared as described for DLS measurements and then centrifuged (90 min, 25,000*g*, 25 °C) to produce a pellet of either PAH-DNP or NOM/PAH-DNP. Supernatant was removed, and the chromophoric NOM remaining in the supernatant was quantified by comparing the absorbance at 320 nm to a calibration curve made from a stock NOM solution (Figure A2.1).

2.2.5 Preparation and characterization of phospholipid vesicles.

We prepared small unilamellar vesicles (SUVs) composed of solely 1-palmitoyl-2-oleoyl-*sn*-glycero-3-phosphocholine (POPC, 16:0-18:1 PC; Avanti Polar Lipids) or with 0.46 mol% rough LPS (rLPS) or smooth LPS (sLPS) or 6.4 mol% rLPS as recently described.[33] Rough and smooth LPS were from *Salmonella enterica* serotype minnesota Re 595 (the so-called deep rough mutant) and serotype minnesota, respectively (Sigma Aldrich). Further details on preparation and characterization of these vesicles, as well as the generic structure of LPS are presented in the Appendix (Figures A2.2 and A2.3).

2.2.6 Interaction of diamond nanoparticles with supported lipid bilayers.

We used QCM-D to monitor the formation of supported lipid bilayers and their interactions with nanoparticles in real time and without the use of labels. The QCM-D technique measures the changes in resonance frequency (Δf) and energy dissipation (ΔD) for an AT-cut quartz crystal as an analyte interacts with the sensor surface. Changes in frequency are related to changes in the mass coupled to the sensor surface, which includes the mass of both the analyte and of any dynamically coupled solvent. The dissipation factor, *D*, represents the fractional energy loss per

radian at the oscillation frequency and provides information on the viscoelastic properties of laterally homogeneous adlayers or the stiffness of particle–surface contacts for films of discrete nanosized objects.[49] Rigidly adsorbed films have a fractional energy loss per radian of oscillation that is small relative to the change in frequency of a given harmonic (n), defined $-\Delta D_n/(\Delta f_n/n) << 2/(f_n)$ (equal to 4×10^{-7} Hz^{-1} for the 4.96 MHz crystals used here),[49] where n is the harmonic number. For such films, the adsorbed surface mass density ($\Delta\Gamma_{QCM\text{-}D}$) is linearly related to the change in frequency, as described by the Sauerbrey equation:[50]

$$\Delta\Gamma_{QCM\text{-}D} = -\frac{C}{n}\Delta f_n \tag{1}$$

where C is the mass sensitivity constant (equal to 18.0 $ng \cdot Hz^{-1} \cdot cm^{-2}$ for a 4.96 MHz crystal). In the PAH-DNP experiments presented, $-\Delta D_n/(\Delta f_n/n) < 4 \times 10^{-7}$ Hz^{-1} (Table A2.7), and the Sauerbrey equation was used to estimate acoustic surface mass density. The fundamental and odd harmonics (n = 3-11) were measured simultaneously. Data from odd harmonics 3 through 11 were equivalent;[51] we present data from the 5th harmonic (~25 MHz) for all studies. Initial rates of PAH-DNP deposition (r_d) were calculated as the first derivative of the change in acoustic surface mass density with respect to time over the first 30 seconds of attachment:[52-54]

$$r_d = \frac{d\Gamma_{QCM\text{-}D}}{dt} \tag{2}$$

Prior to QCM-D experiments, SiO_2-coated sensor crystals (QSX303, Biolin Scientific, Stockholm, Sweden) were cleaned by sonicating in a 2% sodium dodecyl sulfate solution (10 min), rinsing alternatively with ultrapure water and ethanol three times, drying with N_2 gas, and exposed to ultraviolet light (185 nm and 254 nm) from a low-pressure mercury lamp (20 min) to remove any trace organic compounds (Bioforce Nanosciences UV/Ozone Procleaner).

We formed supported lipid bilayers on SiO_2-coated quartz crystal microbalance sensors from SUVs composed of POPC with or without LPS via the vesicle fusion method[33,38,55] using a Q-Sense E4 instrument (Biolin Scientific). The sensors were first equilibrated in 0.150 M NaCl buffered to pH 7.4 with 0.002 M HEPES (pH and buffer concentration used throughout unless otherwise noted). Vesicles (0.125 $mg \cdot mL^{-1}$) in a solution of the same composition were flowed (0.100 $mL \cdot min^{-1}$) over the surface until the critical surface vesicle concentration (evidenced as the time at which the maximum frequency change is observed)[56] was attained and the vesicles ruptured and fused to form a bilayer. After frequency and dissipation values stabilized, vesicle-free solution was flowed over the sensor to remove any loosely adsorbed vesicles. The ionic strength was lowered by exchanging the 0.150 M NaCl solution with 0.025 M NaCl solution until a stable baseline was reached. Figure A2.4 shows a representative frequency trace.

Suspensions of PAH-DNP with or without NOM (5 or 30 $mg_{oc} \cdot L^{-1}$) or NOM alone (5 or 30 $mg_{oc} \cdot L^{-1}$) in 0.025 M NaCl were flowed over the supported lipid bilayers, and attachment was monitored for 20 min. (For samples including NOM and PAH-DNPs, PAH-DNPs were exposed to NOM for up to 20 min before introduction to the QCM-D as no further aggregation of the particles was observed by DLS in this time frame.) After 20 min, bilayers were rinsed with nanoparticle-free solution to examine the reversibility of attachment. In a subset of experiments, the bilayer was equilibrated with 4.7 $mg \cdot L^{-1}$ PAH polymer prior to the introduction of PAH-DNP (with or without NOM) to examine the influence of adsorbed polymer on nanoparticle attachment to the bilayers (Table A2.9). Attachment experiments were conducted in at least triplicate at 25.0 ± 0.5 °C.

2.2.7 *Shewanella oneidensis* viability and membrane damage.

Shewanella oneidensis was grown from colonies on an agar plate in *Difco*™ Luria-Bertani (LB) Broth overnight in a shaker incubator (30 °C, 275 rpm). Cells were sedimented (2000*g*, 10 min) and resuspended in Dulbecco's phosphate-buffered saline (D-PBS), and sedimented and resuspended again in fresh 0.025 M NaCl buffered to pH 7.4 with 0.002 M HEPES before exposure to nanoparticles.

We evaluated the toxicity of PAH-DNP to *S. oneidensis* using a growth-based viability assay to quantify actively metabolizing cells.[57] The time for a cell culture to reach log phase depends on initial cell density: the longer the delay (lag phase), the lower the initial viable cell density (measured in colony forming units, CFU). A calibration curve of *S. oneidensis* was constructed using serially diluted cell culture where 10^7 CFU·mL^{-1} was defined as 100% viable. A *S. oneidensis* culture at 10^7 CFU·mL^{-1} was incubated (10 min) with NOM alone or with NOM+DNP at ratios ranging from 0 to 6.67 $mg_{oc} \cdot mg_{PAH\text{-}DNP}^{-1}$, then diluted in fresh LB medium in a 96-well plate. Optical density at 600 nm was monitored at 20-min intervals for 20 h (SpectraMax Plate Reader) at 30 °C with agitation between readings to track cell growth. The time to reach log phase for each exposure condition was compared to the calibration curve to determine any change in viability.

The LIVE/DEAD BacLight™ kit (ThermoFisher Scientific) was used to assess bacterial membrane damage by PAH-DNP in the presence and absence of NOM. We exposed *S. oneidensis* to 1 nM PAH-DNP at NOM-to-DNP ratios ranging from 0 to 6.67 $mg_{oc} \cdot mg_{PAH\text{-}DNP}^{-1}$ for 10 min, and the cells were distributed in a 96-well plate in triplicate. The LIVE/DEAD stain mixture was used according to manufacturer recommendations. Analyses were conducted using a fluorescence plate reader using an excitation wavelength of 485 nm. Fluorescence intensity was

measured at 528 nm and 635 nm for SYTO9 and propidium iodide (PI), respectively. SYTO9-to-PI fluorescence intensity ratios were determined for each exposure and normalized to that of a control bacterial sample not exposed to either PAH-DNP or NOM.

2.2.8 Statistical analyses.

Comparisons across bilayer types and particle conditions were made using a two-way ANOVA with a Tukey correction for multiple comparisons at the $\alpha = 0.05$ level of significance (Prism 6.0).

2.3 Results and Discussion

2.3.1 NOM alters nanoparticle hydrodynamic and electrokinetic properties.

We determined the hydrodynamic diameter (d_h) and ζ-potential of the PAH-DNPs over a range of NOM concentrations (0 to 30 $mg_{oc} \cdot L^{-1}$) representing NOM-to-PAH-DNP ratios of 0 to 8 $mg_{oc} \cdot mg_{PAH\text{-}DNP}^{-1}$. Interaction with NOM induced changes to PAH-DNP d_h (Figure 2.1a) and ζ-potential (Figure 2.1b). In the absence of NOM at an ionic strength of 0.025 M and a pH of 7.4 (0.002 M HEPES), PAH-DNPs were present in suspension primarily as single positively charged nanoparticles ($d_h = 17 \pm 6$ nm, equivalent to the nominal core size of the nanoparticles, ~15 nm; ζ-potential = +21 ± 3 mV). At a NOM-to-DNP ratio of 1.33 $mg_{oc} \cdot mg_{PAH\text{-}DNP}^{-1}$, the d_h of PAH-DNP increased to 42 ± 9 nm, indicating a modest degree of aggregation, but the ζ-potential remained unchanged (+22.3 ± 0.6 mV). Measurement of the NOM in solution that was not bound to PAH-DNPs at this NOM-to-DNP ratio was thwarted by the inability to sediment these particles from suspension even at centrifugal forces up to 649,555*g* for 120 min. The PAH-DNPs were more stable with respect to sedimentation at 1.33 $mg_{oc} \cdot mg_{PAH\text{-}DNP}^{-1}$ than when no NOM was present. Increasing the NOM-to-DNP ratio to 2.67 $mg_{oc} \cdot mg_{PAH\text{-}DNP}^{-1}$ resulted in further particle aggregation and a reversal of ζ-potential to –13.0 ± 0.4 mV. At NOM-to-DNP ratios of 4 $mg_{oc} \cdot mg_{PAH\text{-}DNP}^{-1}$ and

higher, the d_h and ζ-potentials of the PAH-DNP remained relatively constant, near 40 nm and –30 mV, respectively. Sedimentation of aggregates formed at NOM-to-DNP ratios of 2.67 and 8 $mg_{oc} \cdot mg_{PAH\text{-}DNP}^{-1}$ from suspension by centrifugation (90 min, 25,000*g*) and determination of the amount of NOM remaining in the supernatant (Figure A2.1), suggested that 2.1 $mg_{oc} \cdot mg_{PAH\text{-}DNP}^{-1}$ bound to the surface of the DNP (0.011 $mg_{oc} \cdot nm^{-2}$).

We attribute the decrease in PAH-DNP ζ-potential with increasing NOM-to-DNP concentration ratio primarily to electrostatic interaction of deprotonated carboxyl groups of NOM with the positively charged pendant primary amines on the PAH polymers. At low NOM-to-DNP ratios ($\leq$ 1.33 $mg_{oc} \cdot mg_{PAH\text{-}DNP}^{-1}$), interaction with NOM molecules induces a small degree of aggregation, but the NOM molecules are not present at high enough concentration to neutralize the overall charge of the PAH-DNPs or displace the PAH polymer wrapping. At this low NOM-to-DNP ratio, aggregation may be due to NOM adsorption leading to uneven charge distribution and a concomitant attractive contribution to the interaction energy.[58-59] Aggregation induced by oppositely charged patches on nanoparticle surfaces is not satisfactorily represented by classical Derjaguin–Landau–Verwey–Overbeek (DLVO) theory.[60] As the NOM-to-DNP ratio increased, electrostatic interaction with NOM molecules neutralized and then reversed the positive charge on the DNPs; when the magnitude of the ζ-potential was small, attractive van der Waals forces overcame electrostatic repulsion between particles and destabilized the particle suspensions. Alternatively, aggregation rates may have risen as the probability of favorable interactions increased between oppositely charged regions on the DNP surfaces (a function of surface coverage and charge density of both the PAH and the adsorbing NOM molecules) leading to maximum aggregation rates at non-zero net surface charge.[58-59] At yet higher NOM-to-DNP ratios ($\geq$4 $mg_{oc} \cdot mg_{PAH\text{-}DNP}^{-1}$), the NOM-coated particles possessed strongly negative ζ-potentials (–30 mV) and

yielded stable suspensions of DNP aggregates with comparable d_h (one-way ANOVA, $p = 0.2334$). The observed charge reversal indicated that NOM molecules either overcoat the positively charged polymer on the nanodiamond surface, forming a "NOM corona" around the particles, or displaced the electrostatically wrapped PAH polymer. Charge reversal of positively charged bare zinc oxide,[61-62] hematite,[15] and titanium dioxide[16] due to interaction with NOM has been reported previously. Furthermore, increasing the concentration ratio of NOM to gold nanoparticles functionalized with positively charged branched polyethylenimine or aminated polyethylene glycol led to charge neutralization and ultimately charge reversal much like we observed with PAH-DNPs.[17] Our findings are consistent with these results and demonstrate the same phenomenon for particles differing in core material and initial organic coating.

2.3.2 Nanodiamond attachment to zwitterionic phospholipid bilayers.

We next investigated the impact of the NOM-induced changes to PAH-DNP properties on their interaction with model membranes composed of the zwitterionic phospholipid POPC. We examined the influence of NOM on initial attachment rates to and acoustic surface mass densities attained on POPC bilayers of PAH-DNPs at NOM-to-DNP ratios of 0, 1.33, and 8 $mg_{oc} \cdot mg_{PAH\text{-}DNP}^{-1}$ by QCM-D (Figure 2.2). Consistent with expectations, electrostatic attraction between the positively charged PAH-DNP and the negative potential of the supported zwitterionic POPC bilayer[34,63] led to attachment in the absence of NOM (Figure 2.2). We calculated the efficiency of PAH-DNP attachment to lipid bilayers to quantify the kinetics of initial attachment:[64]

$$a_D = \frac{\left(d\Gamma_{QCM\text{-}D}/dt\right)_{\text{lipid bilayer}}}{\left(d\Gamma_{QCM\text{-}D}/dt\right)_{fav}} \quad (3)$$

where $d\Gamma_{QCM\text{-}D}/dt$ is the change in adsorbed surface mass density per unit time and the subscript fav on the term in the denominator refers to the change in adsorbed surface mass density under

favorable deposition conditions (absence of an energy barrier to deposition). In the present study, we approximated favorable deposition conditions for the positively charged PAH-DNPs using the strongly negatively charged SiO_2 surface.[63] To do this, we empirically determined initial rates of attachment to SiO_2 under the same conditions used for the bilayers. We found all attachment efficiencies for PAH-DNPs to be near unity (Table A2.2), consistent with previous findings of favorable interaction between cationic nanoparticles and zwitterionic lipid bilayers.[33,65-66] We hypothesize that the amine groups on the PAH polymer on the nanodiamond interacted with the phosphate group in the phosphatidylcholine headgroup of the POPC lipids.[67-68] The surface mass density of PAH-DNPs attained after 20 min was higher on the POPC bilayer than on SiO_2 by a factor of ~3.6 (Figure 2.2b, Table A2.8). Lateral repulsion between positively charged PAH-DNP appears to limit the extent of attachment on the SiO_2 surface. Lateral repulsion seems to be diminished on the POPC bilayer, likely due to phospholipid extraction,[35,67] allowing higher surface densities to be reached. Rinsing with nanoparticle-free solution produced small (9 ± 2 ng·cm^{-2}) decreases in acoustic mass consistent with removal of a small population of loosely adhered PAH-DNPs. The attachment of the remaining PAH-DNPs was irreversible on the timescale of our experiments.

At the low NOM-to-DNP ratio of 1.33 $mg_{oc} \cdot mg_{PAH\text{-}DNP}^{-1}$, the PAH-DNP aggregated to a moderate extent ($d_h = 42 \pm 9$ nm) and retained a positive ζ-potential ($+22.3 \pm 0.6$ mV). The initial rate of PAH-DNP attachment to POPC bilayers at this low NOM-to-DNP ratio did not differ significantly from that for PAH-DNP in the absence of NOM ($p > 0.05$; Figure 2.2a and Table A2.1), and attachment efficiencies were close to unity (Table A2.2). This result is not attributable to the deposition of NOM itself to the bilayer. Control experiments showed the initial rate of NOM attachment to POPC to be nearly zero at a concentration of 5 $mg_{oc} \cdot L^{-1}$ (the total NOM concentration

in the 1.33 $mg_{oc}\cdot mg_{PAH\text{-}DNP}^{-1}$ NOM-to-DNP suspensions; Table A2.1). Furthermore, exposure of POPC bilayers to 5 $mg_{oc}\cdot L^{-1}$ NOM prior to introduction of PAH-DNP did not alter the initial attachment rate (-1.8 ± 0.2 $ng\cdot cm^{-2}\cdot s^{-1}$; $p > 0.05$). We expect transport of the aggregates formed in the presence of 5 $mg_{oc}\cdot L^{-1}$ NOM to the model membrane surface to be slower than that of the individual PAH-DNPs. Using a Lévêque solution for convective-diffusive transport modified to account for the curvilinear flow in the QCM-D flow chamber,[69] we estimate that in the presence of 5 mg_{oc}/L NOM the spatially averaged mass-transport limited attachment rate constant is smaller by a factor of 0.56 ± 0.15 relative to the case without NOM (for details of this analysis see the Supporting Information). The equivalence of the initial attachment rates in the absence and presence of 5 mg_{oc}/L NOM implies that that on average the effective mass of the aggregates (mass of PAH-DNPs, NOM and internal water) attaching to the model membrane during the initial attachment period is larger by a factor of approximately two that of the individual PAH-DNPs.

The acoustic surface mass density ($\Gamma_{QCM\text{-}D}$) of PAH-DNP on POPC bilayers after 20 min exposure under flowing conditions was substantially larger at a NOM-to-DNP ratio of 1.33 $mg_{oc}\cdot mg_{PAH\text{-}DNP}^{-1}$ than in the absence of NOM ($p < 0.0001$; Figure 2.2b, Table A2.8) and was accompanied by larger energy dissipation than in the absence of NOM (Table A2.6) and more pronounced dispersion in $\Delta f_n/n$ indicating that the NOM/PAH-DNP aggregates were less rigidly coupled to the oscillating sensor than in the absence of NOM. Rinsing with PAH-DNP- and NOM-free solution resulted in no net change in acoustic mass indicating that NOM/PAH-DNP attachment to POPC bilayers was irreversible over experimental time scales. The much larger $\Gamma_{QCM\text{-}D}$ was not attributable to adsorption of NOM alone; exposure of POPC bilayers to 5 $mg_{oc}\cdot L^{-1}$ NOM in the absence of PAH-DNP resulted in $\Gamma_{QCM\text{-}D}$ values far too small (Table A2.8) to account for the large difference observed in PAH-DNP attachment in the presence and absence of this

concentration of NOM. Furthermore, $\Gamma_{QCM\text{-}D}$ for attachment to POPC bilayers was statistically indistinguishable whether or not the bilayers had been first exposed to 5 $mg_{oc}\cdot L^{-1}$ NOM for 20 min prior to interaction with PAH-DNP. We therefore attributed the higher $\Gamma_{QCM\text{-}D}$ at the 1.33 $mg_{oc}\cdot mg_{PAH\text{-}DNP}^{-1}$ NOM-to-DNP ratio relative to that in the absence of NOM to NOM-induced changes to PAH-DNP properties. As noted above, adsorption of NOM molecules may lead to electrostatic attraction between oppositely charged regions on adjacent DNPs and thereby a moderate degree of aggregation at NOM concentrations insufficient to induce rapid aggregation while the ζ-potential remains positive. The effective mass of these aggregates (mass of PAH-DNPs, NOM and internal water) is higher than that of single PAH-DNPs. We therefore attributed the higher $\Gamma_{QCM\text{-}D}$ at a NOM-to-DNP ratio of 1.33 $mg_{oc}\cdot mg_{PAH\text{-}DNP}^{-1}$ to the larger effective mass of the aggregated particles delivered to the sensor surface.

At a NOM-to-DNP ratio of 8 $mg_{oc}\cdot mg_{PAH\text{-}DNP}^{-1}$, NOM molecules induced a modest degree of aggregation (d_h = 34 ± 13 nm) and coated the PAH-DNPs to the extent that the surface charge was reversed and the ζ-potential was strongly negative (–33 ± 1 mV). At this NOM-to-DNP ratio, the initial rate of PAH-DNP deposition was more than an order of magnitude lower than in the absence of NOM ($p < 0.0001$; Figure 2.2a, Table A2.1) and $\Gamma_{QCM\text{-}D}$ values at 20 min were much smaller than in the absence of NOM (Figure 2.2b, Table A2.8). The NOM concentration remaining in PAH-DNP suspensions at the NOM-to-DNP ratio used here was ~22 $mg_{oc}\cdot L^{-1}$. We examined the initial rate of deposition of 30 $mg_{oc}\cdot L^{-1}$ NOM (the total NOM concentration in the 8 $mg_{oc}\cdot mg_{PAH\text{-}DNP}^{-1}$ NOM-to-DNP suspensions) and the adsorbed surface mass density at 20 min and found the NOM deposition rate and $\Gamma_{QCM\text{-}D}$ to be comparable to those measured for the 8 $mg_{oc}\cdot mg_{PAH\text{-}DNP}^{-1}$ NOM-DNP ratio (Figure 2.2b, Table A2.1). We therefore attribute the small frequency shifts observed in the NOM-DNP attachment experiments at the high NOM-to-DNP

ratio to NOM molecules adsorbing to the bilayer. These results are consistent with following interpretation: NOM molecules overcoated the PAH-DNP or displaced the electrostatically wrapped PAH polymer on the DNP surface to the extent that the ζ-potential of the aggregates became strongly negative resulting in a significant electrostatic energy barrier to attachment to the negatively charged supported model membranes to which NOM had adsorbed.[65,70]

2.3.3 Nanodiamond interaction with phospholipid bilayers containing lipopolysaccharides.

Full-length, or smooth, LPS is composed of three parts: Lipid A, a core oligosaccharide, and an *O*-polysaccharide (Figure A2.2).[71-73] The presence or absence of an *O*-polysaccharide determines whether a LPS molecule is respectively smooth or rough.[71] Rough LPS (expressed by some bacteria) is a truncated form of LPS, which contains Lipid A and at least part of the core oligosaccharide, but lacks the outer *O*-polysaccharide. The rough LPS produced by deep rough mutant 595 used in the present study is composed of Lipid A and two residues of 2-keto-3-deoxy-D-manno-octonate (Kdo) in the core oligosaccharide. In contrast, the smooth LPS also contained a variable length O-polysaccharide lacking acidic residues and the portion of the core oligosaccharide between the Kdo residues and the O-polysaccharide, which includes two phosphate groups.[33,74] The core oligosaccharide of the deep rough and smooth LPS thus contained two and four negative charges, respectively.

Due to the relevance and abundance of these biomolecules at Gram-negative bacterial surfaces we investigated the effect of including rough or smooth LPS molecules in supported POPC bilayers on PAH-DNP interaction with model membranes in the absence and presence of NOM. To construct bilayers incorporating LPS, we employed the vesicle fusion method using LPS-containing POPC vesicles. Vesicles incorporating LPS exhibited more negative ζ-potentials than did those composed solely of POPC (Figure A2.3). Smooth LPS is larger and more negatively

charged than is deep rough LPS. Electrostatic and steric repulsion limits the maximum amount of smooth LPS that can be incorporated into SiO_2-supported model membranes via the vesicle fusion method to a lower mol% than can be achieved with rough LPS.[33,38] To enable direct comparison between the two types of LPS we therefore prepared bilayers from vesicles containing 0.46 mol% rough or smooth LPS. To examine the impact of rough LPS surface density on PAH-DNP attachment, we also formed bilayers from vesicles containing 6.4 mol% rLPS.

Initial rates of PAH-DNP attachment to POPC bilayers and those formed from vesicles containing 0.46 mol% rLPS or sLPS were statistically indistinguishable ($p > 0.05$; Figure 2.2a, Table A2.1) and attachment efficiencies were close to 1 (Table A2.2). This is likely attributable to the small amount of LPS incorporated into these membranes. Increasing vesicle rLPS content from 0.46 to 6.4 mol% produced a small decrease in the initial rate of PAH-DNP attachment relative to that of POPC ($p < 0.01$, Figure 2.2a, Table A2.1). Increasing the incorporation of rough LPS into vesicles by a factor of ~14 decreased the ζ-potential of the vesicles from –12.6 ± 3.6 mV to –41.7 ± 2.2 mV (Figure A2.3). We therefore hypothesize that the decrease in r_d was due to the LPS groups sterically hindering accessibility to the negative charges on the phosphatidylcholine groups of the bilayer. Values for $\Gamma_{QCM\text{-}D}$ after 20 min attachment of PAH-DNPs to POPC bilayers and those incorporating rLPS or sLPS were statistically indistinguishable ($p > 0.05$; Figure 2.2b, Table A2.8).

At a low NOM-to-DNP ratio of 1.33 $mg_{oc} \cdot mg_{PAH\text{-}DNP}^{-1}$, the initial rates and attachment efficiencies of NOM/PAH-DNPs attachment to bilayers containing 0.46 mol% rough or smooth LPS were equal to those measured in the absence of NOM ($p > 0.05$; Figure 2.2a, Table A2.1). Equivalent amounts of NOM at this ratio (5 $mg_{oc} \cdot L^{-1}$) showed little attachment to 0.46 mol% rLPS and no attachment to 0.46 mol% smooth or 6.4 mol% rough LPS. In the case of 6.4 mol% rLPS,

an increase in attachment rate was observed relative to that in the absence of NOM (p <0.0001). Acoustic surface mass densities after 20 min attachment of NOM/PAH-DNPs to all bilayers were higher at a NOM-to-DNP ratio of 1.33 $mg_{oc} \cdot mg_{PAH\text{-}DNP}^{-1}$ relative to those obtained in the absence of NOM ($p < 0.0001$; Figure 2.2b, Table A2.8). As noted in the case of POPC, the larger $\Gamma_{QCM\text{-}D}$ values may be attributable to the higher mass associated with the aggregated particles (PAH-DNPs, NOM and internal water) at this NOM-to-DNP ratio.

As we observed for POPC bilayers for NOM-to-DNP ratios of 8 $mg_{oc} \cdot mg_{PAH\text{-}DNP}^{-1}$, attachment rates to bilayers containing LPS were at least an order of magnitude lower than in the absence of NOM and indistinguishable from one another (Figure 2.2a, Table A2.1). The deposition rate of 30 $mg_{oc} \cdot L^{-1}$ NOM with no PAH-DNP (the total NOM concentration in the 8 $mg_{oc} \cdot mg_{PAH\text{-}DNP}^{-1}$ NOM-to-DNP suspensions) was similar to that observed when particles were present to all three bilayer types (Table A2.1). Furthermore, the acoustic surface mass density of the 8 $mg_{oc} \cdot mg_{PAH\text{-}DNP}^{-1}$ particles after 20 min attachment was indistinguishable from that of NOM binding to the bilayer (Table A2.8, $p > 0.05$). Therefore, we attribute the observed attachment rate and attachment for the 8 $mg_{oc} \cdot mg_{PAH\text{-}DNP}^{-1}$ particles solely to NOM binding to the 0.46 mol% rLPS and 0.46 mol% sLPS bilayers. Neither attachment of particles at NOM-to-DNP ratios of 8 $mg_{oc} \cdot mg_{PAH\text{-}DNP}^{-1}$ nor NOM itself was observed to attach to the 6.4 mol% rLPS bilayer likely due to increased electrostatic repulsion between the NOM and the more negatively charged bilayer relative to the other three studied here (Figure A2.3).

2.3.4 Natural organic matter modulates PAH-DNP impact on *Shewanella oneidensis.*

We examined the influence of NOM on the effect of PAH-DNP on the Gram-negative bacterium *Shewanella oneidensis*. A significantly higher coverage of LPS was expected on bacterial surfaces (up to 75%) than was modeled in the membrane studies; nonetheless, we

anticipated a similar trend in surface attachment to bacterial cells to be observed. We note that under the growth conditions in this study (30 °C), *S. oneidensis* elaborates only rough LPS.[33]

We employed the LIVE/DEAD assay to quantify membrane damage. This fluorescence-based method uses two fluorescent dyes that bind to nucleic acid: green-fluorescent SYTO 9 and red-fluorescent PI. Cell-permeant SYTO 9 stains all live cells; the non-permeant PI stains nucleic acids only in the cells with damaged membranes. In the absence of NOM, exposure to 1 nM PAH-DNP resulted in membrane damage to >60% of the cells (Figure 2.3a). As the NOM-to-DNP ratio increased, the proportion of cells with membrane damage remained unchanged at ratios up to 0.8 $mg_{OC} \cdot mg_{PAH\text{-}DNP}^{-1}$. A sharp increase in the proportion of cells with intact membranes was observed at ratios between 0.8 and 1.1 $mg_{OC} \cdot mg_{PAH\text{-}DNP}^{-1}$, with no observable damage above a ratio of 1.1 $mg_{OC} \cdot mg_{PAH\text{-}DNP}^{-1}$.

The impact of NOM on the toxicity to *S. oneidensis* induced by exposure to PAH-DNP exhibited a similar trend (Figure 2.3b). The toxicity of 1 nM PAH-DNP was completely ameliorated at NOM-to-DNP ratios $\geq 1.3\ mg_{OC} \cdot mg_{PAH\text{-}DNP}^{-1}$. The strong correspondence between the membrane damage and bacterial viability results displayed in Figure 2.3 was expected. Earlier studies have indicated that the toxicity of cationic polymer-wrapped nanoparticles arises largely from attachment of the positively charged particles to negatively charged bacterial surfaces leading to membrane damage.[44] The reduced toxicity and membrane damage at higher NOM-to-DNP ratios are consistent with the drastically reduced attachment of PAH-DNP to supported bilayers containing 6.4% rough LPS at NOM-to-DNP ratios of 8 $mg_{OC} \cdot mg_{PAH\text{-}DNP}^{-1}$ (Figure 2.2b). The discrepancy between the results obtained at 1.3 $mg_{OC} \cdot mg_{PAH\text{-}DNP}^{-1}$ in the whole cell and 6.4% rLPS-POPC studies may be attributable to the much higher LPS content on cell surfaces. The higher density of rLPS on the bacterial surface may have sterically hindered nanoparticle disruption of

the outer membrane. We also note that the critical NOM-to-DNP ratio that resulted in amelioration in toxicity and membrane damage by PAH-DNP occurred at a slightly lower NOM-to-DNP ratio than that of charge reversal of the nanoparticle by NOM (Figure 2.1b). An earlier study examining the attachment to and uptake by HeLa cells of an array of Au nanoparticles spanning a range of ζ-potentials found a threshold of effective surface charge density below which minimal binding occurred even when the particles exhibited positive ζ-potentials.[75] Our observations likely reflect such a threshold in effective charge density as modulated by adsorbed NOM molecules.

2.4 Environmental implications

We have demonstrated that hydrodynamic and electrokinetic properties of DNPs wrapped with the polycation PAH are altered upon interaction with NOM and that NOM influences the interaction of these nanoparticles with model cell membranes and with intact bacterial cells. As the NOM-to-DNP ratio increased the following sequence of events occurred. Initial adsorption of NOM molecules to PAH-DNP surfaces resulted in uneven charge distributions and induced attractive interactions between oppositely charged regions on adjacent particles leading to a moderate degree of aggregation. As further NOM molecules adsorbed to DNP surfaces, the probability of favorable interactions between oppositely charged regions on the DNP surfaces increased leading to higher aggregation rates. Concurrently, adsorbing NOM molecules progressively neutralized and eventually reversed the positive potential of the particles. Aggregation was promoted at NOM-to-DNP ratios producing low ζ-potentials because the electrostatic energy barrier had been lowered sufficiently to allow attractive van der Waals interactions to cause aggregation. At still higher NOM-to-DNP ratios, the amount of NOM on the particles increased and electrostatic repulsion prevented further aggregation of PAH-DNPs. The changes to PAH-DNP hydrodynamic and electrokinetic properties influenced the attachment of

these particles to model membranes and their toxicity toward a Gram-negative bacterium. Our results lead to the expectation that the influence of NOM on nanoparticle-induced effects depends on the NOM-to-nanoparticle ratio (as well as the affinity of NOM for the nanoparticle surface).

In the experiments described here, a finite amount of NOM was available to bind to the PAH-DNP. This is particularly important for the low NOM-to-DNP ratios studied because this imposes a limit on the extent of overcoating/displacement of PAH polymer in the experimental system. In the environment, the amount (mass) of NOM ultimately available would be large enough to eventually overcoat/displace the PAH polymer entirely, even at low NOM concentration. The concentration ratios of NOM to PAH-DNP studied here varied from 1.33 (for 5 $mg_{oc} \cdot L^{-1}$ NOM) to 8.0 (for 30 $mg_{oc} \cdot L^{-1}$ NOM). In typical freshwater environments the ratio of NOM to engineered nanoparticle is expected to be much larger due to the expected low concentrations of engineered nanoparticles.[17] Overcoating/displacement would occur, but more slowly at low NOM concentrations. Differences in kinetics of overcoating/displacement could have biological consequences, similar to those demonstrated here at different NOM concentrations, depending on how rapidly the nanoparticles come in contact with organismal surfaces.

The present study represents an initial demonstration of the complex influence that NOM can have on nanomaterial interactions with bacterial surfaces. The present study focused on a single type of nanoparticle (diamond) functionalized with a single capping agent (the cationic polymer poly(allylamine HCl)). In the specific system investigated, at low NOM-to-PAH-DNP ratios PAH-DNP bound to model membranes and elicited membrane damage in the bacteria. Higher ratios, which caused reversal of the charge of the polymer-wrapped nanodiamond, reduced attachment to the model membranes and damage to bacterial membranes. Effects similar to those

we observed at high NOM concentrations have been reported for nanoscale zero-valent iron to *Escherichia coli*,[29] although the mechanism of toxicity likely differed. We expect our results to be most directly transferable to positively charged natural colloids and engineered nanoparticles functionalized with cationic polymers[17,35] and ligands[14,35,76-77]. We hypothesize that NOM overcoating/replacement of ligands occurs at the high NOM-to-nanoparticle ratios expected in the environment; in environments with low NOM concentrations, this would occur at slower rates than observed in the present study. Future studies are needed to understand the influence of NOM properties and divalent cations on nanomaterial interactions with cell surfaces in the presence of NOM.

2.5 Figures

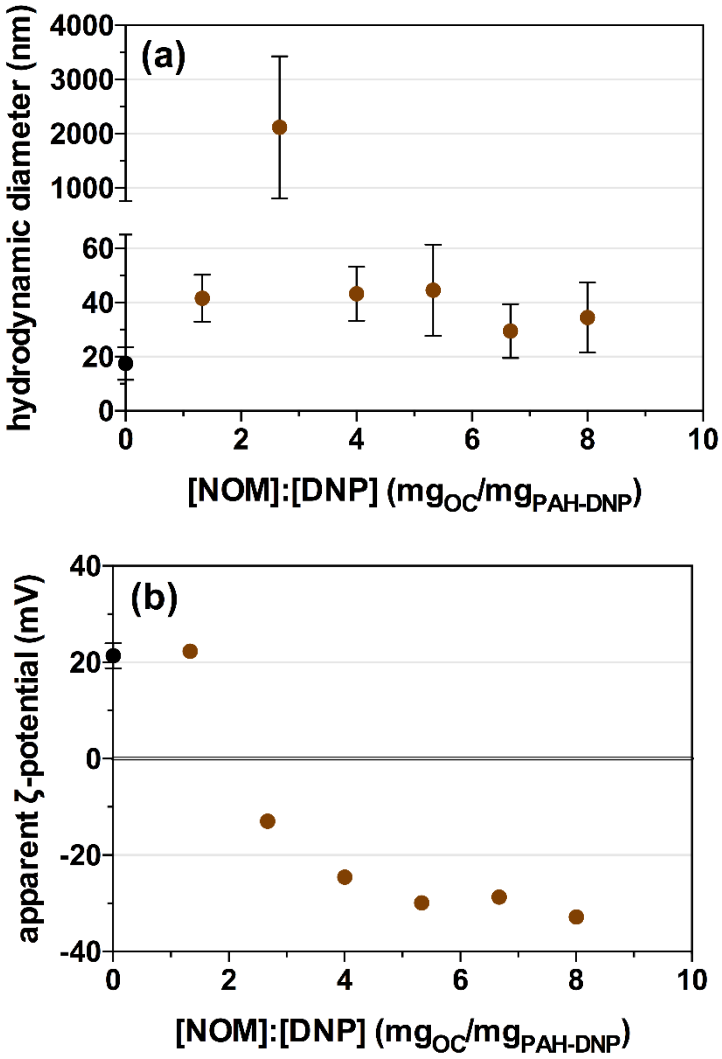

Figure 2.1. PAH-DNP (a) number-averaged hydrodynamic diameters and (b) apparent ζ-potentials as a function of Suwannee River NOM-to-nanoparticle concentration ratio in 0.025 M NaCl buffered to pH 7.4 with 0.002 M HEPES. Error bars represent one standard deviation of five replicate measurements. In some cases error bars in the apparent ζ-potential plot fall within the size of the marker.

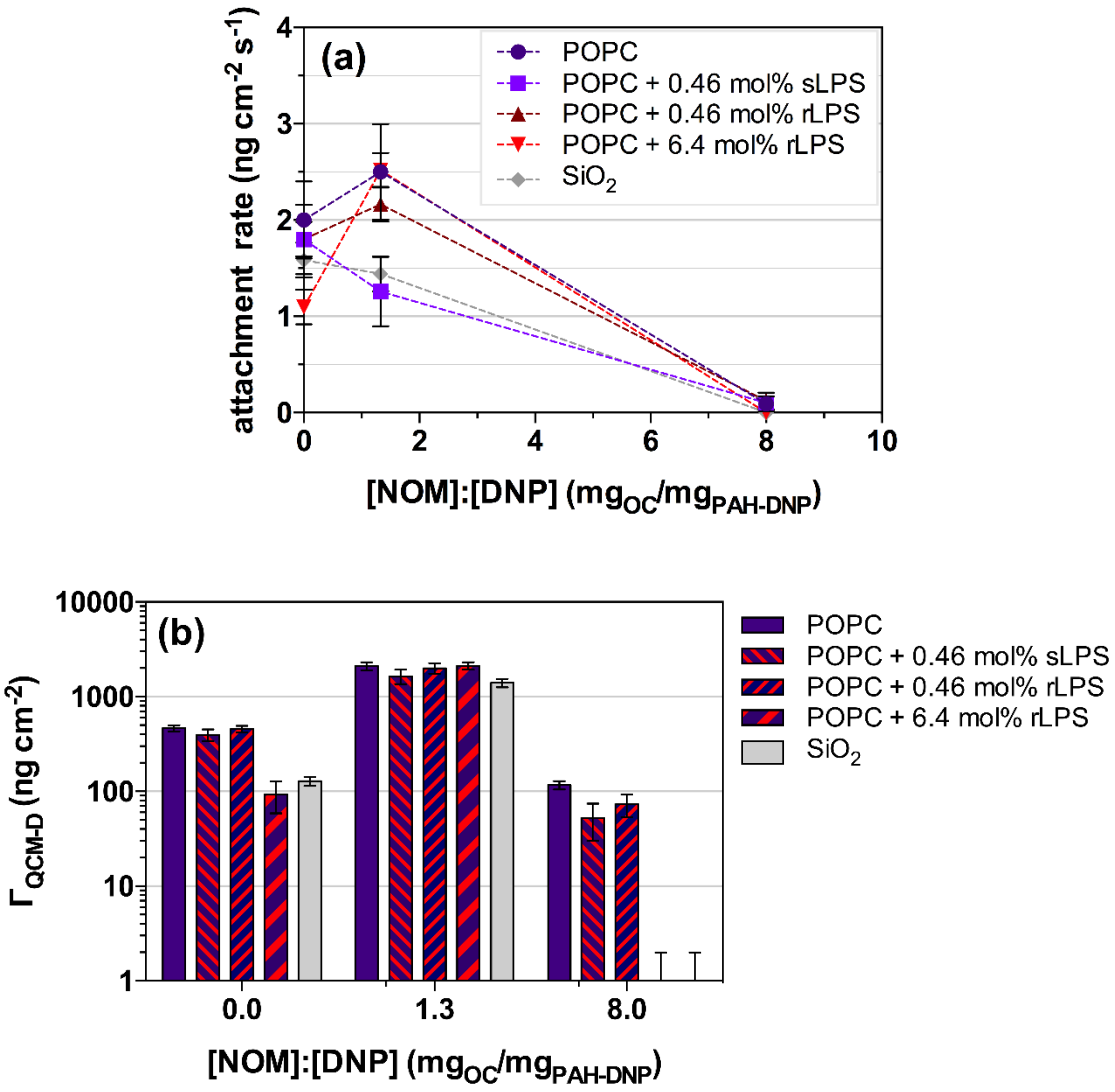

Figure 2.2. Natural organic matter (NOM) influences the attachment of PAH-DNP to supported lipid bilayers composed of the zwitterionic phospholipid POPC alone or with the indicated amounts of smooth or rough lipopolysaccharide (LPS). (a) Initial rates of PAH-DNP attachment to and (b) acoustic surface mass density (Γ_{QCM-D}) at 20 min for the indicated bilayers and SiO_2 as a function of NOM concentration. Attachment rates defined as the first derivative of the change in acoustic surface mass density with respect to time over the first 30 seconds of attachment. Dotted lines are to guide the eye. Acoustic surface mass densities calculated from the Sauerbrey equation[50] (in all cases $\Delta D_n/(\Delta f_n/n) < 0.4 \times 10^{-6}$ Hz^{-1})[49]. Symbols represent means of at least triplicate

measurements; error bars denote one standard deviation. Experiments used 1 nM (number concentration) of PAH-DNPs in 0.025 M NaCl buffered to pH 7.4 with 0.002 M HEPES with the indicated amount of Suwannee River NOM at 25 °C. Numerical data for initial attachment rates and $\Gamma_{QCM\text{-}D}$ are presented in Tables A2.1 and A2.8, respectively. Abbreviations: PAH-DNP, diamond nanoparticles functionalized with poly(allylamine HCl); POPC, 1-palmitoyl-2-oleoyl-*sn*-glycero-3-phosphocholine; rLPS, rough lipopolysaccharide; sLPS, smooth lipopolysaccharide.

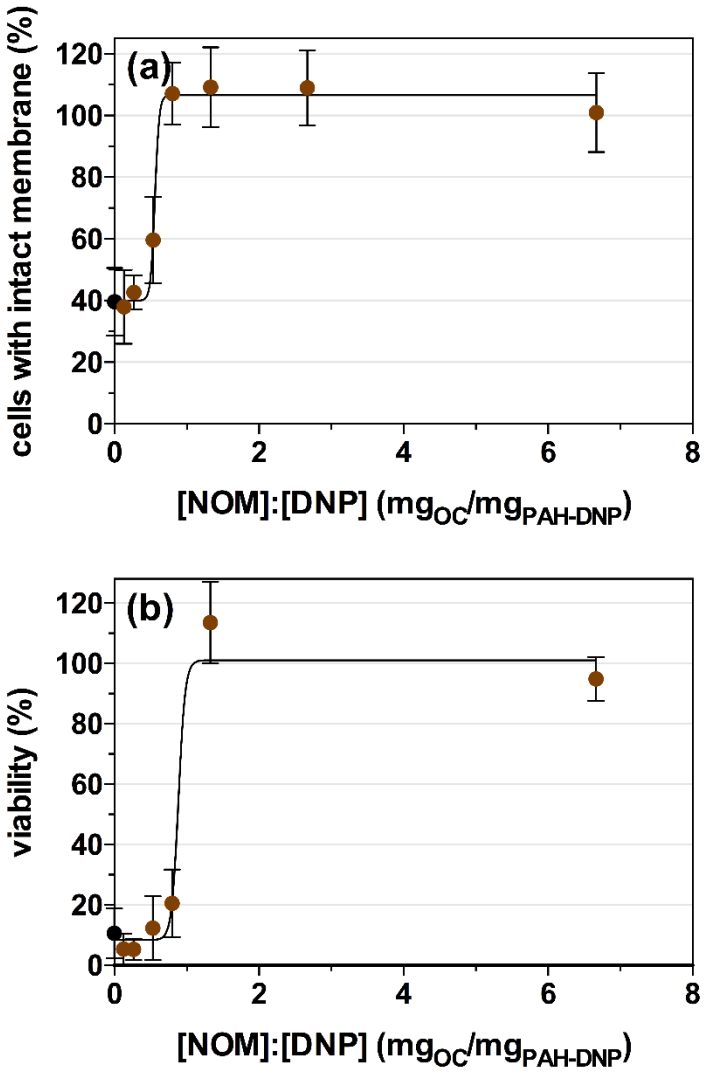

Figure 2.3. The influence of NOM-to-DNP ratio on (a) membrane damage and (b) toxicity to *Shewanella oneidensis* by 1 nM PAH-DNP. Experiments were performed in 0.025 M NaCl buffered with 0.002 M HEPES to pH 7.4.

2.6 References

1. Nel, A.; Xia, T.; Madler, L.; Li, N. Toxic potential of materials at the nanolevel. *Science,* **2006,** *311,* 622-627.

2. Maurer-Jones, M. A.; Gunsolus, I. L.; Murphy, C. J.; Haynes, C. L. Toxicity of engineered nanoparticles in the environment. *Anal Chem,* **2013,** *85,* 3036-3049.

3. Mudunkotuwa, I. A.; Grassian, V. H. The devil is in the details (or the surface): Impact of surface structure and surface energetics on understanding the behavior of nanomaterials in the environment. *J. Environ. Monit.,* **2011,** *13,* 1135-1144.

4. Lundqvist, M.; Stigler, J.; Elia, G.; Lynch, I.; Cedervall, T.; Dawson, K. A. Nanoparticle size and surface properties determine the protein corona with possible implications for biological impacts. *Proc. Natl. Acad. Sci. U.S.A.,* **2008,** *105,* 14265-14270.

5. Sani-Kast, N.; Labille, J.; Ollivier, P.; Slomberg, D.; Hungerbuhler, K.; Scheringer, M. A network perspective reveals decreasing material diversity in studies on nanoparticle interactions with dissolved organic matter. *Proc. Natl. Acad. Sci. U.S.A.,* **2017,** *114,* 1756.

6. Sutton, R.; Sposito, G. Molecular structure in soil humic substances: The new view. *Environ. Sci. Technol.,* **2005,** *29,* 9009-9015.

7. Thurman, E. M., *Organic geochemistry of natural waters*. Martinus Nijhoff/Dr. W. Junk Publishers: Dordrecht, 1985.

8. Jones, M. N.; Bryan, N. D. Colloidal properties of humic substances. *Adv. Colloid Interface Sci.,* **1998,** *78,* 1-48.

9. Ritchie, J. D.; Perdue, E. M. Proton-binding study of standard and reference fulvic acids, humic acids, and natural organic matter. *Geochim. Cosmochim. Acta,* **2003,** *67,* 85-96.

10. Louie, S. M.; Tilton, R. D.; Lowry, G. V. Critical review: Impacts of macromolecular coatings on critical physicochemical processes controlling environmental fate of nanomaterials. *Environ. Sci.: Nano,* **2016,** *3,* 283-310.

11. Peijnenburg, W. J. G. M.; Baalousha, M.; Chen, J.; Chaudry, Q.; Von der kammer, F.; Kuhlbusch, T. A. J.; Lead, J.; Nickel, C.; Quik, J. T. K.; Renker, M.; Wang, Z.; Koelmans, A. A. A review of the properties and processes determining the fate of engineered nanomaterials in the aquatic environment. *Crit. Rev. Env. Sci. Technol.,* **2015,** *45,* 2084-2134.

12. Grillo, R.; Rosa, A. H.; Fraceto, L. F. Engineered nanoparticles and organic matter: A review of the state-of-the-art. *Chemosphere,* **2015,** *119,* 608-619.

13. Philippe, A.; Schaumann, G. E. Interactions of dissolved organic matter with natural and engineered inorganic colloids: A review. *Environ. Sci. Technol.,* **2014,** *48,* 8946-8962.

14. Stankus, D. P.; Lohse, S. E.; Hutchison, J. E.; Nason, J. A. Interactions between natural organic matter and gold nanoparticles stabilized with different organic capping agents. *Environ. Sci. Technol.,* **2011,** *45,* 3238-3244.

15. Kretzschmar, R.; Sticher, H. Transport of humic-coated iron oxide colloids in a sandy soil: Influence of Ca^{2+} and trace metals. *Environ. Sci. Technol.,* **1997,** *31,* 3497-3504.

16. Loosli, F.; Le Coustumer, P.; Stoll, S. TiO_2 nanoparticles aggregation and disaggregation in presence of alginate and Suwannee River humic acids. pH and concentration effects on nanoparticle stability. *Water Res.,* **2013,** *47,* 6052-6063.

17. Surette, M. C.; Nason, J. A. Effects of surface coating character and interactions with natural organic matter on the colloidal stability of gold nanoparticles. *Environ. Sci.: Nano,* **2016,** *3,* 1144-1152.

18. Lau, B. L. T.; Hockaday, W. C.; Ikuma, K.; Furman, O.; Decho, A. W. A preliminary assessment of the interactions between the capping agents of silver nanoparticles and environmental organics. *Colloids Surf., A,* **2013,** *435,* 22-27.

19. Zhang, W.; Rattanaudompol, U.; Li, H.; Bouchard, D. Effects of humic and fulvic acids on aggregation of aqu/nC_{60} nanoparticles. *Water Res.,* **2013,** *47,* 1793-1802.

20. Erhayem, M.; Sohn, M. Stability studies for titanium dioxide nanoparticles upon adsorption of Suwannee River humic and fulvic acids and natural organic matter. *Sci. Total Environ.,* **2014,** *468-469,* 249-257.

21. Furman, O.; Usenko, S.; Lau, B. L. Relative importance of the humic and fulvic fractions of natural organic matter in the aggregation and deposition of silver nanoparticles. *Environ. Sci. Technol.,* **2013,** *47,* 1349-1356.

22. Louie, S. M.; Tilton, R. D.; Lowry, G. V. Effects of molecular weight distribution and chemical properties of natural organic matter on gold nanoparticle aggregation. *Environ. Sci. Technol.,* **2013,** *47,* 4245-4254.

23. Louie, S. M.; Spielman-Sun, E. R.; Small, M. J.; Tilton, R. D.; Lowry, G. V. Correlation of the physicochemical properties of natural organic matter samples from different sources to their effects on gold nanoparticle aggregation in monovalent electrolyte. *Environ. Sci. Technol.,* **2015,** *49,* 2188-2198.

24. Gunsolus, I. L.; Mousavi, M. P.; Hussein, K.; Buhlmann, P.; Haynes, C. L. Effects of humic and fulvic acids on silver nanoparticle stability, dissolution, and toxicity. *Environ. Sci. Technol.,* **2015,** *49,* 8078-8086.

25. Yin, Y.; Shen, M.; Tan, Z.; Yu, S.; Liu, J.; Jiang, G. Particle coating-dependent interaction of molecular weight fractionated natural organic matter: Impacts on the aggregation of silver nanoparticles. *Environ. Sci. Technol.,* **2015,** *49,* 6581-6589.

26. Nason, J. A.; McDowell, S. A.; Callahan, T. W. Effects of natural organic matter type and concentration on the aggregation of citrate-stabilized gold nanoparticles. *J. Environ. Monit.,* **2012,** *14,* 1885-1892.

27. Liu, J.; Legros, S.; von der Kammer, F.; Hofmann, T. Natural organic matter concentration and hydrochemistry influence aggregation kinetics of functionalized engineered nanoparticles. *Environ. Sci. Technol.,* **2013,** *47,* 4113-4120.

28. Ha, Y.; Wang, X.; Liljestrand, H. M.; Maynard, J. A.; Katz, L. E. Bioavailability of fullerene under environmentally relevant conditions: Effects of humic acid and fetal bovine serum on accumulation in lipid bilayers and cellular uptake. *Environ. Sci. Technol.,* **2016,** *50,* 6717-6727.

29. Li, Z.; Greden, K.; Alvarez, P. J. J.; Gregory, K. B.; Lowry, G. V. Adsorbed polymer and NOM limits adhesion and toxicity of nano scale zerovalent iron to *E. coli*. *Environ. Sci. Technol.,* **2010,** *44,* 3462-3467.

30. Chen, K. L.; Bothun, G. D. Nanoparticles meet cell membranes: Probing nonspecific interactions using model membranes. *Environ. Sci. Technol.,* **2014,** *48,* 873-880.

31. Liu, X.; Chen, K. L. Interactions of graphene oxide with model cell membranes: Probing nanoparticle attachment and lipid bilayer disruption. *Langmuir,* **2015,** *31,* 12076-12086.

32. Rascol, E.; Devoisselle, J. M.; Chopineau, J. The relevance of membrane models to understand nanoparticles-cell membrane interactions. *Nanoscale,* **2016,** *8,* 4780-4798.

33. Jacobson, K. H.; Gunsolus, I. L.; Kuech, T. R.; Troiano, J. M.; Melby, E. S.; Lohse, S. E.; Hu, D.; Chrisler, W. B.; Murphy, C. J.; Orr, G.; Geiger, F. M.; Haynes, C. L.; Pedersen, J. A. Lipopolysaccharide density and structure govern the extent and distance of nanoparticle interaction with actual and model bacterial outer membranes. *Environ. Sci. Technol.,* **2015,** *49,* 10642-10650.

34. Troiano, J. M.; Olenick, L. L.; Kuech, T. R.; Melby, E. S.; Hu, D.; Lohse, S. E.; Mensch, A. C.; Dogangun, M.; Vartanian, A. M.; Torelli, M. D.; Ehimiaghe, E.; Walter, S. R.; Fu, L.; Anderton, C. R.; Zhu, Z.; Wang, H.; Orr, G.; Murphy, C. J.; Hamers, R. J.; Pedersen, J. A.; Geiger, F. M. Direct probes of 4 nm diameter gold nanoparticles interacting with supported lipid bilayers. *J. Phys. Chem. C,* **2015,** *119,* 534-546.

35. Leroueil, P. R.; Berry, S. A.; Duthie, K.; Han, G.; Rotello, V. M.; McNerny, D. Q.; Jr., J. R. B.; Orr, B. G.; Holl, M. M. B. Wide varieties of cationic nanoparticles induce defects in supported lipid bilayers. *Nano Lett.,* **2008,** *8,* 420-424.

36. Melby, E. S.; Mensch, A. C.; Lohse, S. E.; Hu, D.; Orr, G.; Murphy, C. J.; Hamers, R. J.; Pedersen, J. A. Formation of supported lipid bilayers containing phase-segregated domains and their interaction with gold nanoparticles. *Environ. Sci.: Nano,* **2016,** *3,* 45-55.

37. Le Brun, A. P.; Clifton, L. A.; Halbert, C. E.; Lin, B.; Meron, M.; Holden, P. J.; Lakey, J. H.; Holt, S. A. Structural characterization of a model Gram-negative bacterial surface using

lipopolysaccharides from rough strains of *Escherichia coli*. *Biomacromolecules,* **2013,** *14,* 2014-2022.

38. Kaufmann, S.; Ilg, K.; Mashaghi, A.; Textor, M.; Priem, B.; Aebi, M.; Reimhult, E. Supported lipopolysaccharide bilayers. *Langmuir,* **2012,** *28,* 12199-12208.

39. Krueger, A. Diamond nanoparticles: Jewels for chemistry and physics. *Adv. Mater.,* **2008,** *20,* 2445-2449.

40. Shakun, A.; Vuorinen, J.; Hoikkanen, M.; Poikelispää, M.; Das, A. Hard nanodiamonds in soft rubbers: Past, present and future – a review. *Composites Part A: Applied Science and Manufacturing,* **2014,** *64,* 49-69.

41. Mochalin, V. N.; Shenderova, O.; Ho, D.; Gogotsi, Y. The properties and applications of nanodiamonds. *Nat. Nanotechnol.,* **2011,** *7,* 11-23.

42. Stavis, C.; Clare, T. L.; Butler, J. E.; Radadia, A. D.; Carr, R.; Zeng, H.; King, W. P.; Carlisle, J. A.; Aksimentiev, A.; Bashir, R.; Hamers, R. J. Surface functionalization of thin-film diamond for highly stable and selective biological interfaces. *Proc. Natl. Acad. Sci. U.S.A.,* **2011,** *108,* 983-988.

43. Bozich, J. S.; Lohse, S. E.; Torelli, M. D.; Murphy, C. J.; Hamers, R. J.; Klaper, R. D. Surface chemistry, charge and ligand type impact the toxicity of gold nanoparticles to *Daphnia magna*. *Environ. Sci.: Nano,* **2014,** *1,* 260-270.

44. Feng, Z. V.; Gunsolus, I. L.; Qiu, T. A.; Hurley, K. R.; Nyberg, L. H.; Frew, H.; Johnson, K. P.; Vartanian, A. M.; Jacob, L. M.; Lohse, S. E.; Torelli, M. D.; Hamers, R. J.; Murphy, C. J.; Haynes, C. L. Impacts of gold nanoparticle charge and ligand type on surface binding and toxicity to Gram-negative and Gram-positive bacteria. *Chem. Sci.,* **2015,** *6,* 5186-5196.

45. Brezonik, P. L.; Arnold, W. A., *Water chemistry: An introduction o the chemistry of natural and engineered aquatic systems*. Oxford University Press: New York, 2011.

46. Malvern Instruments. *Intensity-volume-number: What size is correct*; Technical Note MRK1357-01.

47. Smoluchowski, M. V., Handbuchder elektrizitat und des magnetismus. In *Electrische endosmose und stro-mungsstrome*, Greatz, L., Ed. Barth: Leipzig, 1921; Vol. 2, pp 62-366.

48. Ohshima, H. Electrokinetics of soft particles. *Colloid. Polym. Sci.,* **2007,** *285,* 1411-1421.

49. Reviakine, I.; Johannsmann, D.; Richter, R. P. Hearing what you cannot see and visualizing what you hear: Interpreting quartz crystal microbalance data from solvated interfaces. *Anal. Chem.,* **2011,** *83,* 8838-8848.

50. Sauerbrey, G. Verwendung von schwingquarzen zur wagung dunner schichten und zur mikrowagung. *Zeitschrift Fur Physik,* **1959,** *155,* 206-222.

51. Cho, N. J.; Kanazawa, K. K.; Glenn, J. S.; Frank, C. W. Employing two different quartz crystal microbalance models to study changes in viscoelastic behavior upon transformation of lipid vesicles to a bilayer on a gold surface. *Anal. Chem.,* **2007,** *79,* 7027-7035.

52. Quevedo, I. R.; Olsson, A. L.; Tufenkji, N. Deposition kinetics of quantum dots and polystyrene latex nanoparticles onto alumina: Role of water chemistry and particle coating. *Environ. Sci. Technol.,* **2013,** *47,* 2212-2220.

53. Chen, K. L.; Elimelech, M. Interaction of fullerene (C_{60}) nanoparticles with humic acid and alginate coated silica surfaces: Measurements, mechanisms, and environmental implications. *Environ. Sci. Technol.,* **2008,** *42,* 7607-7614.

54. Quevedo, I. R.; Tufenkji, N. Influence of solution chemistry on the deposition and detachment kinetics of a CdTe quantum dot examined using a quartz crystal microbalance. *Environ. Sci. Technol.,* **2009,** 3176-3182.

55. Richter, R.; Mukhopadhyay, A.; Brisson, A. Pathways of lipid vesicle deposition on solid surfaces: A combined QCM-D and AFM study. *Biophys. J.,* **2003,** *85,* 3035-3047.

56. Keller, C. A.; Kasemo, B. Surface specific kinetics of lipid vesicle adsorption measured with a quartz crystal microbalance. *Biophys. J.,* **1998,** *75,* 1397-1402.

57. Qiu, T. A.; Nguyen, T. H.; Hudson-Smith, N. V.; Clement, P. L.; Forester, D. C.; Frew, H.; Hang, M. N.; Murphy, C. J.; Hamers, R. J.; Feng, Z. V.; Haynes, C. L. Growth-based bacterial viability assay for interference-free and high-throughput toxicity screening of nanomaterials. *Anal. Chem.,* **2017,** *89,* 2057-2064.

58. Gregory, J. Rates of flocculation of latex particles by cationic polymers. *J. Colloid Interface Sci.,* **1973,** *42,* 448-456.

59. Yu, W. L.; Bouyer, F.; Borkovec, M. Polystyrene sulfate latex particles in the presence of poly(vinylamine): Absolute aggregation rate constants and charging behavior. *J. Colloid Interface Sci.,* **2001,** *241,* 392-399.

60. Elimelech, M.; Nagai, M.; Ko, C.-H.; Ryan, J. N. Relative insignificance of mineral grain zeta potential to colloid transport in geochemically heterogeneous porous media. *Environ. Sci. Technol.,* **2000,** *34,* 2143-2148.

61. Jones, E. H.; Su, C. Transport and retention of zinc oxide nanoparticles in porous media: Effects of natural organic matter versus natural organic ligands at circumneutral pH. *J. Hazard. Mater.,* **2014,** *275,* 79-88.

62. Han, Y.; Kim, D.; Hwang, G.; Lee, B.; Eom, I.; Kim, P. J.; Tong, M.; Kim, H. Aggregation and dissolution of ZnO nanoparticles synthesized by different methods: Influence of ionic strength and humic acid. *Colloids Surf., A,* **2014,** *451,* 7-15.

63. Zimmermann, R.; Kuttner, D.; Renner, L.; Kaufmann, M.; Zitzmann, J.; Muller, M.; Werner, C. Charging and structure of zwitterionic supported bilayer lipid membranes studied by

streaming current measurements, fluorescence microscopy, and attenuated total reflection Fourier transform infrared spectroscopy. *Biointerphases*, **2009,** *4*, 1-6.

64. Chen, K. L.; Elimelech, M. Aggregation and deposition kinetics of fullerene (C_{60}) nanoparticles. *Langmuir*, **2006,** *22*, 10994-11001.

65. Zhang, X.; Yang, S. Nonspecific adsorption of charged quantum dots on supported zwitterionic lipid bilayers: Real-time monitoring by quartz crystal microbalance with dissipation. *Langmuir*, **2011,** *27*, 2528-2535.

66. Moghadam, B. Y.; Hou, W. C.; Corredor, C.; Westerhoff, P.; Posner, J. D. Role of nanoparticle surface functionality in the disruption of model cell membranes. *Langmuir*, **2012,** *28*, 16318-16326.

67. Kuech, T. R. Biological interactions and environmental transformations of nanomaterials. Ph. D. Dissertation, University of Wisconsin-Madison, 2015.

68. Troiano, J. M.; Kuech, T. R.; Vartanian, A. M.; Torelli, M. D.; Sen, A.; Jacob, L. M.; Hamers, R. J.; Murphy, C. J.; Pedersen, J. A.; Geiger, F. M. On electronic and charge interference in second harmonic generation responses from gold metal nanoparticles at supported lipid bilayers. *J. Phys. Chem. C*, **2016,** *120*, 20659-20667.

69. Zhang, M.; Soto-Rodríguez, J.; Chen, I. C.; Akbulut, M. Adsorption and removal dynamics of polymeric micellar nanocarriers loaded with a therapeutic agent on silica surfaces. *Soft Matter*, **2013,** *9*, 10155.

70. Frost, R.; Jonsson, G. E.; Chakarov, D.; Svedhem, S.; Kasemo, B. Graphene oxide and lipid membranes: Interactions and nanocomposite structures. *Nano Lett.*, **2012,** *12*, 3356-3362.

71. Kirschner, K. N.; Lins, R. D.; Maass, A.; Soares, T. A. A glycam-based force field for simulations of lipopolysaccharide membranes: Parametrization and validation. *J. Chem. Theory Comput.*, **2012,** *8*, 4719-4731.

72. Clifton, L. A.; Holt, S. A.; Hughes, A. V.; Daulton, E. L.; Arunmanee, W.; Heinrich, F.; Khalid, S.; Jefferies, D.; Charlton, T. R.; Webster, J. R.; Kinane, C. J.; Lakey, J. H. An accurate *in vitro* model of the *E. coli* envelope. *Angew. Chem. Int. Ed.*, **2015,** *54*, 11952-11955.

73. Nikaido, H. Molecular basis of bacterial outer membrane permeability revisited. *Microbiology and Molecular Biology Reviews*, **2003,** *67*, 593-656.

74. Liu, B.; Knirel, Y. A.; Feng, L.; Perepelov, A. V.; Senchenkova, S. N.; Reeves, P. R.; Wang, L. Structural diversity in *Salmonella* O antigens and its genetic basis. *FEMS Microbiol. Rev.*, **2014,** *38*, 56-89.

75. Su, G.; Zhou, H.; Mu, Q.; Zhang, Y.; Li, L.; Jiao, P.; Jiang, G.; Yan, B. Effective surface charge density determines the electrostatic attraction between nanoparticles and cells. *J. Phys. Chem. C*, **2012,** *116*, 4993-4998.

76. You, C. C.; Miranda, O. R.; Gider, B.; Ghosh, P. S.; Kim, I. B.; Erdogan, B.; Krovi, S. A.; Bunz, U. H.; Rotello, V. M. Detection and identification of proteins using nanoparticle-fluorescent polymer 'chemical nose' sensors. *Nat. Nanotechnol.,* **2007,** *2,* 318-323.

77. Goodman, C. M.; McCusker, C. D.; Yilmaz, T.; Rotello, V. M. Toxicity of gold nanoparticles functionalized with cationic and anionic side chains. *Bioconjugate Chem.,* **2004,** *15,* 897-900.

Chapter 3: Quaternary-Amine Terminated Quantum Dots Induce Structural Changes to Supported Lipid Bilayers

A manuscript of this work is in preparation and will be submitted to *Langmuir*

3.1 Introduction

With the increase in the use of nanotechnology comes a concern over the release of engineered nanomaterials into the environment and interactions that may occur with various organisms. However, understanding the impact of nanomaterials on organisms at a mechanistic level is difficult and requires a systematic approach using various analytical tools.[1-2] One strategy to begin to understand the impact of nanomaterials is to study their interactions with the cellular membrane, which is likely the first point of contact between an organism and an engineered nanomaterial. Interaction between nanomaterials and the cellular membrane is a crucial step in causing toxicity to different microorganisms,[3-5] and thus warrants further investigation with various types of nanomaterials and membranes.

Supported lipid bilayers (SLBs) are often used as a model system to study the complex interactions between nanomaterials and cellular membranes.[6-9] While SLBs may not provide all of the complexity associated with full organism studies, they allow systematic control of the chemistry of the lipid systems and enable the use of *in situ* analytical techniques to probe these interactions in environmentally relevant conditions. There are many proposed interactions that can occur between a nanomaterial and a cellular membrane, many of which can be studied using SLBs, including hole formation,[9-11] membrane thinning,[9] structural changes,[12-14] and nanoparticle internalization.[15-16] Furthermore, the phase of the lipid bilayer has been shown to play a crucial role in the interactions between nanomaterials and supported lipid bilayers. Chemical manipulation of SLBs to include liquid-ordered domains, composed of cholesterol and sphingomyelin, caused

an increase in attachment of positively-charged gold nanoparticles as compared to solely liquid-disordered bilayers.[6] Conversely, polycationic polymers were shown to preferentially interact with the liquid-disordered phase of the bilayer.[17] Also, disruption of membrane integrity was shown to vary, depending on the phase of the bilayer, upon interaction with dendrimers.[14] Previous work has used atomic force microscopy to investigate the complex interactions between polymers[17] and dendrimers[14,18] as model nanomaterial systems on SLBs; however, the complexity of the cellular membrane and increased use of nanomaterials of technological relevance present a need study various nanomaterial types and incorporate important biomolecules found in cellular membranes into model systems.

Quantum dots are a good system to use in investigating the impacts of nanomaterials with SLBs due to their technological relevance. They are used commonly in solar cells,[19] bioimaging,[20] and sensors[21] due to their unique optical and electronic properties. Quantum dots are typically composed of a metalloid crystalline core, a protective shell that shields the core, and a second coating or ligand to make the quantum dot biologically compatible or water stable.[22] They have been shown previously to adsorb to[23-24] and/or penetrate through cell membranes.[23,25]. However, the structural impacts of functionalized quantum dots on cellular membranes in real time are not well understood and warrant future investigation through the use of complementary, *in situ* analytical techniques.

The objectives of this study were to investigate the impact of cadmium selenide (CdSe) quantum dots with a zinc sulfide (ZnS) shell functionalized with poly(diallyldimethylammonium chloride) (PDDA) to SLBs of various composition. We chose this particular quantum dot because of the technological relevance of CdSe/ZnS quantum dots[19-20] and due to the impact that other types of cationic nanomaterials have had on model bilayers.[6,9,26-27] Due to the importance of bilayer

fluidity on these interactions, we studied bilayers composed of purely a liquid-disordered (L_d) phase and bilayers composed of both liquid-disordered and liquid-ordered phases through the inclusion of sphingomyelin and cholesterol into the SLBs. We used three complementary *in situ* analytical techniques, quartz crystal microbalance with dissipation monitoring (QCM-D), nanoplasmonic sensing (NPS), and atomic force microscopy (AFM), to gain mechanistic insights into the interactions between the quantum dots and the lipid bilayers in real time. We used QCM-D and NPS to probe attachment of PDDA-QDs to SLBs as well as investigate any structural changes to the bilayer as monitored by dissipation changes. To further our insights into these interactions and the time scale of these interactions, we used AFM to examine the structure of the bilayer before and after interaction with the quantum dots. Together, these three complementary, *in situ*, approaches provide new insights into the complex interactions that occur between functionalized quantum dots and cellular membranes.

3.2 Materials and Methods

3.2.1 Quantum dot characterization

Cadmium selenide core quantum dots (QD) with a zinc sulfide shell and a positively-charged poly(diallyldimethylammonium chloride) (PDDA) polymer wrapping were procured from OceanNanotech (QSQ-620). The polymer wrapping ensured water stability and allowed us to probe the impact of a positively charged particle on the lipid bilayers. We measured the diffusivities and electrophoretic mobilities of the PDDA-QDs by dynamic light scattering and laser Doppler microelectrophoresis (Malvern Zetasizer Nano ZS) at a 1 nM number concentration of QDs 0.010 M NaCl buffered to pH 7.4 with 0.010 M HEPES. The diffusivity and electrophoretic mobility measurements are the average of five measurements. We used the Stokes-Einstein equation to find the intensity-averaged hydrodynamic diameters from the diffusivity

measurements and from these values estimated the hydrodynamic diameter (d_h) using Mie theory.[28] We estimated the ζ-potentials of the PDDA-QDs from the measured electrophoretic mobility using the Smoluchowski approximation.[29] However, this approximation assumes that the particle is a hard sphere. In the case of the polymer-wrapped quantum dots used in this study, we have an ion-permeable soft shell on a hard core-shell particle making the measured ζ-potentials apparent values.[29-30]

3.2.2 Lipid vesicle preparation and characterization

We prepared small unilamellar (SUVs) composed solely of 1,2-dioleoyl-*sn*-glycero-3-phosphocholine (DOPC, 850375C, Avanti Polar Lipids) or DOPC with plant-derived cholesterol (Chol, 700100P, Avanti Polar Lipids) and sphingomyelin from chicken egg yolk (SM, S0756, Sigma Aldrich) as previously described.[6] Briefly, stock solutions of Chol and SM were dissolved in chloroform (1 mg/mL) and sonicated for 30 min. The three components were mixed to the desired ratio (100% DOPC or 60/20/20 mol% DOPC/SM/Chol), the chloroform was removed under a stream of nitrogen gas, and any residual chloroform was removed under vacuum overnight. The dried film was rehydrated in 0.001 M NaCl buffered to pH 7.4 with 0.01 M HEPES and vortexed and sonicated for 30 min to leave a cloudy solution. Following, three cycles of freezing with liquid nitrogen and thawing by sonication the solution was extruded 11 times (Avanti 610000 extruder kit) through a 50 nm polycarbonate membrane filter (Whatman) to give small unilamellar vesicles (SUVs). All extruded vesicles were stored at 4 °C and used within one week of extrusion.

3.2.3 Quartz crystal microbalance with dissipation monitoring (QCM-D) coupled with nanoplasmonic sensing

Quartz crystal microbalance with dissipation monitoring measures changes in resonance frequency (Δf) and changes in dissipation (ΔD) due to the interaction of an analyte (PDDA-QDs

in our case) with the surface of an AT-cut quartz crystal. Detected changes in frequency are related to the amount of mass due to the analyte and any hydrodynamically coupled water at the sensor surface, whereas changes in the energy dissipation are related to any changes in the viscoelastic properties of the surface.[31] To discern, the optical, or "dry" mass associated with these interactions, NPS was used in combination with QCM-D. The combined technique works by using a QCM-D crystal containing nanoplasmonic gold discs with a ~10 nm thick silicon nitride layer deposited on top of the nanoplasmonic features. Light via a fiber optic cable induces charge density oscillations in the gold discs, resulting in a localized surface plasmon resonance (LSPR). Monitoring of the changes to the maximum extinction wavelength $\Delta\lambda_{max}$, due to any changes in the local refractive index, allows for an optical mass to be determined. Here, we used QCM-D in combination with NPS to monitor the formation of supported lipid bilayers and the changes in frequency, energy dissipation, and $\Delta\lambda_{max}$ induced by exposure to PDDA-QDs in real time. This allowed for the detection of any changes in optical ("dry") and acoustic ("wet") mass associated with interactions at the sensor surface.

Prior to use, a Si_3N_4-coated QCM-D crystal with nanoplasmonic gold discs (Batch No. 100-1705-01, Insplorion AB, Göteborg, Sweden) was soaked in a 2% sodium dodecyl sulfate solution for 10 min, rinsed three times alternatively with ultrapure water and ethanol, dried with N_2 gas, and exposed to UV/ozone from a low-pressure mercury lamp for 10 min (Bioforce Nanosciences UV/Ozone Procleaner, 185 and 254 nm). The crystals were then immediately loaded into a window cell module (QWM401, Biolin Scientific). The cell was filled with water and the Insplorion Acoulyte (Insplorion AB, Göteborg, Sweden) was mounted on top of the window cell. The centroid range (60nm) of the plasmon excitation peak was determined by sweeping a range of wavelengths from 550-850 nm and selecting the center of the plasmon excitation peak. This peak

wavelength was monitored for shifts, due to changes in refractive index, throughout the formation of bilayers as well as interactions with PDDA-QDs.

We formed supported lipid bilayers on the Si_3N_4 sensor from SUVs composed of purely DOPC or 60/20/20 mol% DOPC/SM/Chol using the vesicle fusion method.[6,32] The sensor was equilibrated in ultrapure water (18.2 MΩ·cm resistivity, Barnstead GenPure Pro) until a stable baseline was reached. At which point the solution was switched to 0.150 M NaCl buffered to pH 7.4 with 0.010 M HEPES (pH and buffer concentration used throughout) and flowed until a stable baseline was reached (~10 min). A solution of vesicles (0.03125 $mg \cdot mL^{-1}$) in the same buffer were flowed (0.100 $mL \cdot min^{-1}$) over the surface until the critical surface vesicle concentration[33] was attained, at which point, the vesicles ruptured and fused to form a bilayer. Any loosely adsorbed vesicles were rinsed away and a stable baseline was established by rinsing with vesicle free buffer. The ionic strength of the solution was lowered to 0.010 M NaCl by rinsing the bilayer with buffer at this lower ionic strength until the frequency, dissipation, and λ_{max} values stabilized.

Suspensions of 1 nM PDDA-QDs in 0.010 M NaCl were vortexed and immediately flowed over the bilayers. Attachment was monitored for 20 min followed by a rinse with nanoparticle-free solution to examine the reversibility of the interaction and any observed changes upon rinse. Control experiments were conducted examining interaction between the PDDA-QDs and the underlying Si_3N_4 crystal as well as interaction between free PDDA polymer and the bilayers. For polymer control experiments we used a poly(diallyldimethylammonium chloride) solution in water (Sigma, average M_w of 200,000-350,000, 1% wt). Determination of free ligand in solution is difficult and likely the concentration used in this study was an overestimate of unbound free ligand. However, it represents the absolute maximum amount of free ligand as it was the starting

concentration used to functionalize the quantum dots. All attachment experiments were conducted in at least triplicate at 25.0 ± 0.5 °C.

3.2.5 Atomic force microscopy (AFM) imaging

To obtain an image of what the bilayers looked like before and after exposure to PDDA-QDs we used atomic force microscopy (AFM). Prior to AFM, mica substrates (Highest Grade V1, Ted Pella) were adhered to glass bottom dishes (P60G-1.5-30-F, MatTek Corporation) using 5 minute epoxy (ITW Polymer Adhesives). Prior to use, we cleaved the mica using double-sided tape to produce a clean, atomically flat surface.[34] We equilibrated the mica in 0.150 M NaCl and 0.005 M $CaCl_2$ buffered to pH 7.4 with 0.010 M HEPES for at least 20 min. Vesicles (0.0625 $mg \cdot mL^{-1}$) in the same buffer conditions were added to the dish to cover the mica surface and heated to 45 °C, a temperature above the transition temperature of all lipids used here and shown previously to work for these systems,[35] for 1 hr . The sample was allowed to cool to room temperature and the volume was exchanged with 12 mL (3 aliquots of 4 mL each) of vesicle-free solution to remove any loosely adhered vesicles. The calcium was removed from solution by exchanging the solution with 12 mL of 0.150 M NaCl solution. Finally, the ionic strength of the solution was adjusted to 0.010 M NaCl by exchanging with 12 mL of 0.010 M NaCl solution prior to exposure to quantum dots. These sample represent the "before PDDA-QDs" images.

All images were collected in PeakForce Tapping™ mode using a Dimension Icon (Bruker) instrument. Gold-coated silicon nitride probes (Bruker, NPG) with a nominal force constant of 0.24 N/m were used to minimize electrostatic interactions with the positively-charged PDDA-QDs. Prior to imaging, the deflection sensitivity of the cantilever in air was determined using a fused silica reference sample. The force constant was also calibrated in air using the thermal tune method and fitting the power spectral density plot to a Lorentzian function.[36] Imaging was conducted in

0.010 M NaCl buffered to pH 7.4 with 0.010 M HEPES. The deflection sensitivity of the tip in fluid was re-calibrated using the known force constant.[37-38]

Images were collected at room temperature (24.5 °C). The bilayers were screened for quality prior to introducing quantum dots to the bilayer. A "quality" bilayer contained no defects across at least three spots microns away from one another. An "x" was placed on the bottom of the glass bottom dish to ensure that same region could be found using the optical microscope on the AFM and that the same defect-free region was examined before and after exposure to nanomaterials. To minimize the effect of the substrate and interactions that can occur at defects sites,[9,18] bilayers not meeting this criteria were not used for subsequent exposure to quantum dots. At least three "before PDDA-QDs" images were collected for at least three different samples for each bilayer type studied.

To examine the time scale of induced structural changes, we conducted experiments where suspensions of 1 nM QDs in 0.010 M NaCl were added to the bilayers and imaging began immediately without the rinse stage. This sequence represents the "after PDDA-QDs" images. We collected images of the same spot for up to 1 hour and then went to various other spots on the bilayer. Again, at least three "after" images were collected at various spots microns away from one another. We also conducted experiments to best match the sequence used for QCM-D/NPS studies, where suspensions of 1 nM QDs in 0.010 M NaCl were added to the supported lipid bilayer and allowed to interact for 20 min. After 20 min, bilayers were rinsed with nanoparticle-free solution to remove any loosely adhered QDs and imaging was immediately conducted at various spots on the bilayers. Control experiments were conducted to characterize the particles interacting with the underlying mica as well as any free polymer ligand (PDDA) interacting with either the bilayers or the underlying mica. Control experiments were also conducted where we added just buffer instead

of PDDA-QDs and immediately began imaging to ensure that no changes in bilayer structure were observed due to sample preparation or changes over time.

3.3 Results and Discussion

3.3.1 PDDA-QDs attachment to zwitterionic bilayers as probed by QCM-D and LSPR

To investigate the interactions between the PDDA-QDs and the SLBs, we used quartz crystal microbalance with dissipation monitoring to investigate the attachment of particles to the bilayers as well as any changes in viscoelastic properties. We chose to use the zwitterionic bilayer, DOPC, to investigate the role of electrostatics in these interactions. The supported zwitterionic DOPC bilayer carries a negative potential,[7,39] while the PDDA-QDs have a ζ-potential of +33 ± 4 mV (Table 3.1). Consistent with electrostatic attraction, we observed favorable interaction between the positively charged quantum dots and the negatively charged bilayer. Figure 3.1a shows the frequency change as a function of time as quantum dots interacted with a DOPC bilayer. A maximum change of -14.6 ± 1.9 Hz (268.2 ± 34.2 $ng \cdot cm^{-2} \cdot s^{-1}$) was observed. Figure 3.1b shows the corresponding dissipation shift associated with this attachment. The maximum change in dissipation before rinse was $1.4 \pm 0.2 \times 10^{-6}$. Upon rinse, a small increase in frequency (2.2 ± 0.3 Hz) and drop in dissipation ($-0.5 \pm 0.1 \times 10^{-6}$) was observed, corresponding to a loss of mass and a less viscoelastic surface. This was likely loosely adsorbed quantum dots rinsing away. Interestingly, approximately 30 minutes after attachment began and 10 minutes after the rinse began, a sharp decrease in frequency with a corresponding increase in dissipation was observed. This resulted in an increase in dissipation ($0.8 \pm 0.2 \times 10^{-6}$) and a loss of mass of 4.5 ± 0.5 Hz (81.3 ± 8.9 $ng \cdot cm^{-2} \cdot s^{-1}$) as compared to the point of maximum attachment prior to rinse. Our initial hypothesis was that this observation was due to structural changes to the SLB. A previous report in the literature using QCM-D to study the formation of negatively charged SLBs, also observed

an increase in frequency followed by an apparent mass gain with an accompanied decrease in dissipation followed by a sharp rise in dissipation.[32] The authors attributed these observations to a change in conformation or restructuration of the bilayer at the silica surface.[32] While this study does not involve nanomaterials and our ending structures are likely different, the similarities in the trends of the frequency and dissipation traces suggest restructuring of the DOPC upon interaction with PDDA-QDs is likely occurring. The final values of *f* and *D* indicated that the restructured bilayer is flexible and likely has adsorbed quantum dots. However, the hydrodynamic mass measured by QCM-D can sometimes be deceptive in understanding the actual amount of attachment occurring at the bilayer surface due to the coupled water inherently measured.

In an attempt to better understand the restructured bilayer, we used NPS to measure changes in the index of refraction at the surface of the bilayer, which can be related to the optical mass of an adsorbed analyte. Nanoplasmonic sensing qualitatively showed comparable interaction between the PDDA-QDs and the DOPC bilayer to that observed by QCM-D. Figure 3.1c shows the wavelength of maximum extinction (λ_{max}) shifted to a longer wavelength as PDDA-QDs interacted with the bilayer. An increase in the λ_{max} can be interpreted as an increase in optical mass. Unlike with QCM-D the optical mass does not include contributions from the hydrodynamically coupled water and therefore can be considered a "dry mass." We observed that the optical mass increased as QDs interacted with the bilayer and continued to rise upon rinse. The maximum observed $\Delta\lambda_{max}$ value was 0.8 ± 0.1 nm. Immediately upon rinse, we observed a continued increase in $\Delta\lambda_{max}$, suggesting an increase in mass. This is the opposite that was shown for QCM-D, where we observed an apparent mass loss upon rinse. We hypothesize this may be due to the different sensing depths of the two techniques. QCM-D has a sensing depth on the order of 100 nm, whereas NPS is much more surface-sensitive and probes ~10 nm into solution.[40] This observed difference

may be attributable to structural rearrangements or nanoparticle attachment at the bilayer/sensor surface, while loosely bound QDs are rinsed away. By QCM-D we measure the interactions occurring at the surface, but also in solution so an overall net decrease in mass may be observed despite the net gain observed by NPS at the surface. Following rinse, a drastic drop $\Delta\lambda_{max}$ was observed followed by equilibration of the $\Delta\lambda_{max.}$ This corresponded to the same point where there is an apparent mass gain and an increase in dissipation by QCM-D. Again, this is likely due to structural rearrangement. Comparing the λ_{max} value of the final rinsed bilayer after exposure to PDDA-QDs with the pristine bilayer shows a positive $\Delta\lambda_{max}$ value of 0.09 ± 0.02 nm, confirming the presence of adsorbed quantum dots. Taking this information with the dissipation data, we hypothesize that the remaining surface is more dissipative than the starting bilayer and has more mass associated with it, which means it could be a combination of intact bilayer, quantum dots, multilayers, and/or holes. While we can only hypothesize what the remaining structure looks like by QCM-D and NPS, AFM allowed us to probe the structural impact of the quantum dots on the bilayer.

3.3.2 PDDA-QDs induce structural changes to zwitterionic bilayers

To understand the QCM-D and NPS traces, we used AFM to gain insights into any structural changes that occurred due to the interaction of PDDA-QDs with the DOPC bilayer. We first examined any structural changes that occurred immediately upon introduction of PDDA-QDs. Figure 3.2 shows a time lapse sequence of PDDA-QDs interacting with a DOPC bilayer. Figure 3.2a shows a pristine DOPC bilayer with no defects present. A bilayer of DOPC is composed of an entirely liquid-disordered phase with no distinguishing features, causing the topography to mimic that of the underlying surface.[41] To ensure the presence of a DOPC bilayer we conducted

F_b curves and found a characteristic rupture event.[42] After this confirmation we added quantum dots and immediately began imaging.

Figure 3.2b shows that immediately upon interaction with the bilayer, the QDs caused structural changes. Initially upon adsorption, we observed features 1.1 ± 0.2 nm in height as well as taller features with heights of 8.6 ± 2.3 nm (Figure 3.3a). The taller features appeared solely within the microdomains that formed. Previous work showed high regions (~10 nm) formed within microdomains (~1.4 nm in height) after amphiphilic peptide interaction with a DOPC bilayer.[43] The authors hypothesized that the tallest features were either large aggregates of peptides or partially solubilized/"budding" regions of the bilayer.[43] To begin to understand our observed features, we examined the height of the quantum dots on the mica surface. Figure 3.3b shows that when adsorbed to mica the quantum dots have an average size of 4.4 ± 3.2 nm. These values are consistent with the values found for the core size of the particles by TEM (Figure A3.1, Table 3.1) and the nominal size of the particles as given by the company (core size 3.3 nm, shell thickness 2.5 nm, and PDDA thickness 2 nm; ~7.8 nm). A control experiment looking at the interaction of 1 wt% PDDA polymer with no QDs (Figure 3.3c), showed, to a lesser extent than the case of PDDA-QDs, the formation of ~1 nm tall microdomains, but no taller features. Furthermore, when we added just buffer to the DOPC bilayer and imaged it over time, we observed no structural changes to the membrane, indicating that this is a polymer/PDDA-QD specific effect and not due to the experimental protocol or changes to the bilayer over time (Figure A3.2a, b). Given that no taller features were observed with polymer alone, we conclude that the brightest dots observed in the images are the PDDA-QDs; however, we cannot rule out the idea that the PDDA-QDs cause partial solubilization of the membrane, whereas the polymer itself does not.

We hypothesize that the formation of microdomains are likely caused by the PDDA polymer on the surface of the quantum dots due to the fact that we observed these structures with both PDDA-QDs and solely PDDA polymer. However, the increased size of the PDDA-QDs as compared to the polymer alone appears to increase the impact of these structural changes. The initial attachment likely occurs due to favorable electrostatic attraction between the positively charged quaternary amine in the PDDA and the negatively charged phosphate groups in the phosphocholine headgroups of the zwitterionic bilayer, which has been observed previously with primary amines.[7,44] Following this initial attachment, the hydrophobic backbone of the polymer may extend through the hydrophobic tail groups of the bilayer and cause an increase in observed height. The observed height change (1.1 ± 0.2 nm) is also consistent with the quantum dots inducing an increase in lipid ordering within the membrane.[45] However, an increase in lipid ordering and packing would lead to a decrease in bilayer coverage or hole formation,[43] which was not observed. Over time more of the same features were observed, which is consistent with more particles penetrating into the bilayer over time. This also is consistent with the increase in peak shift observed by NPS upon rinse. More quantum dots may be penetrating the bilayer over time causing an increase in mass at the surface and an increase in the microdomains observed by AFM.

3.3.3 Interaction of PDDA-QDs with phase-segregated domain containing SLBs

We also wanted to explore the role that phase-segregated domains play in the structural rearrangement of the membranes following interaction with the PDDA-QDs. Liquid-ordered domains play an important role in cell signaling and trafficking[46] in eukaryotic cells. We have previously shown that the presence of liquid-ordered domains, comprised of sphingomyelin and cholesterol, increased attachment with positively charged gold nanoparticles.[6] The importance of

these biomolecules in addition to the previous observations warrant investigation into how the PDDA-QDs impacted this type of SLB.

We conducted QCM-D, NPS, and AFM imaging with 60/20/20 mol% DOPC/SM/Chol bilayers in a similar manner as the experiments with DOPC explained above. In the case of the phase-segregated domain containing SLBs, a maximum Δf change of -13.1 ± 1.4 Hz and ΔD of 1.1 ± 0.1 × 10^{-6} were observed. These values were not statistically different from the values observed for PDDA-QD interaction with DOPC (p = 0.329 and p = 0.101, respectively). We hypothesize that we did not see an increase in attachment like previously reported for positively charged gold nanoparticles,[6] due to the bulky structure of the polymer coating used on the quantum dots as compared to the short chain amine used in the previous study. The steric hindrance induced by this bulky polymer may prevent attraction between the amine group on the ligand and the exposed negative charge at the edge of the domain boundary.[6]

Upon rinse, a small increase in frequency (1.6 ± 0.3 Hz) and decrease in dissipation (-0.4 ± 0.1 × 10^{-6}) was observed, followed closely by a sharp increase in dissipation and drop in frequency until an equilibrium was reached, again similar to that observed for pure DOPC. This resulted in an increase in dissipation (1.4 ± 0.2 × 10^{-6}) and a mass loss of 2.3 ± 0.1 Hz (41.7 ± 1.9 ng·cm^{-2}·s^{-1}) as compared to the point of maximum attachment prior to rinse. Comparing these final values to DOPC, the phase-segregated domain bilayers had a lower mass loss as compared to the maximum amount of attachment (p < 0.05) and a more dissipative structure as compared to the maximum dissipation change following the rinse step (p < 0.05). Again, these traces suggested that the PDDA-QDs caused structural rearrangement to the membrane.

To elucidate any structural differences caused by PDDA-QDs interacting with phase-segregated domain containing SLBs, we used *in situ* AFM imaging to examine the bilayers

immediately and 20 min after interaction with the quantum dots. Figure 3.4 shows the time lapse of PDDA-QDs interacting with a phase-segregated domain containing bilayer. Initially, domains containing sphingomyelin and cholesterol are observed to be ~1 nm higher in height than the underlying liquid-disordered (L_d), DOPC, component of the bilayer (Figure 3.4a, 3.5a). This finding is consistent with previous work suggesting that cholesterol induces ordering of the unsaturated acyl tails of sphingomyelin, which makes these L_o regions ~1 nm taller than the L_d regions.[6,45] Immediately upon addition of the QDs, we observed similar structural changes as observed with pure DOPC bilayers. Figure 3.4b shows the formation of microdomains with taller features present inside of them, consistent with what was observed with DOPC. However, we also found that the restructured lipids around the quantum dots were slightly taller (1.8 ± 0.2 nm, $p < 0.001$) than the structures in the DOPC bilayer (Figure 3.5b). This is consistent with the hypothesis that the positive amine group binds to the phosphocholine headgroup and the hydrophobic tails induce a height change of the surrounding bilayer. The presence of 30% cholesterol in a DPPC bilayer was shown to increase its height by ~0.6 nm.[47] Therefore, the presence of cholesterol in the membranes used in our work, may account for the increase in height of the microdomains as compared to pure DOPC.

As time continued, the liquid-ordered domains began to shrink in size and ultimately disappear within 15 min of addition of the QDs (between Figure 3.5d and Figure 3.5e). Control experiments scanning the domain over the same length of time without exposure to PDDA-QDs showed no formation of microdomains or bright regions over the length scales of these studies (Figure A3.2c,d). Figure A3.3 shows the time lapse of interaction of free PDDA polymer (average molecular weight 200,000 – 350,000 M_w, 1 wt%) with 60/20/20 mol% DOPC/SM/Chol. This interaction also resulted in the disappearance of domain structures, but to a lesser extent than when

QDs were present (domains still remained after 30 min of interaction). We hypothesize that the disappearance of the domain structure, may be due to the preferential removal of cholesterol from the domains, which would cause a collapse of the domains into a liquid-disordered phase. Previous work, using molecular dynamics simulations to study the interaction between amphiphilic, anionic nanoparticles and a dipalmitoylphosphatidlcholine bilayer with various amounts of cholesterol present showed that the charged group on the nanoparticle associated with the headgroups of the lipids while the hydrophobic ligands remain buried in the core.[48] The embedding of the nanoparticle into the bilayer forced the cholesterol to restructure; namely, the concentration of the cholesterol near nanoparticles decreased and the overall structure of the bilayer becomes more disordered.[48] Our proposed mechanism and observed disappearance of the domain structures supports these simulations.

3.3.4 Additional structural changes observed

We also conducted experiments where we allowed the PDDA-QDs to interact with the bilayers for 20 minutes, rinsed the bilayer, and then immediately imaged different spots on the membrane. These images may be more representative of the final stages of the bilayer as probed by QCM-D. The formation of microdomains with taller features in the center of the microdomain were the most commonly observed feature for both DOPC and 60/20/20 mol% DOPC/SM/Chol. However, Figure 3.6 also shows another commonly observed feature – the formation of large islands of lipids, ~7 nm above the underlying bilayer, which may suggest the formation of a multilayer of lipids on top of the underlying bilayer. The visualization of the underlying topography is consistent with the idea that these patches are sitting on top of the underlying surface and likely give rise to the large dissipation changes we observed by QCM-D. This type of bilayer island formation has been observed previously for an amphiphilic peptide dendrimer interacting

with a gel-phase membrane composed of 1,2-dipalmitoyl-*sn*-glycero-3-phosphocholine (DPPC).[14] We observed these island structures for both 60-20-20 DOPC/SM/Chol bilayers and for pure DOPC bilayers before and after rinsing with QD-free buffer (Figure 3.6). This suggests that the structural rearrangements likely occur due to interaction with the PDDA-QDs and are not solely dependent on a rinse stage as may be interpreted by the QCM-D data.

3.4 Conclusions

We have demonstrated that PDDA-QDs induce a complex structural rearrangement of supported lipid bilayers consisting of 100% DOPC or 60/20/20 mol% DOPC/SM/Chol. The use of three complementary, *in situ* analytical methods provided unprecedented insights into these structural changes. Namely, QCM-D coupled with NPS gave insights into attachment of QDs followed by large dissipative changes, which suggested attachment of the QDs to and structural rearrangement of the SLBs. Real-time *in situ* AFM imaging provided a visual interpretation of these mass and viscoelastic changes. We observed the formation of microdomains with higher features in the center of the microdomains that we hypothesize to be quantum dots. Previous work examining amphiphilic peptide interaction with a DOPC bilayer showed similar microdomain formation, with a corresponding taller region in the center, which was attributed to either peptide aggregates or solubilization of the membrane.[43] We also observed multilayer structures, which helped to explain the increased dissipation shifts observed by QCM-D. The PDDA-QDs also demonstrated preferential interaction with the liquid-ordered phase of the 60/20/20 mol% DOPC/SM/Chol membranes. The liquid-ordered phase was no longer visible after ~15 min of interaction with the QDs suggesting that the ordering of the lipids was disturbed by the QDs. Our results highlight the importance of using complementary analytical tools to study complex interactions at the nano-bio interface.

Given the relevance of lipid rafts to cell signaling and trafficking in eukaryotic cells,[46] our findings highlight the importance of studying these important membrane organizing structures. The disappearance of these biomolecules could result in detrimental effects on organisms. Liquid-ordered domains are hypothesized to exist naturally within animal,[49] plant,[50] fungal,[51] and bacterial[52] cell membranes; however, they are difficult to characterize due to their small size (10-200 nm)[53] and dynamic nature.[53-54] The incorporation of phase-segregated domains into model SLBs enables the use surface sensitive, *in situ* characterization techniques to study these systems. Working in real time enhances our understanding of the dynamics of these systems. In particular, in this study were able to observe the disappearance of the liquid-ordered phase within 15 min of interaction with nanomaterials.

In the experiments described here, we focused on the interactions of PDDA-QDs with defect-free SLBs. The analytical tools of interest all required a negatively charged substrate in order to form a SLB. From QCM-D and AFM control experiments we found a strong electrostatic attraction between the underlying substrate and the positively charged QDs. While differences were observed in comparing the interactions with and without a membrane present (e.g., increases in dissipation shifts, rearrangement of the bilayer structure), the negative charge of the substrate may play a role in interactions with positively charged materials. Previous studies examining the impacts of nanomaterials,[9] dendrimers,[14] or peptides[43] with SLBs have started with defect-ridden SLBs and examined the impacts to these structures. The defects provide a means to confirm bilayer presence and measure the height of the starting membrane; however, these defect-sites may cause artificial interaction due to the underlying substrate.[55] While we cannot claim that the entire bilayer surface used in our studies was defect-free we focused on imaging samples that did not have defects across many spots analyzed. We also imaged the same defect-free area before and after

interaction with nanomaterials to minimize any convoluted effects due to the underlying substrate. While these studies present a good first approach to understanding interactions at the cellular membrane, it may be advantageous to study changes in membrane structure due to QDs using suspended lipid bilayers in future work.

Overall, we propose that the forces that drive the interactions between PDDA-QDs and SLBs (both DOPC and 60/20/20 mol% DOPC/SM/Chol) are a combination of electrostatic and hydrophobic. The positive charge on the quaternary amine interacts favorable with the negatively charged phosphate group.[7,44] Following this initial "anchoring," the hydrophobic backbone of the polymer ligand can insert into the hydrophobic acyl chains of the lipid bilayer and cause restructuring around this site of contact. The QDs may then penetrate through the membrane or remain on top of the surface. Previous molecular dynamics studies have shown that hydrophobic ligands can anchor within the membrane.[48,56] The present study represents an initial demonstration of the complex interactions that can occur between quantum dots wrapped with one particular polymer. While more studies are necessary to generalize these results, other studies with amphiphilic and positively charged, hydrophobic ligands have shown similar features[43] and similar mechanisms of interaction were proposed.[56] Thus, we expect the results presented here will be most transferable to nanomaterials with positively charged hydrophobic or amphiphilic ligands.

3.5 Tables

Table 3.1. Hydrodynamic diameter (d_h), zeta potential (ζ), and particle diameter determined by TEM for the PDDA-QDs used in this study.

Solution Conditions	d_h (nm)	ζ (mV)	Diameter by TEM (nm)
0.01 M HEPES, 0.01 M NaCl, pH 7.4	17 ± 1	33 ± 4	6.2 ± 1.2

[a]TEM analysis is the average and standard deviation of 25 particles. Hydrodynamic and zeta potential measurements were made in 0.01 M HEPES, 0.01 M NaCl, pH 7.4 and are the average and standard deviation of 5 measurements. TEM samples were dried prior to analysis.

Table 3.2. Summary of frequency shifts, dissipation changes, shifts in λ_{max}, and initial attachment rates upon interaction between PDDA-QDs and the indicated supported lipid bilayer or silicon nitride surface as measured by nanoplasmonic sensing and quartz crystal microbalance with dissipation monitoring.[a]

Bilayer Type	**$\Delta f_7/7$ (Hz) (20 min)**	**$\Delta D_7/7$ (Hz) (20 min)**	**$\Delta\lambda$ (nm) (maximum)**	**$\Delta f_7/7$ (Hz) (Final)**	**$\Delta D_7/7$ (Hz) (Final)**	**$\Delta\lambda$ (nm) (Final)**	**initial attachment rate, r_d (ng·cm^{-2}·s^{-1})**
DOPC	-14.6 ± 1.9	1.4 ± 0.2	0.8 ± 0.1	-10.0 ± 1.9	2.2 ± 0.4	0.09 ± 0.02	0.7 ± 0.2
DOPC/SM/Chol	-13.1 ± 1.4	1.1 ± 0.1	0.6 ± 0.1	–10.9 ± 1.4	2.6 ± 0.3	0.08 ± 0.03	0.4 ± 0.1
Si_3N_4	-15.5 ± 0.7	0.6 ± 0.05	0.6 ± 0.02	-15.4 ± 0.7	0.6 ±0.05	0.6 ± 0.04	0.2 ± 0.1

[a] Attachment experiments were conducted in 0.025 M NaCl buffered to pH 7.4 with 0.002 M HEPES at 25 °C. All data are for the 7th harmonic. Data for the frequency and dissipation shifts are after 20 min of attachment. Data for the $\Delta\lambda_{max}$ is for the maximum shift in wavelength observed referenced to the pristine bilayer. Values are means ± standard deviations of at least triplicate experiments. Abbreviations: DOPC, 1,2-dioleoyl-*sn*-glycero-3-phosphocholine; SM, sphingomyelin; Chol, cholesterol.

Table 3.3. Line scan analysis of features observed by AFM.[a]

Bilayer Type	Particle Height (nm)	Microdomain Height (nm)	Particle Height within Microdomains (referenced to underlying bilayer) (nm)
Mica	4.4 ± 3.2 (N = 117)	N/A	N/A
DOPC	N/A	1.1 ± 0.2 (N = 26)	8.6 ± 2.3 (N = 31)
DOPC/SM/Chol	N/A	1.8 ± 0.2 (N = 25)	7.7 ± 2.6 (N = 31)

[a] AFM experiments were conducted in 0.010 M NaCl buffered to pH 7.4 with 0.010 M HEPES at 24.5 °C. Abbreviations: DOPC, 1,2-dioleoyl-*sn*-glycero-3-phosphocholine; SM, sphingomyelin; Chol, cholesterol.

3.6 Figures

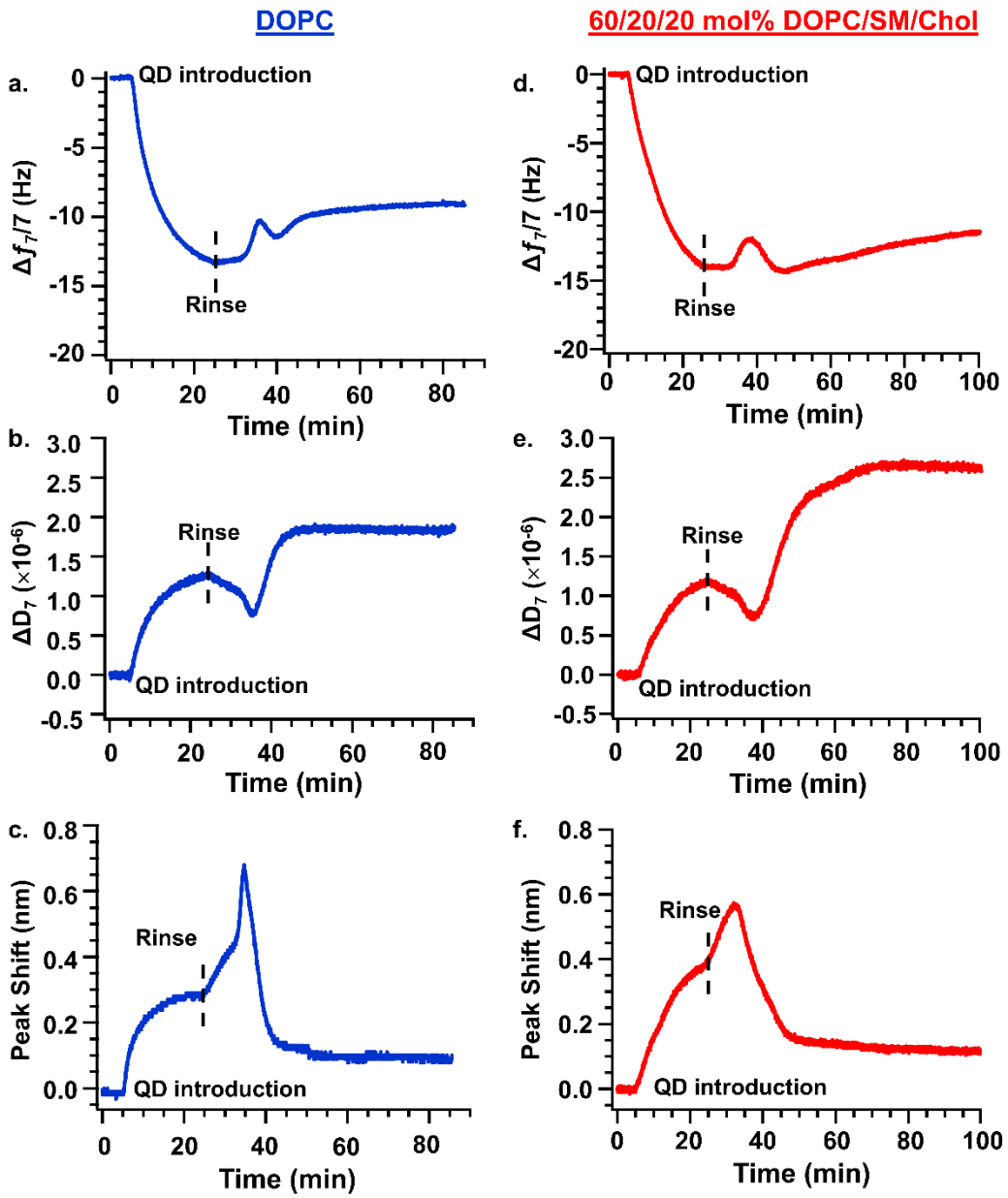

Figure 3.1. Representative changes in frequency and dissipation upon introduction of 1 nM PDDA- QDs to a DOPC bilayer in 0.01 M NaCl buffered to pH 7.4 with 0.01 M HEPES. The bilayer has already been formed and interaction between the QDs and the bilayer begins where noted. The dashed line represents the point where buffer without QDs reach the sensor surface and some mass loss, decrease in dissipation, and increase in $\Delta\lambda_{max}$ is observed.

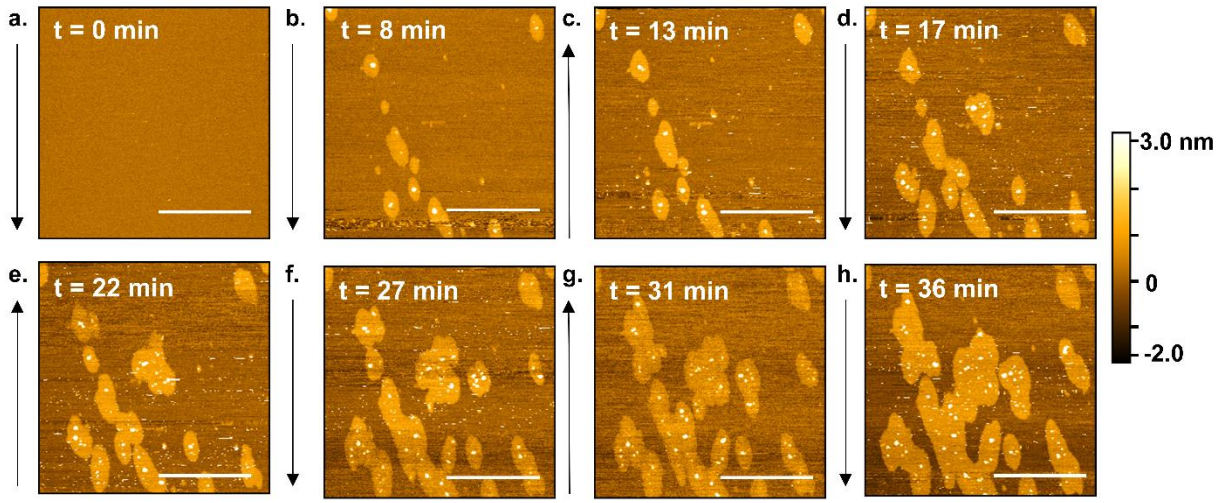

Figure 3.2. Time-lapse topographical AFM images showing the impact of PDDA-QDs on a DOPC bilayer immediately after injection of particles. (a) DOPC bilayer prior to the introduction of PDDA-QDs, (b-h) subsequent images taken after interaction with the PDDA-QDs. All images were collected in 0.01 M NaCl buffered to pH 7.4 with 0.01 M HEPES at 24.5 °C. Black arrows represent the scan direction for the given image. Scale bars on all images are 2 µm. Z-height color scale corresponds to all images. The time on each image indicates how much time the bilayer had been in contact with PDDA-QDs. Each image took between 4-6 mins to capture depending on optimization of scan parameters.

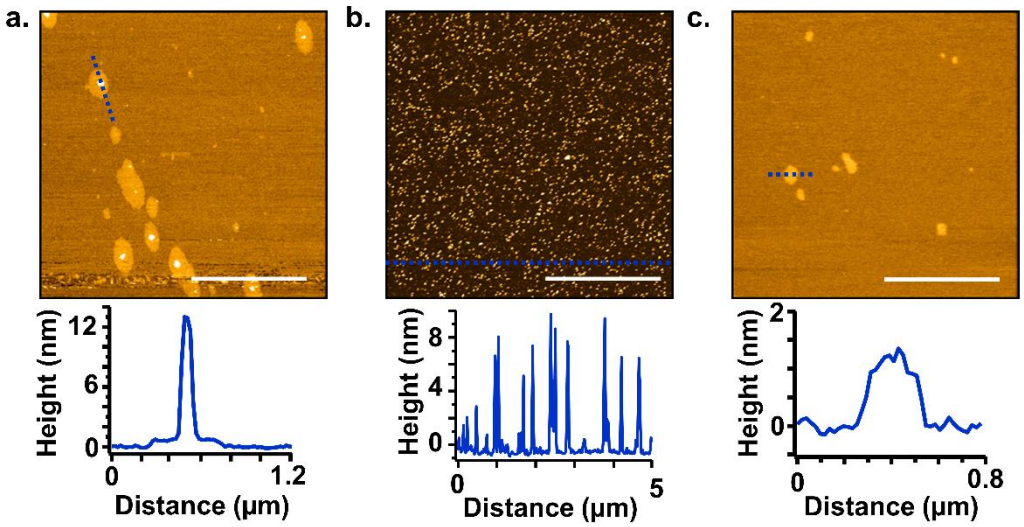

Figure 3.3. (a) Line profile across the microdomains observed after interaction of PDDA-QDs with the DOPC bilayer from Figure 3.2a (b) PDDA-QDs on a mica substrate and corresponding line scan, (c) 1 wt% PDDA polymer (average M_w 200,000-350,000 Da, 1 wt%) interaction with a DOPC bilayer with corresponding line scan. All images were collected in 0.01 M NaCl buffered to pH 7.4 with 0.01 M HEPES at 24.5 °C. Line scans were taken across the dashed blue line in each image. Scale bars on all images are 2 μm.

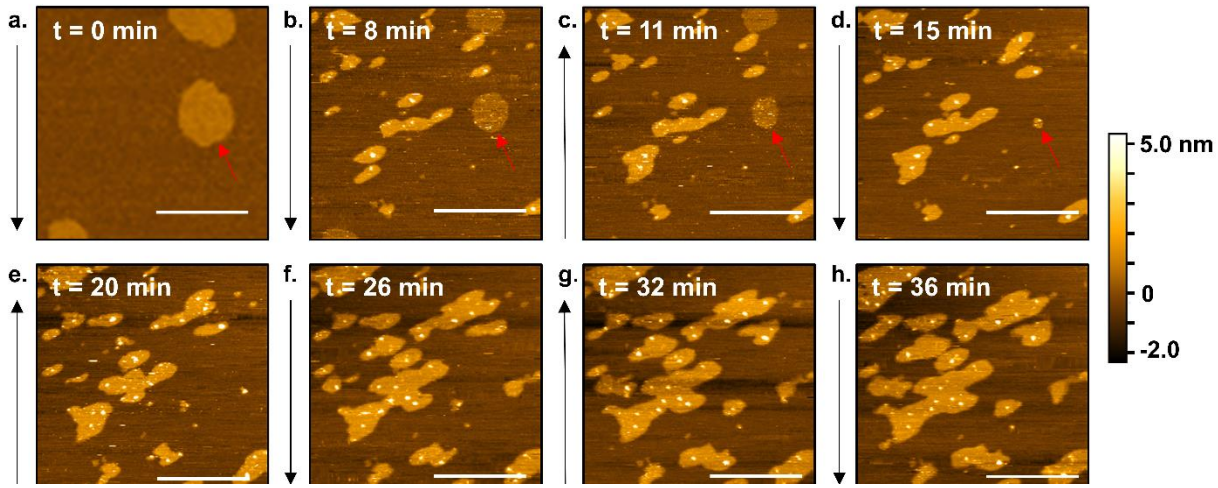

Figure 3.4. Time-lapse topographical AFM images showing the effect of PDDA-QDs on a bilayer initially containing liquid-ordered (L_o) and liquid-disordered (L_d) domains. Bilayer composition was 60/20/20 mol% DOPC/SM/Chol. (a) Bilayer prior to the introduction of PDDA-QDs, (b-h) subsequent images taken after interaction with the PDDA-QDs. All images were collected in 0.01 M NaCl buffered to pH 7.4 with 0.01 M HEPES at 24.5 °C. Black arrows represent the scan direction for the given image. Scale bars on all images are 2 µm. The red arrow is intended to direct the reader's eye to the disappearance of the liquid-ordered domains. Z-height color scale corresponds to all images. The time on each image indicates how much time the bilayer had been in contact with PDDA-QDs. Each image took between 3-6 mins to capture depending on optimization of scan parameters.

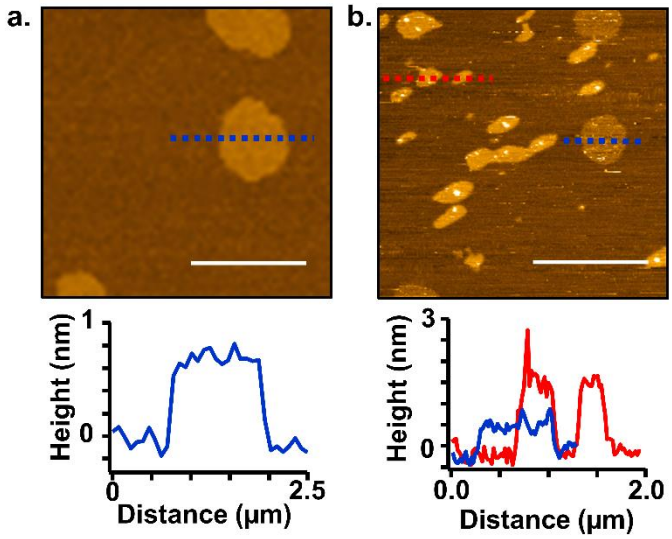

Figure 3.5. Representative line traces observed for height across features observed in a 60/20/20 mol% DOPC/SM/Chol bilayer (note: same bilayer as presented in Figure 3.4) (a) prior to and (b) after interaction with 1 nM PDDA-QDs. The blue trace traces in both images show the height over a liquid-ordered domain, whereas the red trace in (b) shows the height across the microdomain structure induced by the PDDA-QDs. All images were collected in 0.01 M NaCl buffered to pH 7.4 with 0.01 M HEPES at 24.5 °C. Scale bars are 2 μm.

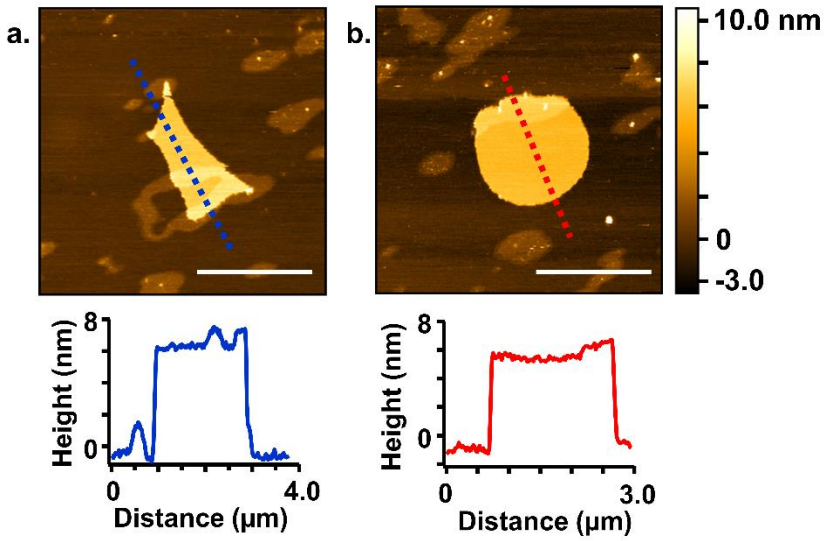

Figure 3.6. AFM images and corresponding line scan of multilayers formed (a) before and (b) after rinse of different spots on the same 60/20/20 mol% DOPC/SM/Chol bilayer presented in Figure 3.4. All images were collected in 0.01 M NaCl buffered to pH 7.4 with 0.01 M HEPES at 24.5 °C. Scale bars are 2 μm.

3.7 References

1. Hamers, R. J. Nanomaterials and global sustainability. *Acc. Chem. Res.*, **2017,** *50,* 633-637.

2. Louie, S. M.; Dale, A. L.; Casman, E. A.; Lowry, G. V., Challenges facing the environmental nanotechnology research enterprise. In *Engineered nanoparticles and the environment: Biophysicochemical processes and toxicity*, Xing, B.; Vectis, C. D.; Senesi, N., Eds. 2016; Vol. 4, pp 3-19.

3. Lesniak, A.; Salvati, A.; Santos-Martinez, M. J.; Radomski, M. W.; Dawson, K. A.; Aberg, C. Nanoparticle adhesion to the cell membrane and its effect on nanoparticle uptake efficiency. *J. Am. Chem. Soc.*, **2013,** *135,* 1438-1444.

4. Goodman, C. M.; McCusker, C. D.; Yilmaz, T.; Rotello, V. M. Toxicity of gold nanoparticles functionalized with cationic and anionic side chains. *Bioconjugate Chem.*, **2004,** *15,* 897-900.

5. Yuan, H.; Li, J.; Bao, G.; Zhang, S. Variable nanoparticle-cell adhesion strength regulates cellular uptake. *Phys. Rev. Lett.*, **2010,** *105,* 138101.

6. Melby, E. S.; Mensch, A. C.; Lohse, S. E.; Hu, D.; Orr, G.; Murphy, C. J.; Hamers, R. J.; Pedersen, J. A. Formation of supported lipid bilayers containing phase-segregated domains and their interaction with gold nanoparticles. *Environ. Sci.: Nano*, **2016,** *3,* 45-55.

7. Troiano, J. M.; Olenick, L. L.; Kuech, T. R.; Melby, E. S.; Hu, D.; Lohse, S. E.; Mensch, A. C.; Dogangun, M.; Vartanian, A. M.; Torelli, M. D.; Ehimiaghe, E.; Walter, S. R.; Fu, L.; Anderton, C. R.; Zhu, Z.; Wang, H.; Orr, G.; Murphy, C. J.; Hamers, R. J.; Pedersen, J. A.; Geiger, F. M. Direct probes of 4 nm diameter gold nanoparticles interacting with supported lipid bilayers. *J. Phys. Chem. C*, **2015,** *119,* 534-546.

8. Chen, K. L.; Bothun, G. D. Nanoparticles meet cell membranes: Probing nonspecific interactions using model membranes. *Environ. Sci. Technol.*, **2014,** *48,* 873-880.

9. Leroueil, P. R.; Berry, S. A.; Duthie, K.; Han, G.; Rotello, V. M.; McNerny, D. Q.; Jr., J. R. B.; Orr, B. G.; Holl, M. M. B. Wide varieties of cationic nanoparticles induce defects in supported lipid bilayers. *Nano Letters*, **2008,** *8,* 420-424.

10. Chen, J.; Hessler, J. A.; Putchakayala, K.; Panama, B. K.; Khan, D. P.; Hong, S.; Mullen, D. G.; DiMaggio, S. C.; Som, A.; Tew, G. N.; Lopatin, A. N.; James R. Baker, J.; Holl, M. M. B.; Orr, B. G. Cationic nanoparticles induce nanoscale disruption in living cell plasma membranes. *J. Phys. Chem. B*, **2009,** *113,* 11179-11185.

11. Lin, J. Q.; Zheng, Y. G.; Zhang, H. W.; Chen, Z. A simulation study on nanoscale holes generated by gold nanoparticles on negative lipid bilayers. *Langmuir*, **2011,** *27,* 8323-8332.

12. Yousefi, N.; Wargenau, A.; Tufenkji, N. Toward more free-floating model cell membranes: Method development and application to their interaction with nanoparticles. *ACS Appl. Mater. Interfaces,* **2016,** *8,* 14339-14348.

13. Nabika, H.; Sakamoto, A.; Motegi, T.; Tero, R.; Yamaguchi, D.; Unoura, K. Imaging characterization of cluster induced morphological changes of a model cell membrane. *J. Phys. Chem. C,* **2016,** *120,* 15640-15647.

14. Lind, T. K.; Zielinska, P.; Wacklin, H. P.; Urbanczyk-Lipkowska, Z.; Cardenas, M. Continuous flow atomic force microscopy imaging reveals fluidity and time-dependent interactions of antimicrobial dendrimer with model lipid membranes. *ACS Nano,* **2014,** *8,* 396-408.

15. Ge, Y.; Horst, A. M.; Kim, J.; Priester, J. H.; Welch, Z. S.; Holden, P. A., Toxicity of manufactured nanomaterials to microorganisms. In *Engineered nanoparticles and the environment: Biophysicochemical processes and toxicity*, Xing, B.; Vectis, C. D.; Senesi, N., Eds. 2016; pp 320-346.

16. Ding, B.; Tian, Y.; Pan, Y.; Shan, Y.; Cai, M.; Xu, H.; Sun, Y.; Wang, H. Recording the dynamic endocytosis of single gold nanoparticles by AFM-based force tracing. *Nanoscale,* **2015,** *7,* 7545-7549.

17. Mecke, A.; Lee, D.-K.; Ramamoorthy, A.; Orr, B. G.; Holl, M. M. B. Synthetic and natural polycationic polymer nanoparticles interact selectively with fluid-phase domains of DMPC lipid bilayers. *Langmuir,* **2005,** *21,* 8588-8590.

18. Hong, S.; Bielinska, A. U.; Mecke, A.; Keszler, B.; Beals, J. L.; Shi, X.; Balogh, L.; Orr, B. G.; James R. Baker, J.; Holl, M. M. B. Interaction of poly(amidoamine) dendrimers with supported lipid bilayers and cells: Hole formation and the relation to transport. *Bioconjugate Chem.,* **2004,** *15,* 774-782.

19. Ruhle, S.; Shalom, M.; Zaban, A. Quantum-dot-sensitized solar cells. *ChemPhysChem,* **2010,** *11,* 2290-2304.

20. Martynenko, I. V.; Litvin, A. P.; Purcell-Milton, F.; Baranov, A. V.; Fedorov, A. V.; Gun'ko, Y. K. Application of semiconductor quantum dots in bioimaging and biosensing. *J. Mater. Chem. B,* **2017,** *5,* 6701-6727.

21. Medintz, I. L.; Uyeda, H. T.; Goldman, E. R.; Mattoussi, H. Quantum dot bioconjugates for imaging, labelling and sensing. *Nat. Mater.,* **2005,** *4,* 436-446.

22. Dabbousi, B. O.; Rodriguez-Viejo, J.; Mikulec, F. V.; Heine, J. R.; Mattoussi, H.; Ober, R.; Jensen, K. F.; Bawendi, M. G. (CdSe)ZnS core-shell quantum dots: Synthesis and characterization of a size series of highly luminescent nanocrystallites. *J. Phys. Chem. B,* **1997,** *101,* 9463-9475.

23. Biswas, N.; Bhattacharya, R.; Saha, A.; Jana, N. R.; Basu, J. K. Interplay of electrostatics and lipid packing determines the binding of charged polymer coated nanoparticles to model membranes. *Phys. Chem. Chem. Phys.,* **2015,** *17,* 24238-24247.

24. Zhang, X.; Yang, S. Nonspecific adsorption of charged quantum dots on supported zwitterionic lipid bilayers: Real-time monitoring by quartz crystal microbalance with dissipation. *Langmuir,* **2011,** *27,* 2528-2535.

25. Dubavik, A.; Sezgin, E.; Lesnyak, V.; Gaponik, N.; Schwille, P.; Eychmuller, A. Penetration of amphiphilic quantum dots through model and cellular plasma membranes. *ACS Nano,* **2012,** *6,* 2150-2156.

26. Moghadam, B. Y.; Hou, W. C.; Corredor, C.; Westerhoff, P.; Posner, J. D. Role of nanoparticle surface functionality in the disruption of model cell membranes. *Langmuir,* **2012,** *28,* 16318-16326.

27. Mensch, A. C.; Tapia Hernandez, R.; Kuether, J. E.; Torelli, M. D.; Feng, Z. V.; Hamers, R. J.; Pedersen, J. A. Natural organic matter concentration impacts the interaction of functionalized diamond nanoparticles with model and actual bacterial membranes. *Environ. Sci. Technol.,* **2017,** *51,* 11075-11084.

28. Malvern Instruments. *Intensity-volume-number: What size is correct*; Technical Note MRK1357-01.

29. Smoluchowski, M. V., Handbuchder Elektrizitat und des Magnetismus. In *Electrische Endosmose und Stromungsstrome*, Greatz, L., Ed. Barth: Leipzig, 1921; Vol. 2, pp 62-366.

30. Ohshima, H. Electrokinetics of soft particles. *Colloid. Polym. Sci.,* **2007,** *285,* 1411-1421.

31. Reviakine, I.; Johannsmann, D.; Richter, R. P. Hearing what you cannot see and visualizing what you hear: Interpreting quartz crystal microbalance data from solvated interfaces. *Anal. Chem.,* **2011,** *83,* 8838-8848.

32. Richter, R.; Mukhopadhyay, A.; Brisson, A. Pathways of lipid vesicle deposition on solid surfaces: A combined QCM-D and AFM study. *Biophys. J.,* **2003,** *85,* 3035-3047.

33. Keller, C. A.; Kasemo, B. Surface specific kinetics of lipid vesicle adsorption measured with a quartz crystal microbalance. *Biophys. J.,* **1998,** *75,* 1397-1402.

34. Mingeot-Leclercq, M. P.; Deleu, M.; Brasseur, R.; Dufrene, Y. F. Atomic force microscopy of supported lipid bilayers. *Nat. Protoc.,* **2008,** *3,* 1654-1659.

35. Sullan, R. M.; Li, J. K.; Hao, C.; Walker, G. C.; Zou, S. Cholesterol-dependent nanomechanical stability of phase-segregated multicomponent lipid bilayers. *Biophys. J.,* **2010,** *99,* 507-516.

36. Hutter, J. L.; Bechhoefer, J. Calibration of atomic-force microscope tips. *Rev. Sci. Instrum.,* **1993,** *64,* 1868-1873.

37. Ohler, B. *Practical advice on determination of cantilever spring constants*; Veeco: 2007.

38. Butt, H. J.; Jaschke, M. Calculation of thermal noise in atomic force microscopy. *Nanotechnology*, **1995,** *6*, 1-7.

39. Zimmermann, R.; Kuttner, D.; Renner, L.; Kaufmann, M.; Zitzmann, J.; Muller, M.; Werner, C. Charging and structure of zwitterionic supported bilayer lipid membranes studied by streaming current measurements, fluorescence microscopy, and attenuated total reflection Fourier transform infrared spectroscopy. *Biointerphases,* **2009,** *4,* 1-6.

40. Zan, G. H.; Jackman, J. A.; Kim, S. O.; Cho, N. J. Controlling lipid membrane architecture for tunable nanoplasmonic biosensing. *Small,* **2014,** *10,* 4828-4832.

41. Mornet, S.; Lambert, O.; Duguet, E.; Brisson, A. The formation of supported lipid bilayers on silica nanoparticles revealed by cryoelectron microscopy. *Nano Letters,* **2005,** *5,* 281-285.

42. Attwood, S. J.; Choi, Y.; Leonenko, Z. Preparation of DOPC and DPPC supported planar lipid bilayers for atomic force microscopy and atomic force spectroscopy. *Int. J. Mol. Sci.,* **2013,** *14,* 3514-3539.

43. Rigby-Singleton, S. M.; Davies, M. C.; Harris, H.; O'Shea, P.; Allen, S. Visualizing the solubilization of supported lipid bilayers by an amphiphilic peptide. *Langmuir,* **2006,** *22,* 6273-6279.

44. Kuech, T. R. Biological interactions and environmental transformations of nanomaterials. Ph. D. Dissertation, University of Wisconsin-Madison, 2015.

45. Chiantia, S.; Kahya, N.; Ries, J.; Schwille, P. Effects of ceramide on liquid-ordered domains investigated by simultaneous AFM and FCS. *Biophys. J.,* **2006,** *90,* 4500-4508.

46. Sezgin, E.; Levental, I.; Mayor, S.; Eggeling, C. The mystery of membrane organization: Composition, regulation and roles of lipid rafts. *Nat. Rev. Mol. Cell Biol.,* **2017,** *18,* 361-374.

47. Garcia-Arribas, A. B.; Busto, J. V.; Alonso, A.; Goni, F. M. Atomic force microscopy characterization of palmitoylceramide and cholesterol effects on phospholipid bilayers: A topographic and nanomechanical study. *Langmuir,* **2015,** *31,* 3135-3145.

48. Gkeka, P.; Angelikopoulos, P.; Sarkisov, L.; Cournia, Z. Membrane partitioning of anionic, ligand-coated nanoparticles is accompanied by ligand snorkeling, local disordering, and cholesterol depletion. *PLoS Comput. Biol.,* **2014,** *10,* e1003917.

49. Brown, D. A.; London, E. Functions of lipid rafts in biological membranes. *Annu. Rev. Cell Dev. Biol.,* **1998,** *14,* 111-136.

50. Grennan, A. K. Lipid rafts in plants. *Plant Physiol.,* **2007,** *143,* 1083-1085.

51. Alvarez, F. J.; Douglas, L. M.; Konopka, J. B. Sterol-rich plasma membrane domains in fungi. *Eukaryot. Cell,* **2007,** *6,* 755-763.

52. Bramkamp, M.; Lopez, D. Exploring the existence of lipid rafts in bacteria. *Microbiol. Mol. Biol. Rev.,* **2015,** *79,* 81-100.

53. Pike, L. J. Rafts defined: A report on the keystone symposium on lipid rafts and cell function. *J. Lipid Res.,* **2006,** *47,* 1597-1598.

54. Shaw, A. S. Lipid rafts: Now you see them, now you don't. *Nat. Immunol.,* **2006,** *7,* 1139-1142.

55. Drucker, P.; Gerke, V.; Galla, H. J. Importance of phospholipid bilayer integrity in the analysis of protein-lipid interactions. *Biochem. Biophys. Res. Commun.,* **2014,** *453,* 143-147.

56. Van Lehn, R. C.; Alexander-Katz, A. Pathway for insertion of amphiphilic nanoparticles into defect-free lipid bilayers from atomistic molecular dynamics simulations. *Soft Matter,* **2015,** *11,* 3165-3175.

Chapter 4: Atomic Force Microscopy of Supported Lipid Bilayers Containing Phase-segregated Domains: Considerations for Examining Bilayers across Multiple Techniques

Correlation of fluorescence and atomic force microscopies were done in collaboration with Eric Melby, Dehong Hu, and Galya Orr at the Environmental Molecular Sciences Laboratory at Pacific Northwest National Laboratory. Matlab analysis of force curves was done in collaboration with Jack Tilka.

4.1 Introduction

Solid-supported lipid bilayers (SLBs) are a versatile model system used to study the properties and behavior of cellular membranes. They provide a first approximation to study the surface chemistry of the cell, including lateral mobility and phase behavior in a controlled manner.[1-2] The benefits of using SLBs include ease of sample preparation,[3] ability to use various *in situ,* surface-sensitive characterization and imaging techniques,[1] and the chemical tunability to include relevant phospholipids and/or biomolecules found in actual cellular membranes.[4-6]

The cellular membranes of different organisms are composed of a complex mixture of phospholipids, proteins, sphingolipids, and sterols. Therefore, the composition of the best model system to represent a particular organism must be carefully considered. One well established model system for the outer leaflet of animal cytoplasmic membranes include the inclusion of zwitterionic phosphatidylcholine, sphingomyelin (SM), and neutral cholesterol (Chol), the majority components in these types of cellular membranes.[7] In this example, SM and Chol phase-segregate into domains within the SLB due to acyl chain saturation and preferential association of cholesterol with sphingomyelin.[2] These two components are enriched within the liquid-ordered (L_o) phase of the membrane, where the lipid tails are more ordered and the lipids are more tightly packed as compared to the liquid-disordered phase (L_d), which consists of the unsaturated

phosphatidylcholine lipids.[2] The resulting membrane is a supported lipid bilayer consisting of domains of L_o phase approximately ~1 nm taller than the underlying L_d phase.[8] Phase-segregated domains play an important biological role in cell signaling and trafficking.[9] However, while hypothesized to exist within animal,[7] plant,[10] fungal,[11] and bacterial[12] cell membranes, domains remain difficult to characterize due to their small size (10-200 nm)[13] and dynamic nature.[13-14]

The difficulty in studying phase-segregated domains within cellular membranes makes SLBs even more useful to study these vital cell membrane components. While a useful means to study the cellular membrane, various factors have been shown to influence the formation, structure, and properties of SLBs that need to be carefully considered when planning experiments (e.g., ionic strength and presence of divalent cations,[15-16] lipid head group charge,[17-18] and substrate[16,19-20]). In particular, both the surface charge and the roughness of the substrate have been shown to play a critical role in impacting the formation of SLBs.[17,21-22] However, little emphasis has been placed on the role of the substrate when using multiple techniques to characterize phase-segregated domain containing SLBs.

Ideally, the substrate used to form supported lipid bilayers will allow for lateral diffusion of the lipids to best mimic the behavior of a real cellular membrane. To allow for this lateral movement, successful supports for lipid bilayers (those forming quality bilayers with little or no defects) will retain a 1 to 2 nm water layer between the lipid headgroup and the surface.[1,23] This water layer highlights the importance of surface-vesicle interactions, including electrostatic, van der Waals, steric, and hydration forces, in SLB formation.[24-25] This typically results in a smooth, clean, hydrophilic substrate being the most suitable substrate for supported lipid bilayer formation.[1,26] Silica substrates, including mica (by atomic force microscopy (AFM[27-28]) and combined fluorescence/AFM methods[8,29]), optical glass (by fluorescence microscopy[5-6]), and

silica (by AFM[6,27]) have all been shown previously to form supported lipid bilayers containing phase-segregated domains. However, little emphasis has been placed in correlating these techniques and considering the role of the substrate on domain size, shape, and height.

The goal of this study was to use atomic force microscopy to characterize the structure of supported lipid bilayers containing phase-segregated domains on various substrates used in different *in situ* analytical methods. We highlight the importance of the underlying substrate in dictating the structure and size of phase-segregated domains. We focused on characterizing the bilayers across three silica based materials - mica, ultra-flat silicon dioxide, and glass bottom dishes. Finally, we extend these studies to include the correlation of fluorescence and atomic force microscopy to characterize the same bilayer using two techniques. Our findings provide important considerations when drawing conclusions on these bilayer systems across various techniques.

4.2 Materials and Methods

4.2.1 Preparation of small unilamellar vesicles

We prepared small unilamellar (SUVs) composed of 100% 1,2-dioleoyl-*sn*-glycero-3-phosphocholine (DOPC, 850375C, Avanti Polar Lipids) or a 60 mol% DOPC, 20 mol% plant-derived cholesterol (Chol, 700100P, Avanti Polar Lipids) and 20 mol% sphingomyelin from chicken egg yolk (SM, S0756, Sigma Aldrich) as previously described.[6] Briefly, the individual components were dissolved in chloroform and mixed to their desired ratios. They were vortexed to mix and the chloroform was evaporated off under a stream of nitrogen gas. We removed any residual chloroform by leaving the dried lipids under vacuum for at least 2 h. The dried film was rehydrated in 0.001 M NaCl buffered to pH 7.4 with 0.01 M HEPES, vortexed, and sonicated for 30 min. The solution was exposed to three cycles of freezing by liquid nitrogen and thawing via

sonication. We extruded the solution 11 times (Avanti 610000 extruder kit) through a 50 nm polycarbonate membrane filter (Whatman) to give SUVs.

4.2.2 Formation of supported lipid bilayers on various substrates

We formed supported lipid bilayers on mica (Highest Grade V1, Ted Pella) substrates, glass bottom dishes (P60G-1.5-30-F, MatTek Corporation), and ultraflat B-doped silicon wafers with a 200 nm thermal oxide layer (Ted Pella). Mica was freshly cleaved using double sided tape prior to use. Ultra-flat silica was rinsed with ethanol, water (3x) and exposed to UV-light (185 nm) for 20 min prior to use. The glass bottom dishes were treated with 6 M NaOH for 2 h and rinsed with copious amounts of nanopure water (18 MΩ) prior to use. For mica and ultra-flat silica, we adhered the substrates to the bottom of a glass bottom dish using 5 minute epoxy (ITW Polymer Adhesives). The substrates were equilibrated in 0.150 M NaCl with 0.005 M $CaCl_2$ buffered to pH 7.4 with 0.01 M HEPES for 10 min. Vesicles were added in this same equilibration buffer (0.03125 mg/mL for mica, 0.0625 mg/mL for ultraflat SiO_2 and glass bottom dishes, as these concentrations were found to most consistently form defect-free bilayers with minimal intact vesicles remaining) for up to 1 hour above the transition temperature of the lipids used to promote rupture and formation of supported lipid bilayers.[28] The sample was cooled to room temperature and rinsed with at least 12 mL of vesicle-free buffer to remove any loosely adhered vesicles. We exchanged the buffer for calcium-free buffer, followed by buffer with 0.010 M NaCl. In each case, the solution was exchanged with at least 12 mL.

4.2.3 Atomic force microscopy imaging and force spectroscopy

Imaging on mica and ultra-flat silica substrates was conducted in PeakForce Tapping™ mode using a Dimension Icon Atomic Force Microscope (Bruker). Silicon nitride probes (Bruker, DNP, NPG, or ScanAyst Fluid+) with force constants of 0.24 N/m for DNP and NPG and 0.7 N/m

for ScanAyst Fluid+ were used for all imaging. While the properties of the probes varied slightly there was no differences observed in domain height or structure across different probes used. Prior to imaging, the deflection sensitivity was determined by ramping the probe against a hard fused silica substrate and fitting the linear portion of the force-distance curve. The spring constant of the cantilever was determined using the thermal tune method and fitting the spectral density function to a Lorentzian curve.[30]

In a subset of experiments, to ensure bilayer formation and characterize the bilayer breakthrough force, we collected force-distance curves. A set of force distance curves were collected at various spots across the bilayers. We worked in "point-and-shoot" mode and had control over whether we were puncturing a liquid-ordered or liquid-disordered phase. A ramp size of 200 nm and a tip velocity of 400 nm/s were used to collect the force curves. We analyzed the force curves for a breakthrough point, indicating the tip had penetrated through the bilayer, using Matlab (see code in A4.1).

4.2.4 Combined AFM and fluorescence studies

In efforts to correlate AFM and fluorescence studies we used a MFP-3D-BIO AFM with an inverted optical microscope (Asylum Research). Imaging on this set-up was conducted in tapping mode using silicon nitride probes (DNP, Bruker). Bilayers were formed in glass bottom dishes as previously described, but in this case the vesicles used contained 0.1 mol% of the fluorophore, Atto647N 1,2-dioleoyl-sn-glycero-3-phosphoethanolamine (DOPE, Atto-Tec, Siegen, Germany, λ_{ex} = 642 nm, λ_{em} = 667 nm).

A protocol was optimized for the successful correlation of fluorescence and atomic force microscopy. We aligned the AFM tip in air with no sample present. The AFM head was removed, a drop of oil was added to the objective, and the sample dish, along with the magnetic petri dish

holder was put in place. The objective was raised to focus on the sample. A drop of buffer was added to the AFM tip and the AFM head was replaced on top of the sample. The AFM head was lowered to submerge the tip and the resonant frequency of the cantilever was determined by sweeping the frequencies. The bilayer surface was found and focused on by bringing the fluorescence signal from the Atto647N dye into focus. The AFM tip was brought closer to the surface by engaging on the surface and then bringing the tip back up slightly. We used the optical microscope on the AFM to locate the cantilever within the field of view of the fluorescence microscope. This was best done by finding the dark circle/halo (the objective from the inverted fluorescence microscope) within the AFM camera. We centered the AFM tip within that circle. At this point, if desired, brightfield images were collected using the AFM optical microscope. Fluorescence images were collected and the AFM tip was moved to any features of interest found on the fluorescence images. Finally, the objective was lowered (failure to do so will result in periodic noise within the AFM images) and AFM scans were collected.

4.2.5 Analysis of AFM images

Initial image analysis, roughness calculations, and line scan analysis of heights of phase-segregated domains were conducted using Gwyddion.[31] To determine the area, perimeter, and fractional coverage of the domains, the images were processed using FIJI.[32] Briefly, the noise of the image was removed using the "despeckle" feature, which is a median filter to remove noise. A color threshold was adjusted to select only the domain features on the images, a threshold of 20 pixels was also set to ensure no noise was counted as a domain. A mask of outlined domains was made and the resulting area and perimeter of each domain was given. The fractional area was determined by dividing the sum of the area of the domains by the total area of the image. An example of this analysis can be found in Figure A4.1.

4.3 Results and Discussion

4.3.1 Characterization of substrates prior to SLB formation

In order to make comparisons of supported lipid bilayers formed across various analytical techniques we first characterized the underlying substrates typically used in AFM, fluorescence, and quartz crystal microbalance experiments. We used AFM to characterize the topography and surface roughness of mica, glass bottom dishes, QCM-D wafers, and ultra-flat silica. Figure 4.1 shows the topography and root mean square (RMS) roughness of each of the substrates. We found that mica has the smallest RMS value (122 ± 26 pm), followed by ultra-flat silica (204 ± 30 pm), glass bottom dishes (239 ± 61 pm), and finally SiO_2-coated QCM-D crystals (1.08 ± 0.05 nm).

Given the large RMS value of QCM-D crystals, likely due to the sputter-coated gold the SiO_2 layer is deposited on, the L_o domain, ~1 nm above the L_d phase, may be difficult to observe on the QCM-D crystal. We therefore used ultra-flat SiO_2, which also has an oxide layer on its surface to be used as a representative surface when considering studies conducted by QCM-D and AFM.

4.3.2 Comparison of SLB formation on various substrates

We used mica as a standard in these studies as SLBs containing phase-segregated domains have been previously characterized by AFM on mica.[8,28] We characterized both 100% L_d bilayers (100% DOPC) and bilayers containing both L_d and L_o phases (60/20/20 mol% DOPC/SM/Chol). Figure 4.2a shows a purely DOPC bilayer. There are no distinguishing features, shown by the flat line profile across the bilayer, and confirming that the bilayer follows the topography of the underlying mica substrate.[17] To ensure that a SLB did form and it was not just the underlying mica being imaged, there are three commonly used approaches to determine the presence of a bilayer – characteristic puncture events by force spectroscopy,[33] determining the height across a defect in

the bilayer,[34] or "nano-shaving" a small region of the bilayer by working at high forces and confirming the height of the bilayer across this defect.[35] In these studies, for pure DOPC bilayers we conducted force-distance curves to confirm the presence of the bilayer.[33] In the case of 60/20/20 mol% DOPC/SM/Chol, the presence of the characteristic lipid rafts, ~1 nm taller in height, confirmed the presence of the bilayer.[8] Figure 4.3a shows a characteristic force-distance curve for a DOPC SLB. When the AFM tip and the bilayer are far apart, no interaction is observed between the tip and the sample (baseline near zero in Figure 4.3a); however, as the tip approaches the sample short-range interactions cause the tip to be pulled towards the sample. Eventually the tip and the bilayer come in mechanical contact and as the force is increased, the membrane will elasticity deform and eventually a threshold value is reached (breakthrough force) where the AFM probe penetrates through the lipid bilayer and hits the underlying surface.[33] For DOPC bilayers we found this value to occur at 3.19 ± 0.01 nN, consistent with previous studies.[28] Force-distance curves and the characteristic breakthrough event is a convenient way to confirm the presence of a SLB.

To investigate the size and shape of phase-segregated domains we also formed SLBs containing 60/20/20 mol% DOPC/SM/Chol. Figure 4.2b, 4.2c show the topography of the phase-segregated domains on mica. They are 0.8 ± 0.1 nm taller than the underlying L_d phase and have a fractional coverage of 11.2 ± 1.0% (Table 4.1). The domains that form on mica are much larger in area (range of 0.128 to 2.95 μm^2) as compared to what is expected to be found within naturally occurring membranes (8×10^{-5} to 0.03 μm^2 assuming a circular shape and a size range of 10-200 nm).[13] We also observed an increase in the breakthrough force associated with the L_o phase as compared to the L_d phase ($p < 0.001$), which has been shown previously on similar systems.[28] This

increase is likely due to the increased sphingomyelin – cholesterol interaction resulting in a more tightly pack and ordered phase as compared to the case of unsaturated phospholipids.

While the larger size of phase-segregated domains on mica allows for easier characterization by surface-sensitive and imaging techniques, they may behave differently than those naturally present. We observed domains with larger heights, smaller areas, and smaller perimeters (Table 4.1) when investigating the role of the substrate and analyzing phase-segregated domains on ultraflat SiO_2 and glass bottom dishes. The domains were higher on ultraflat SiO_2 (0.9 ± 0.1, $p < 0.001$) as compared to mica, but they were highest on glass bottom dishes (1.2 ± 0.2, $p < 0.001$). We attribute this increase in height and increase in standard deviation in height to the increase in the RMS value found for the underlying substrate.

Figure 4.4a shows a supported lipid bilayer of pure DOPC formed on an ultraflat SiO_2. Again, a featureless topography is observed suggesting the bilayer is of uniform height and follows the topography of the underlying surface. Upon the inclusion of sphingomyelin and cholesterol (Figure 4.4b), L_o domains formed and covered 6.5 ± 1.7% of the imaged surface. The domains were much smaller than those formed on mica (range of areas from 1.91-63.7 $\times 10^{-3}$ nm^2 with an average perimeter of 375 ± 247 nm). Figure 4.5a shows domains formed on glass bottom dishes with larger size than those of SiO_2 formed, but with comparable perimeters. However, the fractional area of domains across glass bottom dishes is much larger than that observed for both mica and ultraflat SiO_2 (18.7 ± 0.8%).

Ultimately, all three substrates showed a large variation in the sizes of the domains formed both in terms of area and in terms of perimeter. The standard deviations were large for all calculated values (Table 4.1). This suggests that the methods employed in this study are not ideal for the formation of uniformly sized domains. The differences observed across substrates

highlights the likelihood that both surface roughness and substrate charge play a strong role in the distribution and size of the domains. It has been shown previously that increasing the surface roughness results in a decrease in the lipid diffusion coefficient.[36] We hypothesize that this increased diffusion barrier due to the roughness of the surface may result in smaller domain formation on the rougher substrates.

4.3.3 Spatial and temporal correlation of phase-segregated domains using AFM and fluorescence microscopy

To demonstrate the utilization of multiple techniques in characterizing these bilayers we correlated fluorescence microscopy with AFM. Fluorescence microscopy is a powerful technique that can provide chemical information and an optical image of a sample, through the appropriate use of fluorophores. Combining fluorescence with atomic force microscopy, we can gain structural, surface, and chemical properties. In order to use AFM and fluorescence microscopy in combination with one another, we first optimized a protocol for the use of the combined AFM/fluorescence set up as described above. We chose to work on glass bottom dishes due to the fact that smaller, more representative of those naturally found, domains formed on these substrates and they were transparent which allowed for illumination from the bottom.

Figure 4.5 shows the spatial and temporal correlation of SLBs containing domains. The small size of the domains make them unobservable by light microscopy,[13] but by fluorescence we observe the formation of bright and dark regions. The Atto647N DOPE dye has been shown previously to associate with the liquid-disordered phase.[6] Upon excitation with a 642 nm laser, the phase-segregated domains will appeared dark and the remaining liquid-disordered bilayer appeared bright, confirming the association of the dye with the L_d phase.

Despite the small sizes of the domains formed on the glass bottom dishes, we were able to correlate the AFM and fluorescence images through various "markers." For example, the blue arrows in Figure 4.5 point out two defects (holes) observed by AFM. These holes appear dark by fluorescence and could be confused for a domain as compared to a hole. However, having the corresponding AFM data allowed for the direct correlation of the two techniques. In other cases, larger domains or domains of distinctive shapes were used to correlate the two channels. Our work here presents the first example of correlating AFM and fluorescence on phase-segregated domains of this smaller size. Previous work in correlating AFM and fluorescence on similar bilayers used mica substrates where the domains were much larger.[8,29]

4.4 Conclusions

We were successfully able to form supported lipid bilayers containing phase-segregated domains on three different substrates – mica, ultraflat SiO_2, and glass bottom dishes. We found that the size of the domains (area, perimeter, and fractional coverage) varied for each of the substrates. This highlights a need to consider the effect of the substrate on the characteristics of the liquid-ordered domains and in drawing conclusions on these systems when using various analytical tools that require different substrates. Naturally occurring domains may be of a smaller size than those observed on mica, which is a typically used substrate in these studies. Therefore, it may be necessary to weigh the factors of relevance of the study as compared to ease of studying the domains.

The naturally occurring size of domains is smaller than the resolution of light microscopy.[13] This makes both AFM and super-resolution fluorescence spectroscopy attractive tools to study these systems. The optimization of the combined AFM-fluorescence technique presented here works towards establishing a robust system to study lipid rafts by complementary methods.

The work presented here focused on the vesicle fusion method in the formation of SLBs. The vesicle fusion method requires a large adhesive energy between the substrate and the lipids to induce vesicle fusion and rupture. However, others have shown that different methods have promoted SLB formation even when vesicle fusion failed.[24] It would be interesting to explore how different means of membrane formation (e.g., solvent assisted lipid bilayer, Langmuir Blodgett, bubble collapse deposition) may impact the size and shape of phase-segregated domains on various substrates.

Liquid-ordered domains are hypothesized to be a reactive site responsible for many chemical reactions. For example, an increase in attachment of positively charged gold nanoparticles was observed in the presence of phase-segregated domains[6] and the HIV fusion peptide was shown to preferentially target the L_o-L_d phase boundary.[37] The hypothesis that domain edges are a reactive site will undoubtedly result in the need for methods to control and understand the factors that influence the amount of exposed edge sites in phase-segregated domain containing SLBs. While this may simply be controlled by varying the amount of sphingomyelin and cholesterol present and thus the fractional coverage by domains,[6] one may also consider choosing a substrate that provides either larger domains or more total edges, as described in this work.

4.5 Tables

Table 4.1. Summary of characteristics of 60/20/20 mol% DOPC/SM/Chol bilayers formed on mica, ultraflat SiO_2, and glass bottom dishes as determined by AFM.[a]

Substrate	Average Domain Height (nm)	Average Domain Area (nm^2)	Range of Domain Area (nm^2)	Average Domain Perimeter (nm)	Average Fractional Coverage of Domains (%)
Mica	0.8 ± 0.1 *N = 198*	$(8.9 \pm 4.9) \times 10^5$ *N = 355*	$(1.3 \text{ to } 29.5) \times 10^5$	$(3.4 \pm 1.1) \times 10^3$ *N = 355*	11.2 ± 1.0 *N = 7*
Ultraflat SiO_2	0.9 ± 0.1 *N = 115*	$(7.2 \pm 7.3) \times 10^3$ *N = 704*	$(1.9 \text{ to } 63.7) \times 10^3$	375 ± 247 *N = 704*	6.5 ± 1.7 *N = 3*
Glass Bottom Dish	1.2 ± 0.2 *N = 100*	$(2.3 \pm 3.6) \times 10^5$ *N = 612*	$(1.9 \text{ to } 365) \times 10^3$	625 ± 606 *N = 612*	18.7 ± 0.8 *N = 3*

[a] Imaging was conducted across at least three spots on at least two different samples. The *N* value listed is for the number of domains analyzed in the reported values.

4.6 Figures

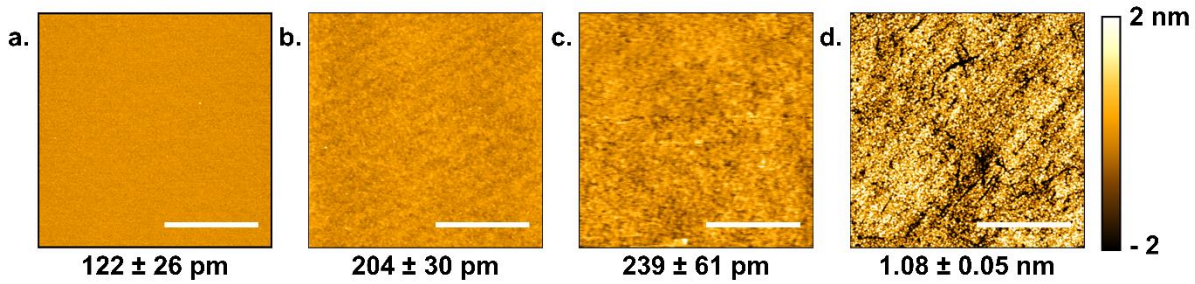

Figure 4.1. Atomic force microscopy topography images of (a) mica, (b) ultraflat silica, (c) glass bottom dish, (d) quartz crystal microbalance sensor. All images were collected in aqueous buffer at pH 7.4. The value under the image is the RMS value across at least three different spots of each substrate.

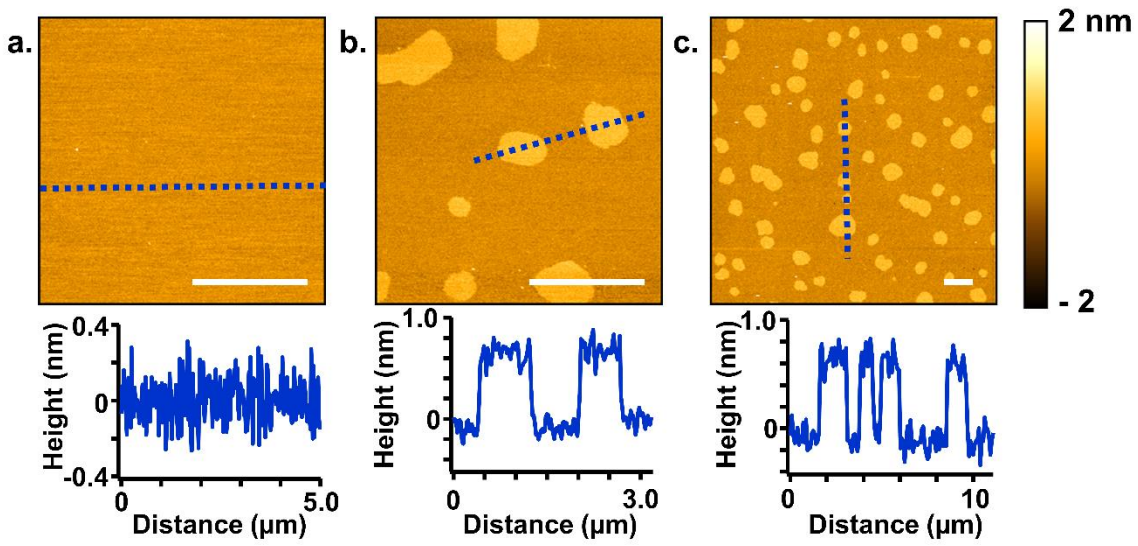

Figure 4.2. Atomic force microscopy topography images and corresponding line profiles (across dashed lines) of (a) 100% DOPC, (b) 60/20/20 mol% DOPC/SM/Chol, (c) zoomed out scan of 60/20/20 mol% DOPC/SM/Chol. Scale bars are 2 μm. Z-scale corresponds to all images.

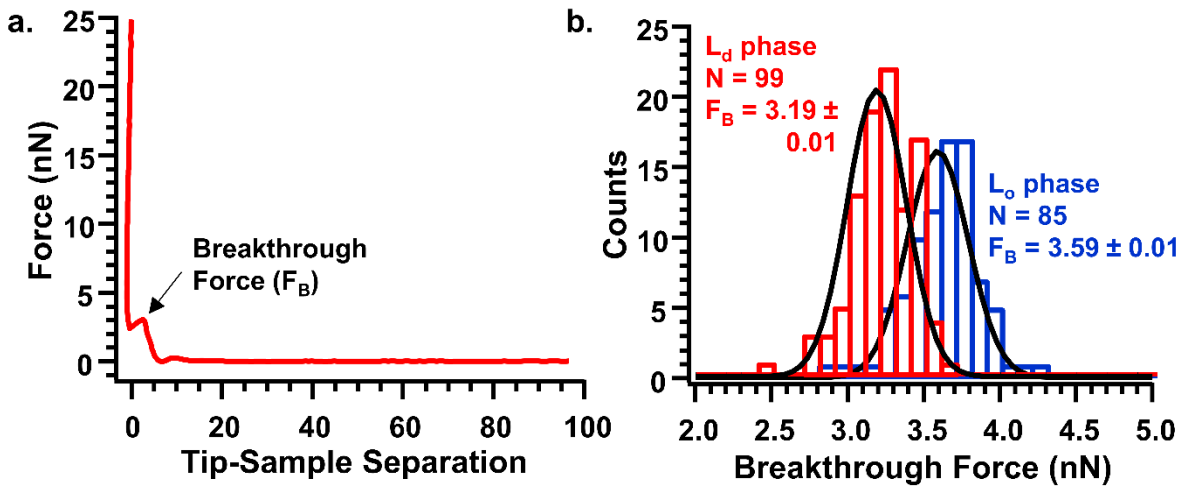

Figure 4.3. (a) Representative force-distance curve on a pure DOPC bilayer showing the characteristic breakthrough feature. (b) Histograms showing the breakthrough forces (F_B) of the liquid-disordered (red) and liquid-ordered (blue) phases of a 60/20/20 mol% DOPC/SM/Chol bilayer on a mica substrate in 0.010 M NaCl solution buffered to pH 7.4 with 0.010 M HEPES buffer. The distributions were fit to a Gaussian function to determine the F_B value, which represents the average and standard deviation of the denoted N number of curves.

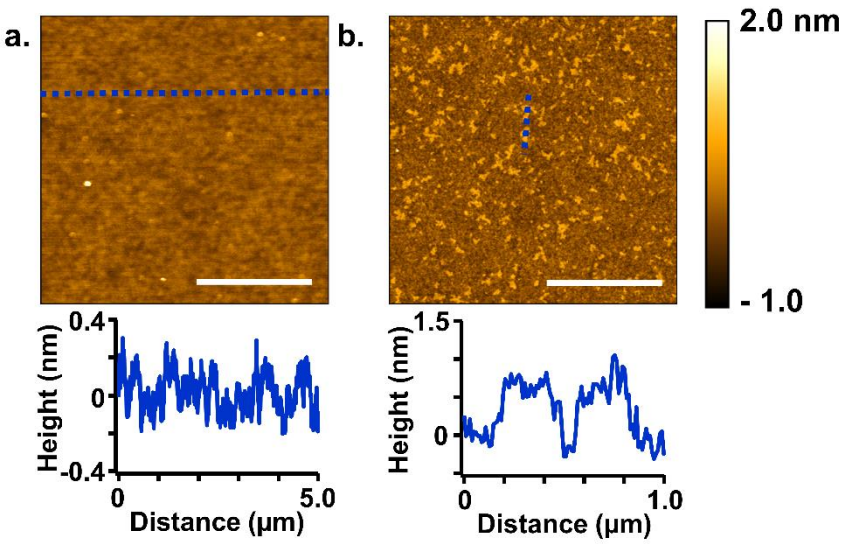

Figure 4.4. Atomic force microscopy images and representative line scans of (a) DOPC and (b) 60/20/20 mol% DOPC/SM/Chol on an ultraflat SiO_2 wafer. Scale bars are 2 μm. Z-scale corresponds to both images.

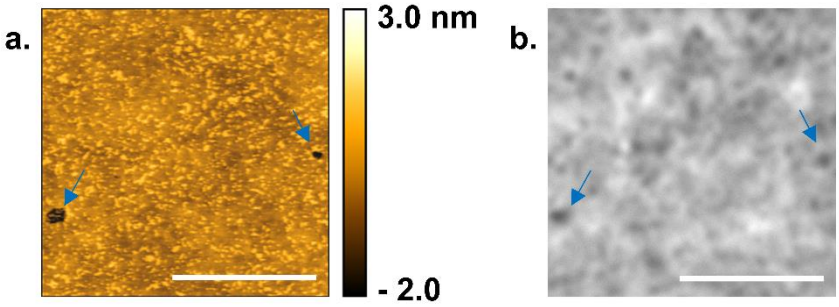

Figure 4.5. Spatially and temporally correlated (a) atomic force microscopy topography image and (b) fluorescence microscopy image of 60/20/20 DOPC/SM/Chol + 0.1% of the fluorophore Atto DOPE 647N. Scale bars are 5 µm. Blue arrows point to defects observed in the AFM image and holes in the fluorescence image, which were used to correlate the images.

4.7 References

1. Castellana, E. T.; Cremer, P. S. Solid supported lipid bilayers: From biophysical studies to sensor design. *Surf. Sci. Rep.,* **2006,** *61,* 429-444.

2. Kiessling, V.; Yang, S. T.; Tamm, L. K. Supported lipid bilayers as models for studying membrane domains. *Curr. Top. Membr.,* **2015,** *75,* 1-23.

3. Richter, R.; Mukhopadhyay, A.; Brisson, A. Pathways of lipid vesicle deposition on solid surfaces: A combined QCM-D and AFM study. *Biophys. J.,* **2003,** *85,* 3035-3047.

4. Kaufmann, S.; Ilg, K.; Mashaghi, A.; Textor, M.; Priem, B.; Aebi, M.; Reimhult, E. Supported lipopolysaccharide bilayers. *Langmuir,* **2012,** *28,* 12199-12208.

5. Dietrich, C.; Bagatolli, L. A.; Volovyk, Z. N.; Thompson, N. L.; Levi, M.; Jacobson, K.; Gratton, E. Lipid rafts reconstituted in model membranes. *Biophys. J.,* **2001,** *80,* 1417-1428.

6. Melby, E. S.; Mensch, A. C.; Lohse, S. E.; Hu, D.; Orr, G.; Murphy, C. J.; Hamers, R. J.; Pedersen, J. A. Formation of supported lipid bilayers containing phase-segregated domains and their interaction with gold nanoparticles. *Environ. Sci.: Nano,* **2016,** *3,* 45-55.

7. Brown, D. A.; London, E. Functions of lipid rafts in biological membranes. *Annu. Rev. Cell Dev. Biol.,* **1998,** *14,* 111-136.

8. Chiantia, S.; Kahya, N.; Ries, J.; Schwille, P. Effects of ceramide on liquid-ordered domains investigated by simultaneous AFM and FCS. *Biophys. J.,* **2006,** *90,* 4500-4508.

9. Sezgin, E.; Levental, I.; Mayor, S.; Eggeling, C. The mystery of membrane organization: Composition, regulation and roles of lipid rafts. *Nat. Rev. Mol. Cell Biol.,* **2017,** *18,* 361-374.

10. Grennan, A. K. Lipid rafts in plants. *Plant Physiol.,* **2007,** *143,* 1083-1085.

11. Alvarez, F. J.; Douglas, L. M.; Konopka, J. B. Sterol-rich plasma membrane domains in fungi. *Eukaryot. Cell,* **2007,** *6,* 755-763.

12. Bramkamp, M.; Lopez, D. Exploring the existence of lipid rafts in bacteria. *Microbiol. Mol. Biol. Rev.,* **2015,** *79,* 81-100.

13. Pike, L. J. Rafts defined: A report on the keystone symposium on lipid rafts and cell function. *J. Lipid Res.,* **2006,** *47,* 1597-1598.

14. Shaw, A. S. Lipid rafts: Now you see them, now you don't. *Nat. Immunol.,* **2006,** *7,* 1139-1142.

15. Redondo-Morata, L.; Giannotti, M. I.; Sanz, F. Structural impact of cations on lipid bilayer models: Nanomechanical properties by AFM-force spectroscopy. *Mol. Membr. Biol.,* **2014,** *31,* 17-28.

16. Richter, R. P.; Berat, R.; Brisson, A. R. Formation of solid-supported lipid bilayers: An integrated view. *Langmuir,* **2006,** *22,* 3497-3505.

17. Mornet, S.; Lambert, O.; Duguet, E.; Brisson, A. The formation of supported lipid bilayers on silica nanoparticles revealed by cryoelectron microscopy. *Nano Letters,* **2005,** *5,* 281-285.

18. Garcia-Manyes, S.; Oncins, G.; Sanz, F. Effect of pH and ionic strength on phospholipid nanomechanics and on deposition process onto hydrophilic surfaces measured by AFM. *Electrochim. Acta,* **2006,** *51,* 5029-5036.

19. Nussio, M. R.; Oncins, G.; Ridelis, I.; Szili, E.; Shapter, J. G.; Sanz, F.; Voelcker, N. H. Nanomechanical characterization of phospholipid bilayer islands on flat and porous substrates: A force spectroscopy study. *J. Phys. Chem. B,* **2009,** *113,* 10339-10347.

20. Richter, R. P.; Brisson, A. Characterization of lipid bilayers and protein assemblies supported on rough surfaces by atomic force microscopy. *Langmuir,* **2003,** *19,* 1632-1640.

21. Radler, J.; Strey, H.; Sackmann, E. Phenomenology and kinetics of lipid bilayer spreading on hydrophilic surfaces. *Langmuir,* **1995,** *11,* 4539-4548.

22. Cremer, P. S.; Boxer, S. G. Formation and spreading of lipid bilayers on planar glass substrates. *J. Phys. Chem. B,* **1999,** *103,* 2554-2559.

23. Tamm, L. K.; McConnell, H. M. Supported phospholipid bilayers. *Biophys. J.,* **1985,** *47,* 105-113.

24. Mager, M. D.; Almquist, B.; Melosh, N. A. Formation and characterization of fluid lipid bilayers on alumina. *Langmuir,* **2008,** *24,* 12734-12737.

25. Cha, T.; Guo, A.; Zhu, X. Y. Formation of supported phospholipid bilayers on molecular surfaces: Role of surface charge density and electrostatic interaction. *Biophys. J.,* **2006,** *90,* 1270-1274.

26. Picas, L.; Milhiet, P. E.; Hernandez-Borrell, J. Atomic force microscopy: A versatile tool to probe the physical and chemical properties of supported membranes at the nanoscale. *Chem. Phys. Lipids,* **2012,** *165,* 845-860.

27. Seghezza, S.; Dante, S.; Diaspro, A.; Canale, C. High resolution nanomechanical characterization of multi-domain model membranes by fast force volume. *J. Mol. Recognit.,* **2015,** *28,* 742-750.

28. Sullan, R. M.; Li, J. K.; Hao, C.; Walker, G. C.; Zou, S. Cholesterol-dependent nanomechanical stability of phase-segregated multicomponent lipid bilayers. *Biophys. J.,* **2010,** *99,* 507-516.

29. Shaw, J. E.; Epand, R. F.; Epand, R. M.; Li, Z.; Bittman, R.; Yip, C. M. Correlated fluorescence-atomic force microscopy of membrane domains: Structure of fluorescence probes determines lipid localization. *Biophys. J.,* **2006,** *90,* 2170-2178.

30. Hutter, J. L.; Bechhoefer, J. Calibration of atomic-force microscope tips. *Rev. Sci. Instrum.,* **1993,** *64,* 1868-1873.

31. Nečas, D.; Klapetek, P. Gwyddion: An open-source software for SPM data analysis. *Cent. Eur. J. Phys.,* **2012,** *10,* 181-188.

32. Schindelin, J.; Arganda-Carreras, I.; Frise, E.; Kaynig, V.; Longair, M.; Pietzsch, T.; Preibisch, S.; Rueden, C.; Saalfeld, S.; Schmid, B.; Tinevez, J. Y.; White, D. J.; Hartenstein, V.; Eliceiri, K.; Tomancak, P.; Cardona, A. Fiji: An open-source platform for biological-image analysis. *Nat. Methods,* **2012,** *9,* 676-682.

33. Garcia-Manyes, S.; Sanz, F. Nanomechanics of lipid bilayers by force spectroscopy with AFM: A perspective. *Biochim. Biophys. Acta,* **2010,** *1798,* 741-749.

34. Attwood, S. J.; Choi, Y.; Leonenko, Z. Preparation of DOPC and DPPC supported planar lipid bilayers for atomic force microscopy and atomic force spectroscopy. *Int. J. Mol. Sci.,* **2013,** *14,* 3514-3539.

35. Kumar, S.; Hoh, J. H. Direct visualization of vesicle-bilayer complexes by atomic force microscopy. *Langmuir,* **2000,** *16,* 9936-9940.

36. Seu, K. J.; Pandey, A. P.; Haque, F.; Proctor, E. A.; Ribbe, A. E.; Hovis, J. S. Effect of surface treatment on diffusion and domain formation in supported lipid bilayers. *Biophys. J.,* **2007,** *92,* 2445-2450.

37. Yang, S. T.; Kiessling, V.; Simmons, J. A.; White, J. M.; Tamm, L. K. HIV gp41-mediated membrane fusion occurs at edges of cholesterol-rich lipid domains. *Nat. Chem. Biol.,* **2015,** *11,* 424-431.

Chapter 5: Optimization of Atomic Force Microscopy Parameters for the Nanomechanical Characterization of Fixed and Live Trout Gill

This work was done in collaboration with Kyoungtea Kim in Joel Pedersen's lab. Kyoungtea grew and prepared the trout gill cells for imaging.

5.1 Introduction

Mechanical properties (e.g., elasticity, adhesiveness, and viscosity) play a critical role in many fundamental biological processes such as, cell growth, differentiation, protein synthesis, motility, mechanotransduction, and apoptosis.[1-2] Changes to the mechanical properties of a cell can disrupt its normal behavior and is a key indicator of a variety of different pathologies.[3] Previously, external stressors such as, drugs,[4-5] disease,[6-7] and nanoparticles[8-10] have all been shown to induce mechanical changes to the cellular membrane of a variety of cell types. Examples of these impacts include, stiffening of epithelial cells after exposure to gold nanorods,[9] reduction in elasticity and viscosity of L929 cells after exposure to a drug, cytochalasin D, due to disruption of actin filaments,[5] and reduction in stiffness in diseased human cervical cells as compared to healthy cells.[7] While it is difficult to generalize the impact of different types of stressors across different cell lines, the fact that mechanical changes to the cell directly impact cell function highlights the importance of characterizing the mechanical properties of various model cell lines.

The studies mentioned above all have one commonality – the use of atomic force microscopy (AFM) to characterize the mechanical response of a chosen cell line to an applied stressor. The AFM was invented in order to work on insulating surfaces in ambient conditions, unlike its predecessor, the scanning tunneling microscope.[11] The technique uses a sharp tip at the end of a cantilever that is rastered across the sample. The amount of interaction (or force) applied to the sample is specified and maintained via a feedback mechanism. A laser is aligned to the end

of the tip and as the tip is scanned across the surface, a piezo moves either the tip or the sample to maintain the desired amount of tip-sample interaction. In doing so, the laser light is reflected from the cantilever to a position-sensitive photodetector and any variations in the position of that laser light on the detector correspond to changes in height on the surface of the sample. Traditional AFM has long been recognized as a valuable tool in characterizing biological structures with unprecedented resolution, in real time, and under biological conditions (pH, ionic strength, and temperature controlled).[12] Imaging of biological structures such as DNA,[13-14] supported lipid bilayers,[15-16] and proteins[17] have all been conducted using AFM. Similarly, imaging of cells, both live[18-20] and fixed,[18-19] has been carried out using traditional AFM methods. However, AFM on cells is a difficult task that requires great attention to proper sample preparation, including substrate choice, cell preparation, scanning probe choice, and imaging parameters.[20] In order to obtain reliable results and avoid sample damage, optimization of sample preparation and imaging parameters is crucial for conducting AFM on cells.

Recent advancements in AFM technology have been aimed at simplifying the process of fluid imaging, increasing spatiotemporal resolution, and decreasing the required imaging force to minimize sample and tip damage.[21-22] One recent development, PeakForce Quantitative Nanomechanical Mapping (PFQNM) Atomic Force Microscopy, allows for the simultaneous mapping of deformation, modulus, dissipation, and adhesion in addition to topography.[21] This technique provides control over the forces applied to the sample down to the pico-Newton scale, which prevents sample damage and allows for high resolution imaging of cells. The ability to map nanomechanical properties in addition to topography provides a novel platform for the quantitative characterization of cell properties with unprecedented resolution. The optimization of PFQNM

AFM imaging will allow for the quantitative characterization of the mechanical properties of cells before and after exposure to various stressors.

Here we optimize a method using atomic force microscopy for the nanomechanical characterization of a model epithelial cell, gill cells from a rainbow trout (*Oncorhynchus mykiss*, RTgill-W1). We chose to study trout gill cells because they have previously been established as a model system for understanding mechanisms of toxicity in fish and are often used to evaluate the toxicity of different stressors.[23-24] However, little is known about the mechanical properties of these cells. We begin with method development by considering various factors that can impact the results of the technique, such as the mode of AFM operation, the shape and stiffness of the AFM probe used, and the confluency of the cells on various substrates. We use PFQNM to determine the height, modulus, deformation, dissipation, and adhesion of both fixed and live trout gill cells for the first time on this cell line. This work establishes a basis to study any mechanical changes that may be induced to these cells due to external stressors, such as nanomaterials.

5.2 Materials and Methods

5.2.1 Trout gill cell preparation

The rainbow trout gill cell line (American Type Culture Collection, Manassas, VA) were routinely maintained in Leibovitz's L-15 medium, with l-glutamine (Sigma-Aldrich Chemical Co., St. Louis, MO) supplemented with 1% antibiotics (100 U/ml penicillin and 100 g/ml streptomycin, GE Healthcare Life Sciences, Logan, UT) and 10% fetal bovine serum (Cell Applications Inc., San Diego, CA) at 20° C in an incubator containing normal atmosphere. For the AFM studies, 2.2 $\times 10^5$ cells were seeded in 21.5 cm^2 cell culture dishes (Fisher Scientific, Markham, ON). Cells were allowed to grow for 6 days to attain 100 % confluency, 5 days for ~75 % confluency, and 7 days to be past confluency.

To fix the cells, after cells reached the desired confluency, cells were rinsed with pH 7.4 phosphate-buffered saline (PBS) buffer (Lonza, Basel, Switzerland) three times. The cells were then treated with 4 % paraformaldehyde in 0.1 M PBS buffer (Santa Cruz Biotechnology, Dallas, TX) at room temperature. After 10 min, the paraformaldehyde was removed and the cells were subsequently washed with PBS twice.

5.2.2 Atomic force microscopy imaging and nanomechanical mapping

Imaging and nanomechanical mapping were conducted in PeakForce Tapping™ Quantitative Nanomechanical Mapping (PFQNM) mode on a Dimension Icon Atomic Force Microscope (Bruker, Santa Barbara, CA). We monitored topography, PeakForce error, adhesion, deformation, DMT modulus, and dissipation simultaneously for all samples studies. Samples were prepared as described above. Various types of AFM probes (all from Bruker AFM Probes) were explored in this work as described below, but ultimately final images were collected with a silicon nitride probe (DNP-C) with a nominal resonant frequency of 56 kHz, spring constant of 0.24 N/m, and tip radius of 20 nm.

Regardless of probe type, prior to imaging and nanomechanical characterization, the probe was first calibrated to determine its deflection sensitivity and spring constant, which allows for the conversion of the voltage signal from the photodetector into a unit of force. The deflection sensitivity is a measure of the cantilever's deflection (distance) for a certain change in voltage measured by the detector.[25] To do this, we ramped the probe over a hard, fused silica substrate (Bruker) in air to obtain a plot of deflection versus position of the piezo and found the slope of the contact regime of the plot, resulting in a value with units of nm/V.[26] We found an average deflection sensitivity value using six different force curves. Once the deflection sensitivity was known, Hooke's Law:

$$F = kx \quad (1)$$

where F the force, k is the spring constant, and x is the displacement of the laser on the detector (determined using the deflection sensitivity), was used to determine the corresponding force. We determined the spring constant using the thermal tune method and fitting the resulting power spectral density plot to a Lorentzian curve.[27]

All imaging was conducted in fluid, either supplemented Leibovitz's L-15 medium or PBS buffer at room temperature, 24.5°C. The addition of fluid to the AFM tip changes the optical path of the AFM detection laser; therefore, we determined the deflection sensitivity in fluid using the previously determined spring constant of the cantilever to account for this difference.[28-29]

5.3 Results and Discussion

5.3.1 PFQNM as an imaging mode

In order to investigate the mechanical properties of both live and fixed cells, we used PFQNM. Figure 5.1 shows the basic operation of PFQNM as an AFM imaging mode. A set amount of force is designated and maintained via a feedback mechanism. The piezo scanner is driven in a nonlinear extension and retraction cycle to monitor force over time.[21] This generates the plot shown in Figure 5.1a. The tip starts far from the sample (point 1 in Figure 5.1a) where there are little or no forces acting on the tip. As the tip begins to approach the sample (red curve), the cantilever is pulled towards the sample, resulting in attractive adhesive forces. At point 2 in Figure 5.1a, the stiffness of the cantilever is overcome by the attractive forces that pull the tip and the sample surface into contact. The force continues to increase until the designated PeakForce setpoint is reached (point 3, Figure 5.1a). At this point, the withdraw cycle of the tip begins (blue curve), where the tip is lifted from the sample surface. The force begins to decrease until a minimum is reached, which represents the adhesive forces between the tip and the sample (point

4, Figure 5.1a). The tip continues to withdraw from the sample until the tip loses contact with the sample and minimal long range forces are felt by the tip causing a near zero or zero force (point 5, Figure 5.1a). This cycle is repeated at a frequency that is lower than the resonant frequency of the cantilever, but fast enough to collect a force-distance curve at each pixel.

Plotting this cycle as a function of tip position relative to the sample results in the curves shown in Figure 5.1b. This allows us to back out the mechanical information to characterize the trout gill cells, including DMT modulus, deformation, adhesion, and dissipation. The adhesive forces between the tip and the sample are found from the minimum force in Figure 5.1b. The deformation is calculated from the difference in separation along the approach curve between the PeakForce and the point at which the force is zero. The dissipation is a measure of the viscoelasticity of the sample. We can determine the modulus value of our sample by fitting the withdraw curve (dashed green line in Figure 5.1b) using the Derjaguin-Muller-Toporov (DMT) model:[30]

$$F_L = \frac{4}{3}E^*\sqrt{R(d-d_0)^3} + F_{adh} \tag{2}$$

where F_L is the loading force, R is the tip radius, d-d_0 is the deformation depth of the sample, F_{adh} is the adhesive force, and E^* is the reduced modulus. The reduced modulus is related to the modulus of the sample in the following relationship:

$$E^* = \left[\frac{1-\nu_s^2}{E_s} + \frac{1-\nu_{tip}^2}{E_{tip}}\right]^{-1} \tag{3}$$

where ν_s and ν_{tip} are the Poisson's ratio for the sample and the tip, respectively, and E_s and E_{tip} are the modulus values of the sample and the tip, respectively. We can assume that the E_{tip} is infinite because Si_3N_4 is much harder than our cells and use the estimated Poisson's ratio of a cell to

determine the modulus value.[31] We estimated Poisson's ratio to be 0.5, the value for an incompressible material, which is consistent with other literature reports for cells.[18,32]

5.3.2 AFM imaging optimization

In order to characterize the nanomechanical properties of both live and fixed cells using PFQNM, we first needed to optimize the sample preparation and imaging parameters. Without proper attention to sample preparation and imaging conditions, shear and friction effects can cause damage to cells and lead to inaccurate height and mechanical measurements. Considerations in imaging optimization include cell confluency, choice of AFM probe, and imaging parameter optimization.

5.3.2.1 Confluency of the cells on the substrate

We examined the role of confluency on our ability to image and map the mechanical properties of trout gill cells. Confluency refers to how covered a surface is with cells. Figure 5.2 shows optical images taken using the AFM of three different cell confluences – ~75% confluency, 100% confluency, and past-confluency. *In vivo* cells form a confluent layer with one another within tissues.[33] Therefore, in order to best mimic the natural properties of cells, we wanted to work on a confluent layer. However, a 100% confluent layer (Figure 5.2b) presented challenges associated with engaging the tip to track the surface for AFM measurements to the point where we could not obtain images on a 100% confluent layer. This is likely due to the fact that engaging directly on a cell results in deformation of the cell and a large height barrier for the AFM probe.[34] Therefore, the probe was never actually engaged on a surface, but more likely just deforming the cell. However, in the case of a ~75% confluent layer, there is exposed substrate available to engage the tip on instead of an entire layer of cells. We found that a ~75% confluency layer (Figure 5.2a) allowed us to engage the tip on the hard substrate and then expand the scan size to include the cell

of interest. Samples grown to this confluency were used throughout the remainder of the work. Samples grown past confluency (Figure 5.2c) tended to ball up and not adhere to the underlying substrate, which also resulted problems in imaging, such as cells dragging on the surface causing build-up on one side of the image (Figure 5.3a) or cells getting stuck on the end of the tip (Figure 5.3b).

5.3.2.2 Choice of AFM tip

We also considered the impact of different AFM cantilever properties on our ability to image and map the mechanical properties of the cells. Consideration must be given to the spring constant of the cantilever as well as the height of the cantilever. Cells are relatively tall samples for AFM analysis and as such the potential to drag the cells across the surface is high, if the AFM probe choice is not intentional and well thought out.[34] In this work, we attempted to image cells using different probes, all from Bruker AFM Probes, whose nominal properties are listed in Table 5.1. Comparing DNP-C to MCLT-C allowed us to explore the impact of spring constant, whereas comparing DNP-C and SNL-C allowed us to explore the role of tip radius.

We found that the DNP-C probes worked best for imaging both the live and fixed gill cells. The MLCT-C probes were too soft and as such, remained bound to the adhesive cell surface. During the withdraw cycle, the probe was unable to detach from the cell surface, which caused the cells to drag along the substrate (representative images shown in Figure 5.3). The SNL-C tips were too sharp for optimized cell imaging and mechanical probing. Typically, sharper probes result in higher resolution imaging, but in the case of mechanical mapping the probe must still be able to have a large enough contact area with the cell surface to deform the sample.[35] In the case of the SNL-C probes, we found them to drag the cells on the substrate, which we hypothesize was due to them puncturing the cell rather than causing sample deformation. Ultimately, a balance between

probe stiffness and tip radius was found with the DNP-C probes, which were used throughout the work presented here.

5.3.2.3 Optimization of PFQNM imaging parameters

We also optimized both the PFQNM and traditional imaging parameters to ensure proper tracking of the cell surface and accurate mechanical measurements. This included considering the PeakForce applied to the samples, the PeakForce frequency, the PeakForce amplitude, the scan speed, and the feedback gains. These parameters were optimized for both fixed and live cells.

The PeakForce refers to the maximum amount of force applied to the samples (point 3 in Figure 5.1b). Ideally, the force will be large enough to obtain good tracking of the sample surface by the tip, but not too high as to cause sample damage. We explored a range of force values on both fixed and live cells and found that a value of 500 pN was optimal for live cells, whereas we could increase the force up to 1.5 nN on fixed cells. Higher forces on either sample caused the probe to drag the cells on the surface, whereas lower forces caused the tip to not be in good contact with the cell surface resulting in low resolution images. The fact that fixed cells could withstand more force is likely due to their increased rigidity due to the cross-linking caused by fixation.[36]

In order to obtain good tracking of the cellular surface, which can be gauged by the alignment of the trace and retrace of the line scans, we needed to optimize the PeakForce, as well as the feedback gains and scan speed. Due to the large height variation of the cell compared to the substrate (microns), the scan speed needed to be minimized to ensure that the tip could overcome these large differences.[20] We found a scan speed of 0.125 Hz worked well for both live and fixed cells. While this slow speed drastically increased the amount of time required to collect an image, it also resulted in better resolved images. The gains were optimized per cell per image and were

found to vary depending on the particular cell. We increased the gains until tracking of the surface was optimized.

Two other PFQNM parameters that were optimized were the PeakForce frequency and the PeakForce amplitude. The PeakForce frequency is the rate at which the piezo goes through the approach/withdraw cycle, whereas the PeakForce amplitude is the peak to peak height of the z piezo modulation through this cycle. Ideally, minimizing the frequency and the amplitude will reduce viscous drag on the cantilever.[37] The ideal PeakForce frequency was found to be 0.25 kHz for both fixed and live cells. While we wanted to minimize the PeakForce amplitude, we found that a value of 300 nm was necessary to allow the tip to fully withdraw from the cell surface before moving on to the next spot on the sample. Too low of an amplitude caused the tip to drag the cells.

Ultimately, the optimization of these parameters in combination with using DNP-C probes and samples grown to ~75% confluency resulted in optimized images on both fixed and live cells. Figure 5.4 shows the topographical and mechanical channels collected on a fixed cell, whereas Figure 5.5 shows these different channels for live cells. For most of the channels, good contrast is observed between the cells and the underlying substrate; however, low contrast is observed in the case of adhesion, which is likely due to the fact that working in liquid reduces the adhesive forces between the tip and sample.[38] Interestingly, what we hypothesize to be different cellular structures were also resolved, such as the actin filaments in the PeakForce Error channels of both the fixed and live cells (Figure 5.4b and Figure 5.5b, respectively) and the nucleus in the DMT modulus and dissipation channels of the fixed cells (Figure 5.4d,e). The increased resolution of these features in the fixed cells is likely due to the increased modulus values and thus higher forces we could exert on these cells.[18] Table 5.2 summarizes the ranges of values obtained for three different fixed and three different live cells. The optimization of both sample preparation and imaging conditions

presented above allowed us to explore the impact of fixation on the mechanical properties of the trout gill cells.

5.3.3 Impact of fixation on mechanical properties of trout gill cells

Fixation is a method by which biological samples are preserved from decay. Essentially the chemistry of the cell is stopped and the fine structural details of the cells and tissues are stabilized.[36] In this work we used 4% paraformaldehyde to fix the trout gill cells, which crosslinks, via a methylene bridge, the nitrogen atoms in proteins.[36] Fixed cells are easier to image by AFM[19] and improve the resolution of the AFM images;[18,31] however, fixing cells ultimately changes the cell structure, viability, and elasticity.[31] Therefore, we wanted to investigate the impact of fixation on the topography and mechanical properties of trout gill cells.

Table 5.2 shows that the fixation process significantly increased the height of the trout gill cells from 2.9 ± 0.8 to 4.6 ± 0.6 μm ($p < 0.05$). Fixation has been shown previously to either increase or decrease the height of cells. For example, an increase in height of U2-OS osteosarcoma cells was attributed to the cross-linking nature of glutaraldehyde stretching and flattening the cells on the underlying substrate,[38] whereas the opposite argument was made in the case of bacteria, where an increase in height for fixed cells was attributed to the increase in cell rigidity decreasing the likelihood of the bacteria spreading out on the surface.[39] In the case of the trout gill cells studied here, we hypothesize the increase in height with fixation is due to the fixation process increasing the rigidity of the cell and decreasing its likelihood to spread out, thus resulting in taller fixed cells as compared to live cells.

The deformation between the live and fixed cells was found to be comparable. This is somewhat surprising as we would expect the less rigid, live cells to be more easily deformed. However, we minimized the imaging force we used on both types of cells to track the surface of

the cell, but to not cause cell damage. Therefore, a comparable deformation is likely due to similar forces being applied to the cells.

The adhesion of both the fixed and live cells was low (Table 5.2). This is likely attributable to the fact that both sample types were collected in fluid. Previous work has demonstrated that working in fluid decreased the adhesive forces between the tip and the sample.[38]

We found that fixation increased the modulus value of fixed cells (maximum value observed, 116 kPa)) as compared to live cells (maximum value, 36 kPa). This is likely due to the chemical changes that fixation induces. The crosslinking of the proteins within the cell causes a more rigid cell body, which results in a stiff cell. The majority of the mechanical robustness of epithelial cells stems from the cell cortex, a thin layer of actin-myosin, which consists of cross-linked actin filaments.[40] We hypothesize it is these actin filaments that are visible in the fixed cell shown in Figure 5.4, particularly the Peak Force Error channel helps to resolve these structures (Figure 5.4b). While the range of values observed for both live and fixed cells was large (Table 5.2), our results on this epithelial cell are in agreement with the literature, which shows that fixation of different types of cells (e.g., liver endothelial cells,[18] mouse embryonic fibroblasts,[32] human epithelial cancer cells,[32] and corneal cells[41]) also results in an increase in the cell stiffness (or modulus) as compared to live cells. The large range of values found is likely due to the heterogeneity associated with cells and the various cellular components contributing to the modulus values.[18]

5.4 Conclusions and Outlook

This work presents the optimization of imaging and nanomechanical mapping (adhesion, deformation, DMT modulus, and dissipation) of trout gill cells. We demonstrated imaging and nanomechanical mapping on both fixed and live trout gill cells for the first time through the

optimization of cell confluency, AFM probe selection, and AFM imaging parameters. The optimization of PFQNM makes acquisition of mechanical properties and topography information quicker and easier than previous AFM modes. We showed that both the height and the modulus value increased for fixed cells, indicating that the chemical changes induced by fixation changes the mechanical properties of cells. Ultimately using cells grown to ~75% confluency, an AFM probe with a spring constant of 0.24 N/m and a radius of 20 nm, and low scan speeds, high amplitudes, and minimal forces resulted in the ideal imaging conditions for trout gill cells.

This work sets a precedent to consider the impact of different stressors on the mechanical properties of trout gill cells. Nanomaterials represent one emerging class of contaminants that have been shown previously to impact the mechanical properties of cells.[8-10] Future work should use the optimized parameters set forth here to investigate the impact of nanomaterials on these cells.

In considering live versus fixed cells, live cells behave more representatively of cells *in vivo* and should be used as a model system whenever possible. Furthermore, confluent cells have been shown previously to behave most like cells *in vivo*.[33] However, we found cells grown to ~75% confluency to be most idea for this work. Ultimately, developing alternative methods to conduct studies on live, confluent cells may result in the most realistic cell behavior and most accurate measurements of cell mechanics. This may include templating surfaces to have regions where cells grow to confluency near areas where the tip can engage on the surface,[34] scratching away a subsection of cells in order to engage on the substrate and then offsetting on to the remaining confluent layer, or improving our AFM imaging parameters to allow for imaging on confluent layers. Overall, PFQNM is a powerful and relatively easy method to study the cell mechanics of both fixed and live cells.

5.5 Tables

Table 5.1. Summary of the properties of the different cantilevers and tips used in this study.

Cantilever Type	Cantilever and Tip Properties			
	Height (μm)	Resonant Frequency (kHz)	Nominal Spring Constant (N/m)	Nominal Tip Radius (nm)
DNP-C	2.5 – 8.0	56	0.24	20
MLCT-C	2.5 – 8.0	7	0.01	20
SNL-C	2.5 – 8.0	56	0.24	2

[a] All listed values are nominal values and are provided by the manufacturer (Bruker AFM Probes)

Table 5.2. Summary of height, adhesion, deformation, and DMT modulus for live and fixed cells.

Sample Preparation	Mechanical Properties Measured by AFM			
	Height (μm)	**Adhesion (nN)**	**Deformation (nm)**	**DMT modulus (kPa)**
Live	2.9 ± 0.8	0.03 – 0.6	99 – 240	1.6 – 36
Fixed with 4% Paraformaldehyde	4.6 ± 0.6	0.03 – 0.2	136 – 197	21 – 116

[a] Height measurements represent the average and standard deviation of three different cells. In the case of the live cells the height values are averaged from different cells on the same sample, whereas the fixed cells are averaged across different samples. The height measurements were taken across the highest point (across the cell body) of three different cells and represents the average and standard deviation of these measurements. Adhesion, deformation, Young's modulus, and dissipation values represent a range of values found across 3 different cells.

5.6 Figures

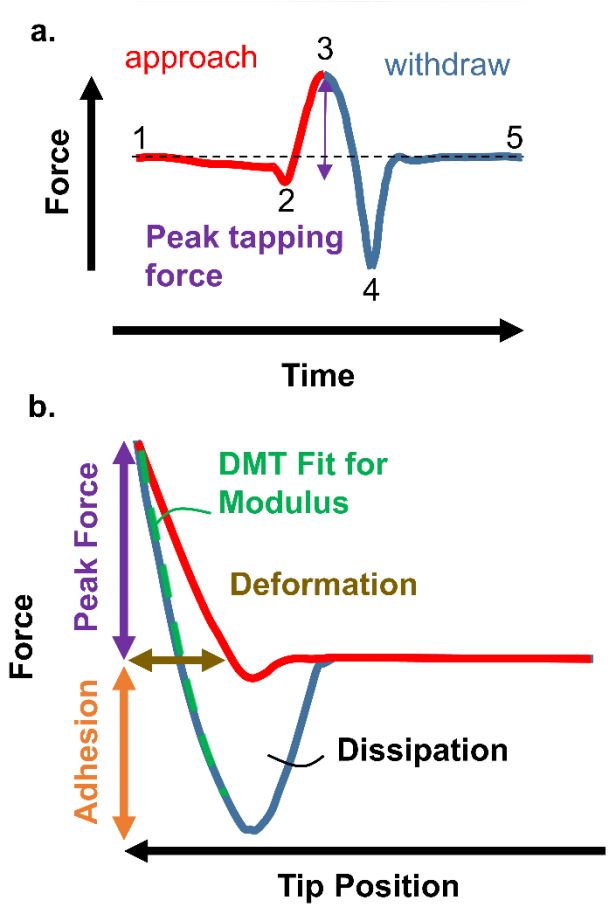

Figure 5.1. PeakForce Quantitative Nanomechanical Mapping Atomic Force Microscopy works by applying a force set point which is maintained throughout imaging. (a) a Peak tapping force is set and the tip is brought into contact with the sample (approach curve, red) until the desired force is applied at which point the tip withdraws from that spot (withdraw curve, blue). By plotting the approach and withdraw curves as a function of tip position (b), we can map the mechanical properties of the sample including, adhesion, deformation, dissipation, and modulus values for the sample in addition to topography.

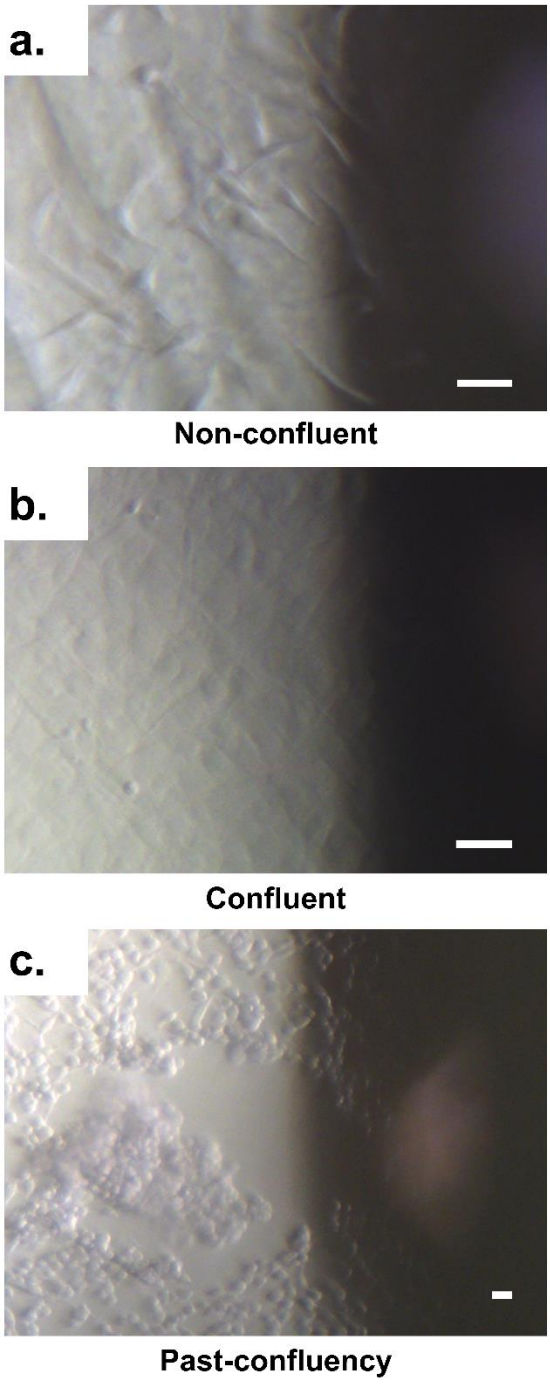

Figure 5.2. The coverage of the cells on the substrate, or their confluency, played a role in the ability to image the cells by AFM. Here the cells were grown to (a) ~75% confluency, (b) 100% confluency, and (c) past confluency. The shadow on the right hand side of the image is due to the AFM cantilever. Scale bars are ~40 μm.

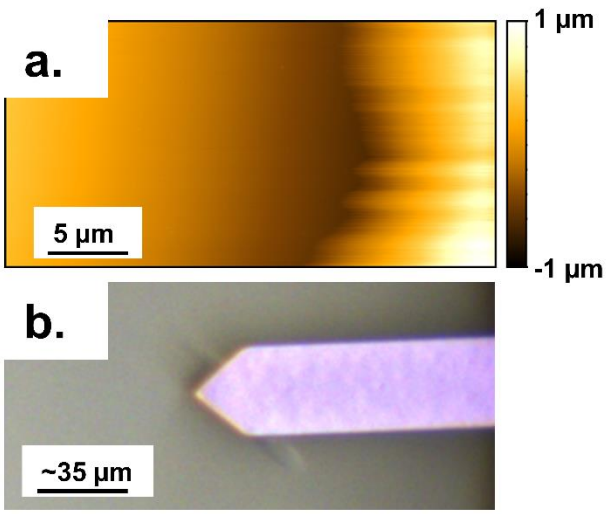

Figure 5.3.Examples where parameters for imaging were not optimized resulting in sample damage. Examples include (a) build up on one side of the image caused by the tip dragging the cells on the surface and (b) removal of the cells from the substrate via being stuck on the tip.

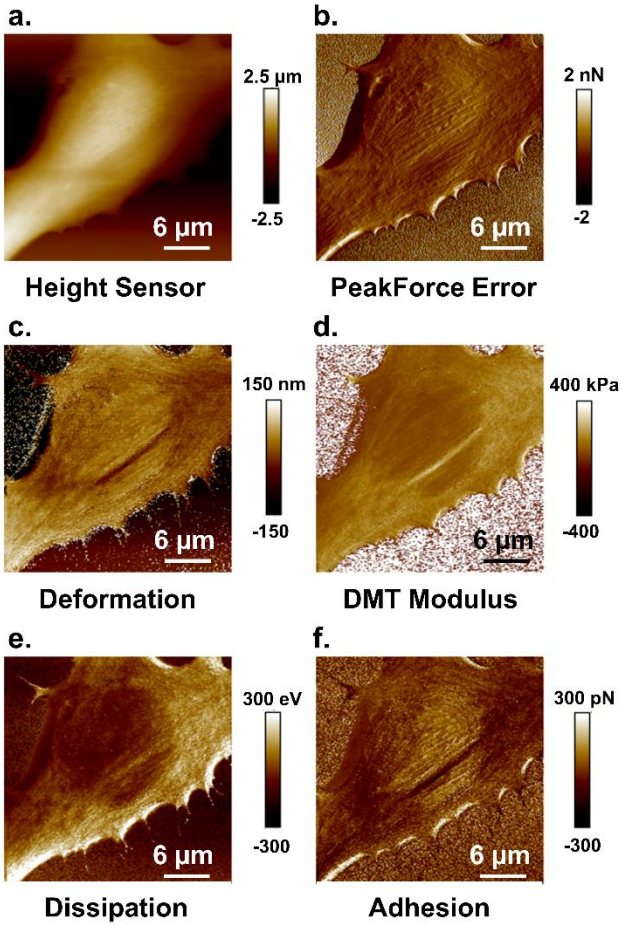

Figure 5.4. Atomic Force Microscopy images (a) topography, (b) Peak Force error, (c) deformation, (d) DMT modulus, (e) dissipation, and (f) adhesion of cells grown to ~75% confluency on a petri dish, fixed with 4% paraformaldehyde, rinsed with PBS buffer and imaged in PBS buffer at room temperature

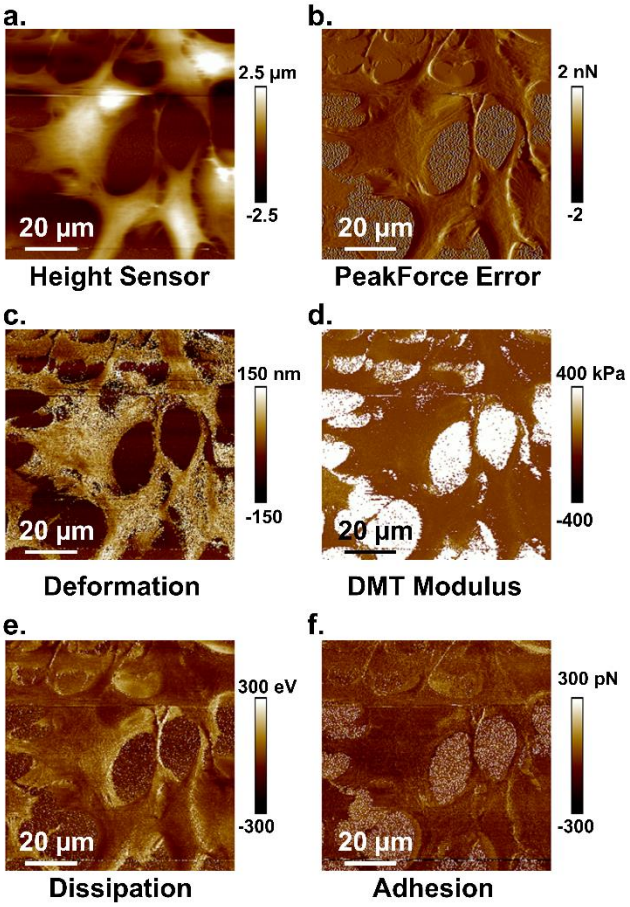

Figure 5.5. Atomic Force Microscopy images (a) topography, (b) Peak Force error, (c) deformation, (d) DMT modulus, (e) dissipation, and (f) adhesion of cells grown to ~75% confluency on a petri dish and imaged in medium at room temperature.

5.7 References

1. Fletcher, D. A.; Mullins, R. D. Cell mechanics and the cytoskeleton. *Nature,* **2010,** *463,* 485-492.

2. Alcaraz, J.; Buscemi, L.; Grabulosa, M.; Trepat, X.; Fabry, B.; Farre, R.; Navajas, D. Microheology of human lung epithelial cells measured by atomic force microscopy. *Biophys. J.,* **2003,** *84,* 2071-2079.

3. Moeendarbary, E.; Harris, A. R. Cell mechanics: Principles, practices, and prospects. *WIREs Syst. Biol. Med.,* **2014,** *6,* 371-388.

4. Rotsch, C.; Radmacher, M. Drug induced changes of cytoskeletal structure and mechanics in fibroblasts: An atomic force microscopy study. *Biophys. J.,* **2000,** *78,* 520-535.

5. Wu, H. W.; Kuhn, T.; Moy, V. T. Mechanical properties of L929 cells measured by atomic force microscopy: Effects of anticytoskeletal drugs and membrane crosslinking. *Scanning,* **1998,** *20,* 398-397.

6. Fortier, H.; Variola, F.; Wang, C.; Zou, S. AFM force indentation analysis on leukemia cells. *Anal. Methods,* **2016,** *8,* 4421-4431.

7. Zhao, X.; Zhong, Y.; Ye, T.; Wang, D.; Mao, B. Discrimination between cervical cancer cells and normal cervical cells based on longitudinal elasticity using atomic force microscopy. *Nanoscale Res. Lett.,* **2015,** *10,* 482.

8. Pernodet, N.; Fang, X.; Sun, Y.; Bakhtina, A.; Ramakrishnan, A.; Sokolov, J.; Ulman, A.; Rafailovich, M. Adverse effects of citrate/gold nanoparticles on human dermal fibroblasts. *Small,* **2006,** *2,* 766-773.

9. Pietuch, A.; Bruckner, B. R.; Schneider, D.; Tarantola, M.; Rosman, C.; Sonnichsen, C.; Janshoff, A. Mechanical properties of MDCK II cells exposed to gold nanorods. *Beilstein J. Nanotechnol.,* **2015,** *6,* 223-231.

10. Zhang, X.; Zhang, Y.; Zheng, Y.; Wang, B. Mechanical characteristics of human red blood cell membrane change due to C_{60} nanoparticle infiltration. *Phys. Chem. Chem. Phys.,* **2013,** *15,* 2473-2481.

11. Binnig, G.; Quate, C. F.; Gerber, C. Atomic force microscope. *Phys. Rev. Lett.,* **1986,** *56,* 930-933.

12. Engel, A.; Muller, D. J. Observing single biomolecules at work with the atomic force microscope. *Nat. Struct. Biol.,* **2000,** *7,* 715-718.

13. Hansma, H. G.; Sinsheimer, R. L.; Li, M.-Q.; Hansma, P. K. Atomic force microscopy of single- and double-stranded DNA. *Nucleic Acids Res.,* **1992,** *20,* 3585.

14. Lyubchenko, Y. L. DNA structure and dynamics. *Cell Biochem. Biophys.*, **2004,** *41*, 75-98.

15. Mingeot-Leclercq, M. P.; Deleu, M.; Brasseur, R.; Dufrene, Y. F. Atomic force microscopy of supported lipid bilayers. *Nat. Protoc.,* **2008,** *3*, 1654-1659.

16. Dufrene, Y. F.; Lee, G. U. Advances in the characterization of supported lipid films with the atomic force microscope. *Biochim. Biophys. Acta,* **2000,** *1509*, 14-41.

17. Muller, D. J.; Janovjak, H.; Lehto, T.; Kuerschner, L.; Anderson, K. Observing structue, function and assembly of single proteins by AFM. *Prog. Biophys. Mol. Biol.,* **2002,** *79*, 1-43.

18. Braet, F.; Rotsch, C.; Wisse, E.; Radmacher, M. Comparison of fixed and living liver endothelial cells by atomic force microscopy. *Appl. Phys. A,* **1998,** *66,* S575-S578.

19. Sinniah, K.; Paauw, J.; Ubels, J. Investigating live and fixed epithelial and fibroblast cells by atomic force microscopy. *Curr. Eye Res.,* **2002,** *25*, 61-68.

20. Henderson, E. Imaging of living cells by atomic force microscopy. *Prog. Surf. Sci.,* **1994,** *46*, 39-60.

21. Pittenger, B.; Erina, N.; Su, C. *Quantitative mechanical property mapping at the nanoscale with peakforce QNM*; Bruker: 2010; 1-12.

22. Alsteens, D.; Muller, D. J.; Dufrene, Y. F. Multiparametric atomic force microscopy imaging of biomolecular and cellular systems. *Acc. Chem. Res.,* **2017,** *50*, 924-931.

23. Tanneberger, K.; Knobel, M.; Busser, F. J.; Sinnige, T. L.; Hermens, J. L.; Schirmer, K. Predicting fish acute toxicity using a fish gill cell line-based toxicity assay. *Environ. Sci. Technol.,* **2013,** *47*, 1110-1119.

24. Yue, Y.; Behra, R.; Sigg, L.; Suter, M. J. F.; Pillai, S.; Schirmer, K. Silver nanoparticle–protein interactions in intact rainbow trout gill cells. *Environ. Sci.: Nano,* **2016,** *3*, 1174-1185.

25. Butt, H.-J.; Cappella, B.; Kappl, M. Force measurements with the atomic force microscope: Technique, interpretation and applications. *Surf. Sci. Rep.,* **2005,** *59*, 1-152.

26. Slattery, A. D.; Blanch, A. J.; Quinton, J. S.; Gibson, C. T. Accurate measurement of atomic force microscope cantilever deflection excluding tip-surface contact with application to force calibration. *Ultramicroscopy,* **2013,** *131*, 46-55.

27. Hutter, J. L.; Bechhoefer, J. Calibration of atomic-force microscope tips. *Rev. Sci. Instrum.,* **1993,** *64*, 1868-1873.

28. Butt, H. J.; Jaschke, M. Calculation of thermal noise in atomic force microscopy. *Nanotechnology,* **1995,** *6*, 1-7.

29. Ohler, B. *Practical advice on determination of cantilever spring constants*; Veeco: 2007.

30. Derjaguin, B. V.; Muller, V. M.; Toporov, Y. P. Effect of contact deformations on the adhesion of particles. *J. Colloid Interface Sci.,* **1975,** *53,* 314-326.

31. Kuznetsova, T. G.; Starodubtseva, M. N.; Yegorenkov, N. I.; Chizhik, S. A.; Zhdanov, R. I. Atomic force microscopy probing of cell elasticity. *Micron,* **2007,** *38,* 824-833.

32. Codan, B.; Martinelli, V.; Mestroni, L.; Sbaizero, O. Atomic force microscopy of 3T3 and SW-13 cell lines: An investigation of cell elasticity changes due to fixation. *Mater. Sci. Eng. C Mater. Biol. Appl.,* **2013,** *33,* 3303-3308.

33. Efremov, Y. M.; Dokrunova, A. A.; Bagrov, D. V.; Kudryashova, K. S.; Sokolova, O. S.; Shaitan, K. V. The effects of confluency on cell mechanical properties. *J. Biomech.,* **2013,** *46,* 1081-1087.

34. Morris, V. J.; Kirby, A. R.; Gunning, A. P., *Atomic force microscopy for biologists*. Imperial College Press: 2009.

35. Gavara, N. A beginner's guide to atomic force microscopy probing for cell mechanics. *Microsc. Res. Tech.,* **2017,** *80,* 75-84.

36. Kiernan, J. A., Formaldehyde, formalin, paraformaldehyde and glutaraldehyde: What they are and what they do. *Microscopy Today* 2000, pp 8-12.

37. Bruker Nano Surfaces Division. *Toward quantitative nanomechanical measurements on live cells with peakforce QNM*; Application Note #141; 2013.

38. Berquand, A.; Roduit, C.; Kasas, S.; Holloschi, A.; Ponce, L.; Hafner, M., Atomic force microscopy imaging of living cells. *Microscopy Today* 2010, pp 8-14.

39. Liu, B. Y.; Zhang, G. M.; Li, X. L.; Chen, H. Effect of glutaraldehyde fixation on bacterial cells observed by atomic force microscopy. *Scanning,* **2012,** *34,* 6-11.

40. Bruckner, B. R.; Janshoff, A. Elastic properties of epithelial cells probed by atomic force microscopy. *Biochim. Biophys. Acta,* **2015,** *1853,* 3075-3082.

41. Shibata-Seki, T.; Tajima, K.; Takahashi, H.; Seki, H.; Masai, J.; Goto, H.; Kobatake, E.; Akaike, T.; Itoh, N. AFM characterization of chemically treated corneal cells. *Anal. Bioanal. Chem.,* **2015,** *407,* 2631-2635.

Chapter 6: Conclusions and Future Directions

As the use of nanomaterials continues to rise, a need exists to understand the interactions that occur between released nanomaterials and organisms at a molecular level. This problem is difficult and requires input from scientists from all fields. However, utilizing model systems and developing *in situ* analytical approaches to study these interactions will undoubtedly help to simplify these complex systems. The work presented here focuses on the implementation of *in situ* analytical methods to characterize supported lipid bilayers, intentionally designed to best model the cellular membranes of different types of organisms, and their interactions with nanomaterials, as well as the mechanical characteristics of trout gill cells.

First, we examined the impact of natural organic matter (NOM) on the interactions of poly(allylamine hydrochloride) polymer-wrapped diamond nanoparticles (DNPs) with supported lipid bilayers and the Gram-negative bacterium, *Shewanella oneidensis* MR-1. We found NOM impacts the hydrodynamic and electrokinetic properties of the DNPs in a concentration dependent manner. These changes to the physical properties of the DNPs altered subsequent interactions with the model membrane systems as well as to *S. oneidensis*. The inclusion of both lipid bilayers and *S. oneidensis* increased the impact of this work by demonstrating that experiments conducted on model bilayers may be extendable to full organism studies. Ultimately, for concentration ratios of NOM-to-DNP expected to be found in the environment, it is likely that NOM will cause a reversal of charge and minimize the biological impact of the DNPs.

While positively charged diamond nanomaterials attached to model membranes, positively charged quantum dots caused structural rearrangement of supported lipid bilayers. Through the use of complementary *in situ* analytical techniques we found that quantum dots deposited on the bilayers and caused the lipids to rearrange around the particles. Furthermore, the quantum dots

caused the disappearance of phase-segregated domains (composed of sphingomyelin and cholesterol) likely through the removal of the cholesterol from these domains. This study highlighted the importance of using complementary, *in situ* approaches to understand interactions that occur at the cellular membrane.

Nanoparticle interactions with supported lipid membranes are complex and the mechanisms of these interactions are difficult to discern. However, through the use of *in situ* analytical tools this work has made significant contributions to understanding two specific interactions. While aspects of this work are likely transferable to other positively charged nanomaterials, future work is needed to examine the influence of surface charge, charge density, capping agent, and core material on the interactions of nanomaterials with bilayers and organisms. In particular, studying these interactions in both the presence and absence of NOM is crucial as NOM is found ubiquitously in the environment and, as we have shown, can play a critical role in the impact of nanomaterials on organisms. Varying the water chemistry (e.g., inclusion of divalent cations, changing the source of the NOM used) could also be explored to generalize these results to more complex settings.

Significant efforts were made to characterize supported lipid bilayers. We demonstrate that the substrate plays a significant role in the distribution of biomolecules in supported lipid bilayers. On mica substrates, cholesterol and sphingomyelin form large phase-segregated domains, whereas on ultraflat SiO_2 and glass the domains are much smaller. Consideration must be paid to substrate choice in extending studies across various analytical techniques.

Finally, PeakForce quantitative nanomechanical mapping atomic force microscopy was optimized and used to characterize the topography, modulus, deformation, adhesion, and dissipation of trout gill cells. We found that fixation causes an increase in modulus value and

height of the cells. This works sets the groundwork to consider the impact of nanomaterials and other stressors on the mechanical properties of cells. There is ample opportunity to make great contributions to the field using the knowledge gained in these studies. Coupling AFM with fluorescence microscopy will allow us to directly correlate cellular structures with mechanical changes and/or correlate the location of nanomaterials to different parts of the cell. Furthermore, tip functionalization may be used to directly probe cells or model membranes with nanomaterials or different ligands to study their adhesion to the cellular membrane.

Appendix

A.2. Supporting Information for Chapter 2: Natural Organic Matter Concentration Impacts the Interaction of Functionalized Diamond Nanoparticles with Model and Actual Bacterial Membranes

A2.1 Supplemental Materials and Methods

A2.1.1 Chemicals

Suwannee River natural organic matter was purchased from the International Humic Substances Society (1R101N, St. Paul, MN). Poly(allylamine hydrochloride) (PAH, 15kDa), lipopolysaccharide (LPS) purified from *Salmonella enterica* serotype minnesota (smooth) and *Salmonella enterica* serotype minnesota Re595 mutant (rough) were procured from Sigma-Aldrich (St. Louis, MO). Smooth LPS was dissolved in 8:2 (v/v) ultrapure H_2O:methanol, whereas rough LPS was dissolved in chloroform. We obtained 1-palmitoyl-2-oleoyl-*sn*-glycero-3-phosphocholine (POPC) in chloroform from Avanti Polar Lipids (Alabaster, AL). Buffers were prepared with 0.002 M 4-(2-hydroxyethyl)-1-1piperazineethanesulfonic acid (HEPES, Fisher Scientific). The ionic strength was controlled with the addition of sodium chloride, and pH was adjusted to 7.4 with NaOH. Solutions were filtered through a 0.22 μm filter (Millipore, Billerica, MA).

A2.1.2 Lipopolysaccharide-phospholipid vesicles preparation and characterization

Solutions of POPC and LPS were mixed to the desired ratios[1] in glass vials, the solvent was evaporated off using nitrogen gas, and the remaining solvent was removed under vacuum for at least 2 h. The dried lipid/LPS solids were rehydrated in 0.001 M NaCl buffered to pH 7.4 with 0.002 M HEPES and vortexed and sonicated to mix. After rehydration, the solution was subjected to three cycles of freezing with liquid nitrogen and thawing by sonication prior to

extrusion through a 50 nm polycarbonate membrane filter (Whatman) 15 times using an Avanti 610000 extruder kit. Vesicle electrophoretic mobilities and diffusion coefficients were determined in 0.002 M HEPES, 0.001 M NaCl, pH 7.4 using laser Doppler microelectrophoresis and dynamic light scattering. These data are shown in Figure A2.3. These vesicles were used to form supported lipid bilayers as described previously.[1] An example QCM-D frequency trace for bilayer formation is depicted in Figure A2.4.

A2.1.3 Attachment of PAH-DNP in the absence and presence of NOM to SiO_2-coated QCM-D sensor

We determined initial rates of attachment to SiO_2 under the same conductions used for the bilayers. QCM-D sensors were cleaned as described in the main text. The sensor was equilibrated with 0.025 M NaCl buffered to pH 7.4 with 0.002 M HEPES until a stable baseline was achieved. PAH-DNP in the absence or presence of NOM, or NOM alone in the same electrolyte solution was flowed over the sensor surface for 20 min. The sensor was then rinsed again with buffer for at least 10 min to obtain a stable baseline. Results from these experiments are presented in Tables A2.1-A2.8. Trends in attachment to SiO_2 were similar to those observed for the POPC bilayer. However, the presence of the bilayer significantly increased PAH-DNP attachment in the absence of NOM and in the 1.33 $mg_{oc} \cdot mg_{PAH\text{-}DNP}^{-1}$ NOM:DNP concentration ratio.

A2.1.4 Bilayers equilibrated in PAH polymer prior to introduction of DNPs

We also examined whether the observed trends in attachment could be attributed to any PAH polymer in the nanoparticle suspensions. In the case of most functionalized nanoparticles, unbound capping agent remains in nanoparticle suspension after the functionalization steps.[2] The amount of unbound PAH polymer was determined using fluorescamine, a dye that binds to

primary amines,[3-4] following a recently published procedure[5] using a calibration curve prepared from three PAH polymer concentrations. To obtain the amount of unbound PAH polymer remaining in the PAH-DNP, the stock suspension was diluted with ultrapure water, and the diluted suspensions were centrifuged at 66,000*g* for 45 min at 4 °C to pellet the nanoparticles. A PAH polymer solution of 441.1 $mg \cdot L^{-1}$ was also centrifuged together with the sample as a control. After centrifugation, grey pellets of NDs were observed. Supernatants were collected, and aliquots of the supernatants were concentrated using a Savant SpeedVac Concentrator. We determined that ~4.7 $mg \cdot L^{-1}$ of free PAH polymer remained in solution for the 1 nM PAH-DNP suspensions used in this study.

To examine the possible effect of free PAH polymer with the bilayers and SiO_2 surfaces used in experiments with PAH-DNPs, we first equilibrated the LPS-bilayers with 4.7 $mg \cdot L^{-1}$ free PAH polymer prior to the introduction of PAH-DNP in the absence or presence of NOM or of NOM alone. We found that the free PAH polymer bound to all bilayers studied (Table A2.9). We then introduced PAH-DNP in the absence or presence of NOM or of NOM alone to the bilayers and surfaces that had been equilibrated with PAH polymer. The overall trends of attachment remain the same as when bilayers were not pre-exposed to PAH polymer, although some differences in mass did occur due to the presence of the free PAH polymer (Table A2.9).

A2.2 Supplemental Results and Discussion

A2.2.1 Mass transport-limited attachment rate constants

The attachment efficiencies for PAH-DNP attachment to the model membranes are all are close to unity (Table A2.2) suggesting mass transport-limited deposition in the absence of NOM and in the presence of 5 mg_{oc}/L NOM. We analyzed the expected transport of the particles and their aggregates to the bilayer surface using the modified Lévêque solution for mass transport-limited

attachment: $\langle k_a \rangle = D_c^{2/3} Q^{1/3} \langle n \rangle$, where $\langle k_a \rangle$ is the spatially averaged mass transport-limited attachment rate constant, D_c is the diffusion coefficient, Q is the volumetric flow rate and $\langle n \rangle$ is a geometric factor specific to the QCM-D flow chamber.[6] Using diffusion coefficients corresponding to the number average hydrodynamic diameters, this analysis indicates that in the presence of 5 mg_{oc}/L NOM, $\langle k_a \rangle$ is smaller by a factor of 0.56 ± 0.15 relative to the case without NOM.

The initial rates of attachment are comparable for the 0 and 5 mg_{oc}/L NOM cases (Figure 2.2a, Table A2.1). The initial rate of attachment is given as $r_d = \langle k_a \rangle C$, where C is the mass concentration of particles or aggregates. The attachment rates being equivalent in the absence and presence of 5 mg_{oc}/L NOM implies that on average the *effective* mass of the aggregates formed in the presence of 5 mg_{oc}/L NOM (mass of PAH-DNPs, NOM, and water) attaching to the model membrane during the initial attachment period is approximately twice that of the individual PAH-DNPs.

A2.3 Supplemental Tables

Table A2.1. Initial rates of (NOM/)PAH-DNP or NOM deposition to the POPC bilayers containing the indicated amount of rough or smooth lipopolysaccharides or to silica.[a]

			initial attachment rate, r_d ($ng \cdot cm^{-2} \cdot s^{-1}$)				
[PAH-DNP] (nM)	**[NOM] ($mg_{OC} \cdot L^{-1}$)**	**[NOM]:[DNP] ($mg_{OC} \cdot mg_{PAH\text{-}DNP}^{-1}$)**	**POPC**	**0.46 mol% sLPS**	**0.46 mol% rLPS**	**6.4 mol% rLPS**	**SiO_2**
1	0	0	2.0 ± 0.4	1.8 ± 0.4	1.8 ± 0.2	1.1 ± 0.2	1.6 ± 0.2
1	5	1.33	2.5 ± 0.5	1.3 ± 0.4	2.2 ± 0.2	2.5 ± 0.2****	1.4 ± 0.2
1	30	8	0.09 ± 0.08****	0.10 ± 0.02****	0.12 ± 0.09****	–***	–****
—	5	—	0.12 ± 0.02****	–****	0.20 ± 0.03***	–****	–****
—	30	—	0.11 ± 0.03****	0.11 ± 0.13****	0.20 ± 0.03***	–****	–****

[a] Attachment experiments were conducted in 0.025 M NaCl buffered to pH 7.4 with 0.002 M HEPES at 25 °C. Initial rates are for the first 30 s of PAH-DNP or NOM attachment to the indicated surface. Values are means ± standard deviations of at least triplicate experiments. Abbreviations: POPC, 1-palmitoyl-2-oleoyl-*sn*-glycero-3-phosphocholine; rLPS, rough lipopolysaccharide; sLPS, smooth lipopolysaccharide. Significance of differences relative to the rate of deposition of PAH-DNP in the absence of NOM for each surface: ***, $p < 0.001$; ****, $p < 0.0001$.

Table A2.2. Attachment efficiencies (α_D) for (NOM/)PAH-DNP attachment to the POPC bilayers containing the indicated amount of rough or smooth lipopolysaccharides.[a]

[PAH-DNP] (nM)	[NOM] ($mg_{OC} \cdot L^{-1}$)	[NOM]:[DNP] ($mg_{OC} \cdot mg_{PAH\text{-}DNP}^{-1}$)	attachment efficiencies, α_D			
			POPC	0.46 mol% sLPS	0.46 mol% rLPS	6.4 mol% rLPS
1	0	0	1.3 ± 0.3	1.1 ± 0.3	1.1 ± 0.2	0.7 ± 0.2
1	5	1.33	1.8 ± 0.4	0.9 ± 0.3	1.6 ± 0.3	1.8 ± 0.3*

[a] Attachment efficiencies were calculated as the ratio of the initial attachment rate to the indicated bilayer to the attachment rate to SiO_2 ($r_d/r_{d,SiO2}$). Attachment experiments were conducted in 0.025 M NaCl buffered to pH 7.4 with 0.002 M HEPES at 25 °C. Initial rates are for the first 30 s of PAH-DNP or NOM attachment to the indicated surface ratioed to the initial attachment rate to SiO_2. Values are means ± uncertainty of at least triplicate experiments. Abbreviations: POPC, 1-palmitoyl-2-oleoyl-*sn*-glycero-3-phosphocholine; rLPS, rough lipopolysaccharide; sLPS, smooth lipopolysaccharide. Significance of differences relative to the attachment efficiency of PAH-DNP in the absence of NOM for each surface: *, $p < 0.05$.

Table A2.3. Initial change in dissipation for (NOM/)PAH-DNP or NOM deposition to the POPC bilayers containing the indicated amount of rough or smooth lipopolysaccharides or to silica.[a]

			change in dissipation, ΔD_5 ($\times 10^{-6}$)				
[PAH-DNP] (nM)	**[NOM] ($mg_{oc} \cdot L^{-1}$)**	**[NOM]:[DNP] ($mg_{oc} \cdot mg_{PAH\text{-}DNP}^{-1}$)**	**POPC**	**0.46 mol% sLPS**	**0.46 mol% rLPS**	**6.4 mol% rLPS**	**SiO_2**
1	0	0	0.3 ± 0.1	0.2 ± 0.09	0.3 ± 0.2	0.06 ± 0.06	0.2 ± 0.06
1	5	1.33	0.4 ± 0.09	0.3 ± 0.2	0.5 ± 0.08	0.6 ± 0.2	0.6 ± 0.04
1	30	8	0.1 ± 0.2	0.0 ± 0.1	0.0 ± 0.1	—	—
—	5	—	0.01 ± 0.06	—	0.04 ± 0.08	—	—
—	30	—	-0.3 ± 0.4	0.1 ± 0.2	0.01 ± 0.09	—	—

[a] Attachment experiments were conducted in 0.025 M NaCl buffered to pH 7.4 with 0.002 M HEPES at 25 °C. Initial rates of dissipation change are for the first 30 s of PAH-DNP or NOM attachment to the indicated surface. Values are means ± standard deviations of at least triplicate experiments. Abbreviations: POPC, 1-palmitoyl-2-oleoyl-*sn*-glycero-3-phosphocholine; rLPS, rough lipopolysaccharide; sLPS, smooth lipopolysaccharide.

Table A2.4. Ratio of initial change in dissipation to initial change in frequency for (NOM/)PAH-DNP or NOM deposition to the POPC bilayers containing the indicated amount of rough or smooth lipopolysaccharides or to silica.[a]

			$-\Delta D_5/(\Delta f_5/5)$ ($\times 10^{-6}$)				
[PAH-DNP] (nM)	**[NOM] ($mg_{OC} \cdot L^{-1}$)**	**[NOM]:[DNP] ($mg_{OC} \cdot mg_{PAH\text{-}DNP}^{-1}$)**	**POPC**	**0.46 mol% sLPS**	**0.46 mol% rLPS**	**6.4 mol% rLPS**	**SiO_2**
1	0	0	0.1 ± 0.03	0.06 ± 0.04	0.1 ± 0.05	0.05 ± 0.05	0.07 ± 0.02
1	5	1.33	0.1 ± 0.07	0.1 ± 0.1	0.2 ± 0.03	0.2 ± 0.03	0.3 ± 0.03
1	30	8	–0.1 ± 0.7	0.3 ± 0.8	0.0 ± 1.3	—	—
—	5	—	–8 ± 16	—	0.6 ± 1.3	—	—
—	30	—	–1.2 ± 1.2	–0.3 ± 0.6	0.2 ± 0.6	—	—

[a] Attachment experiments were conducted in 0.025 M NaCl buffered to pH 7.4 with 0.002 M HEPES at 25 °C. Initial rates of dissipation and frequency change are for the first 30 s of PAH-DNP or NOM attachment to the indicated surface. Values are means ± standard deviations of at least triplicate experiments. Abbreviations: POPC, 1-palmitoyl-2-oleoyl-*sn*-glycero-3-phosphocholine; rLPS, rough lipopolysaccharide; sLPS, smooth lipopolysaccharide.

Table A2.5. Change in frequency measured by QCM-D after 20 min attachment of (NOM/)PAH-DNP or NOM to the POPC bilayers containing the indicated amount of rough or smooth lipopolysaccharides or to silica.[a]

			change in frequency, $\Delta f_5/5$ (Hz)				
[PAH-DNP] (nM)	**[NOM] ($mg_{OC} \cdot L^{-1}$)**	**[NOM]:[DNP] ($mg_{OC} \cdot mg_{PAH\text{-}DNP}^{-1}$)**	**POPC**	**0.46 mol% sLPS**	**0.46 mol% rLPS**	**6.4 mol% rLPS**	**SiO_2**
1	0	0	–26 ± 1.9	–22.0 ± 3.1	–25 ± 2.0	–5 ± 1.9	–7.1 ± 0.8
1	5	1.33	–120 ± 12	–90 ± 16	–110 ± 19	–120 ± 10	–78 ± 7.9
1	30	8	–6.5 ± 0.7	–3 ± 1.2	–4 ± 1.1	—	—
—	5	—	–1.4 ± 0.7	—	–2 ± 1.3	—	—
—	30	—	–4.5 ± 1.1	–1.7 ± 0.3	–3.9 ± 0.3	—	—

[a] Attachment experiments were conducted in 0.025 M NaCl buffered to pH 7.4 with 0.002 M HEPES at 25 °C. All data are for the 5th harmonic after 20 min of attachment. Values are means ± standard deviations of at least triplicate experiments. Abbreviations: POPC, 1-palmitoyl-2-oleoyl-*sn*-glycero-3-phosphocholine; rLPS, rough lipopolysaccharide; sLPS, smooth lipopolysaccharide.

Table A2.6. Change in dissipation measured by QCM-D after 20 min attachment of (NOM/)PAH-DNP or NOM to the POPC bilayers containing the indicated amount of rough or smooth lipopolysaccharides or to silica.[a]

			change in dissipation, ΔD_5 ($\times 10^{-6}$)				
[PAH-DNP] (nM)	**[NOM] ($mg_{OC} \cdot L^{-1}$)**	**[NOM]:[DNP] ($mg_{OC} \cdot mg_{PAH\text{-}DNP}^{-1}$)**	**POPC**	**0.46 mol% sLPS**	**0.46 mol% rLPS**	**6.4 mol% rLPS**	**SiO_2**
1	0	0	2.3 ± 0.1	1.7 ± 0.2	2.6 ± 0.2	0.4 ± 0.3	0.6 ± 0.04
1	5	1.33	15 ± 4.1	15 ± 1.7	21 ± 2.8	22 ± 2.2	22 ± 1.4
1	30	8	0.9 ± 0.2	0.2 ± 0.5	0.6 ± 0.05	—	—
—	5	—	0.2 ± 0.1	—	0.3 ± 0.04	—	—
—	30	—	0.6 ± 0.2	0.2 ± 0.1	0.6 ± 0.5	—	—

[a] Attachment experiments were conducted in 0.025 M NaCl buffered to pH 7.4 with 0.002 M HEPES at 25 °C. All data are for the 5th harmonic after 20 min of attachment. Values are means ± standard deviations of at least triplicate experiments. Abbreviations: POPC, 1-palmitoyl-2-oleoyl-*sn*-glycero-3-phosphocholine; rLPS, rough lipopolysaccharide; sLPS, smooth lipopolysaccharide.

Table A2.7. Ratio of change in dissipation to change in frequency measured by QCM-D after 20 min attachment of (NOM/)PAH-DNP or NOM to the POPC bilayers containing the indicated amount of rough or smooth lipopolysaccharides or to silica.[a]

			$-\Delta D_5/(\Delta f_5/5)$ ($\times 10^{-7}$)				
[PAH-DNP] (nM)	**[NOM] ($mg_{OC} \cdot L^{-1}$)**	**[NOM]:[DNP] ($mg_{OC} \cdot mg_{PAH-DNP}^{-1}$)**	**POPC**	**0.46 mol% sLPS**	**0.46 mol% rLPS**	**6.4 mol% rLPS**	**SiO_2**
1	0	0	0.9 ± 0.01	0.8 ± 0.02	1.0 ± 0.04	0.8 ± 0.3	0.9 ± 0.1
1	5	1.33	1.3 ± 0.2	1.7 ± 0.4	1.9 ± 0.4	1.8 ± 0.1	2.8 ± 0.3
1	30	8	1.4 ± 0.3	0.8 ± 2.0	1.6 ± 0.3	—	—
—	5	—	2.2 ± 1.6	—	3.1 ± 3.2	—	—
—	30	—	1.3 ± 0.2	0.9 ± 0.6	1.4 ± 0.07	—	—

[a] Attachment experiments were conducted in 0.025 M NaCl buffered to pH 7.4 with 0.002 M HEPES at 25 °C. All data are for the 5th harmonic after 20 min of attachment. Values are means ± standard deviations of at least triplicate experiments. Abbreviations: POPC, 1-palmitoyl-2-oleoyl-*sn*-glycero-3-phosphocholine; rLPS, rough lipopolysaccharide; sLPS, smooth lipopolysaccharide.

Table A2.8. Acoustic surface mass densities measured by QCM-D after 20 min attachment of (NOM/)PAH-DNP or NOM to the POPC bilayers containing the indicated amount of rough or smooth lipopolysaccharides or to silica [a]

			Acoustic surface mass density, $\Delta\Gamma_{QCM-D}$ ($ng \cdot cm^{-2}$)				
[PAH-DNP] (nM)	**[NOM] ($mg_{OC} \cdot L^{-1}$)**	**[NOM]:[DNP] ($mg_{OC} \cdot mg_{PAH-DNP}^{-1}$)**	**POPC**	**0.46 mol% sLPS**	**0.46 mol% rLPS**	**6.4 mol% rLPS**	**SiO_2**
1	0	0	470 ± 33	400 ± 55	460 ± 36	90 ± 34	130 ± 14
1	5	1.33	2110 ± 210****	1600 ± 290****	2000 ± 250****	2100 ± 190****	1400 ± 140****
1	30	8	120 ± 12****	50 ± 22****	70 ± 19****	—****	—
—	5	—	25 ± 13***	—*	30 ± 24**	—****	—
—	30	—	80 ± 21*	30 ± 6*	70 ± 6**	—****	—

[a] Attachment experiments were conducted in 0.025 M NaCl buffered to pH 7.4 with 0.002 M HEPES at 25 °C. All data are for the 5th harmonic after 20 min of attachment. Values are means ± standard deviations of at least triplicate experiments. Abbreviations: POPC, 1-palmitoyl-2-oleoyl-*sn*-glycero-3-phosphocholine; rLPS, rough lipopolysaccharide; sLPS, smooth lipopolysaccharide. Significance of differences relative to the acoustic surface mass density of PAH-DNP in the absence of NOM for each surface: *, $p < 0.05$; **, $p < 0.01$; ***, $p < 0.001$; ****, $p < 0.0001$.

Table A2.9. Acoustic surface mass densities measured by QCM-D after 20 min attachment of free PAH polymer and (NOM/)PAH-DNP or NOM to the POPC bilayers containing the indicated amount of rough or smooth lipopolysaccharides after being pre-exposed to PAH polymer.[a]

[PAH-DNP] (nM)	[NOM] ($mg_{OC} \cdot L^{-1}$)	[NOM]:[DNP] ($mg_{OC} \cdot mg_{PAH-DNP}^{-1}$)	[PAH] polymer ($mg \cdot L^{-1}$)	Acoustic surface mass density, $\Delta\Gamma_{QCM-D}$ ($ng \cdot cm^{-2}$)			
				POPC	0.46 mol% sLPS	0.46 mol% rLPS	6.4 mol% rLPS
—	—	—	4.7	54 ± 4	80 ± 10	80 ± 22	40 ± 15****
1	0	0	—	500 ± 30	410 ± 97	260 ± 50	—
1	5	1.33	—	1570 ± 86****	1300 ± 480	1200 ± 311****	90 ± 18
1	30	8	—	128 ± 7	120 ± 13	150 ± 18	150 ± 18
—	5	—	—	80 ± 25	76 ± 9	80 ± 18	130 ± 13
—	30	—	—	133 ± 2	149 ± 7	180 ± 14	144 ± 7

[a] Attachment experiments were conducted in 0.025 M NaCl buffered to pH 7.4 with 0.002 M HEPES at 25 °C. The bilayers were formed as previously described and 4.7 $mg \cdot L^{-1}$free PAH polymer was flowed over the bilayers prior to the exposure to PAH-DNPs, NOM, or PAH-DNP and NOM. All data are for the 5th harmonic after 20 min of attachment. Values are means ± standard deviations of at least triplicate experiments. Significance of differences relative to the acoustic surface mass density of PAH-DNP without prior exposure to PAH polymer (Table S5): ****, p <0.0001. Abbreviations: POPC, 1-palmitoyl-2-oleoyl-*sn*-glycero-3-phosphocholine; rLPS, rough lipopolysaccharide; sLPS, smooth lipopolysaccharide; PAH, poly(allylamine hydrochloride).

A2.4 Supplemental Figures

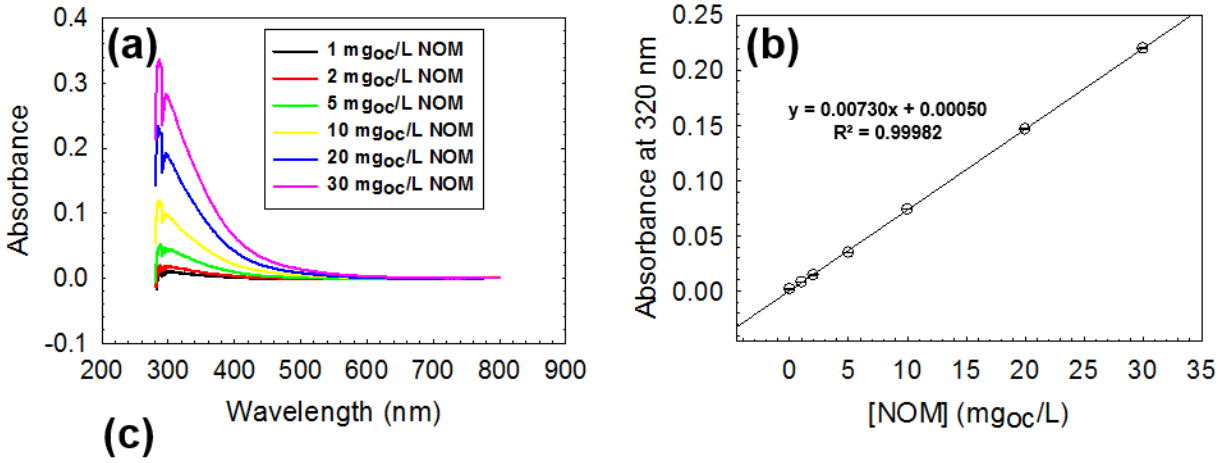

(c)

[PAH-DNP] (nM)	[NOM] ($mg_{OC} \cdot L^{-1}$)	NOM-to-DNP ratio ($mg_{OC} \cdot mg_{PAH\text{-}DNP}^{-1}$)	Absorbance at 320 nm	[NOM] in supernatant ($mg_{OC} \cdot L^{-1}$)
1	10	2.67	0.011 ± 0.001	1.7 ± 0.1
1	30	8	0.16 ± 0.0004	21.8 ± 0.1

Figure A2.1. (a) Absorbance of chromophoric NOM between 280 and 800 nm and (b) absorbance of chromophoric SRNOM at 320 nm as a function of NOM concentration. Error bars represent one standard deviation of three measurements and fall within the data points depicted. The line of best fit of this plot was used to quantify (c) the amount of NOM remaining in the supernatant of the 2.67 and 8 $mg_{OC} \cdot mg_{PAH\text{-}DNP}^{-1}$ samples. Standard deviations are for three measurements. The limit of detection for this study was 0.2 mg_{OC}/L NOM. Experiments were conducted in 0.025 M NaCl buffered to pH 7.4 with 0.002 M HEPES at 25 °C. Absorbance at 320 nm of samples containing PAH-DNP and NOM in buffer were referenced to PAH-DNP in buffer that had undergone the same centrifugation steps as the samples to eliminate any interference on the measurements by HEPES or free PAH polymer in solution.

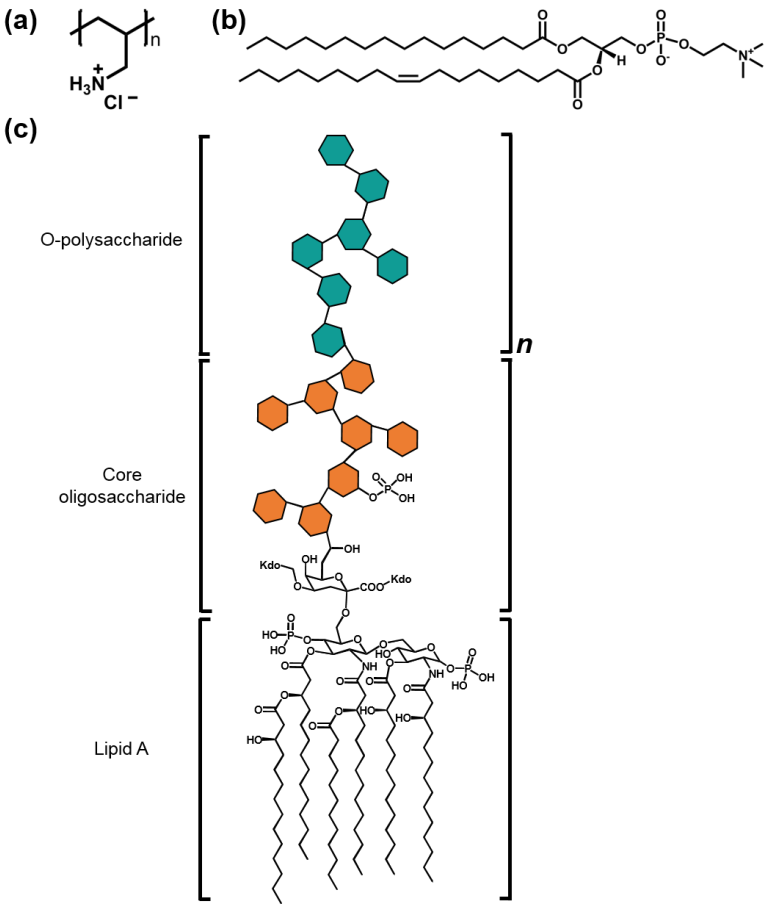

Figure A2.2. Chemical structures of (a) poly(allylamine HCl) used to functionalize the nanodiamond, (b) 1-palmitoyl-2-oleoyl-*sn*-glycero-3-phosphocholine (POPC), (c) the general structure of lipopolysaccharide (LPS) from a Gram-negative bacteria. Smooth LPS molecules contain Lipid A, core oligosaccharide, and an outermost O-polysaccharide chain, whereas rough LPS molecules lack this outermost domain. Lipid A is comprised of four to seven acyl chains (depending on bacterial species) connected to two phosphorylated glucosamine residues and anchors the molecule in the outer membrane. The core oligosaccharide is covalently linked to Lipid A, contains two or three 2-keto-3-deoxy-D-*manno*-octonate (Kdo) repeat units and is otherwise composed of 3-deoxy-D-mannooctulosonic acid, hexose, and heptose residues.[7-9] O-polysaccharide in smooth LPS is primarily made up of hexoses.

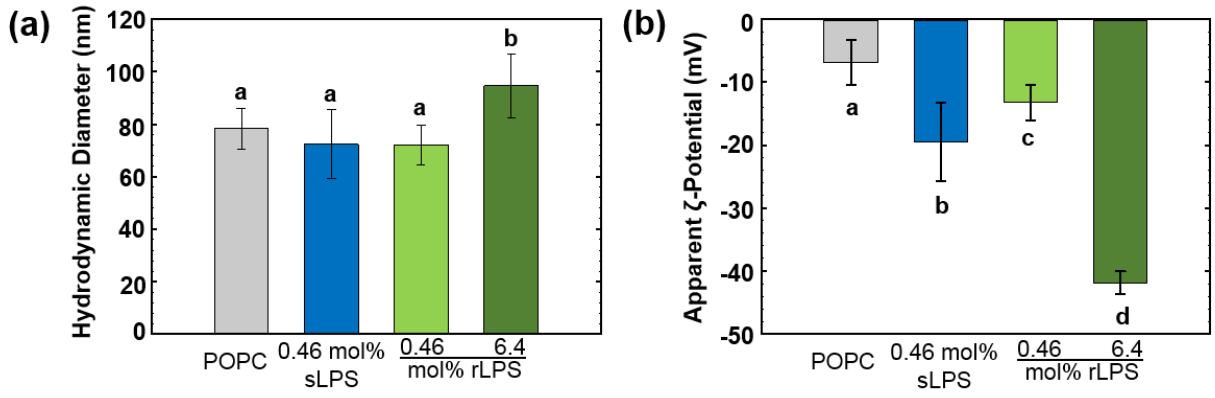

Figure A2.3. (a) Hydrodynamic diameters and (b) apparent ζ-potential values of phospholipid vesicles of POPC or POPC with the indicated mole percentage of either rough (green) or smooth (blue) LPS. Samples were 0.125 mg/mL concentration of vesicles in 0.002 M HEPES, 0.001 M NaCl, pH 7.4. Error bars represent one standard deviation of five measurements. Letters indicate significant differences within hydrodynamic diameters or apparent ζ potentials (p<0.001).

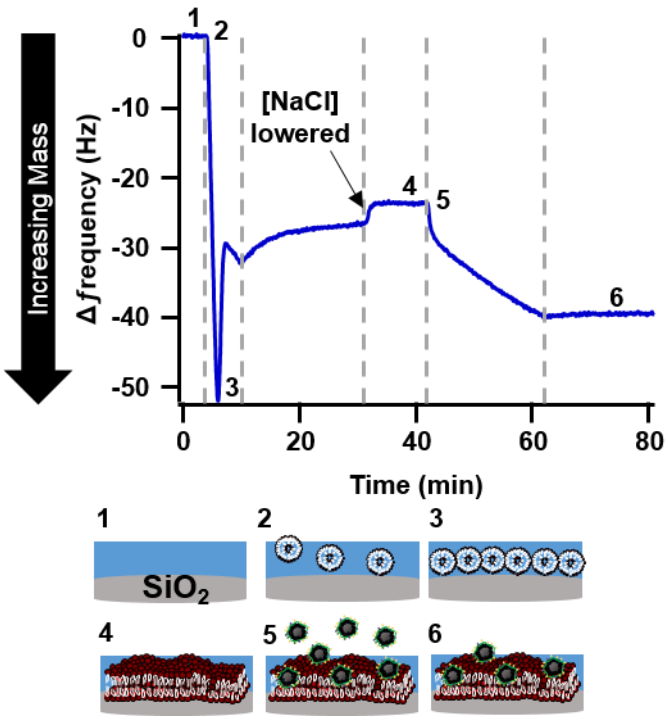

Figure A2.4. Quartz crystal microbalance enables *in situ* observation of the formation of a supported lipid bilayer and monitoring of the interaction between nanoparticles and these model bilayers. A typical experiment consists of the steps illustrated in the figure: (1) the SiO_2-coated sensor crystal is equilibrated in background solution (0.150 M NaCl buffered to pH 7.4 with 0.002 M HEPES); (2) once a stable baseline is reached, vesicles in the same solution are introduced causing a drop in frequency corresponding to an increase in mass; (3) a critical surface concentration of vesicles is attained, at which point the vesicles fuse and rupture releasing internalized water and a loss of mass; the bilayer is rinsed with vesicle-free solution; buffer (first 0.002 M HEPES, 0.150 M NaCl, pH 7.4, followed by 0.002 M HEPES, 0.025 M NaCl, pH 7.4) to remove any loosely bound vesicles; (4) once a stable baseline is achieved, (5) nanoparticles or nanoparticles + NOM in 0.002 M HEPES, 0.025 M NaCl, pH 7.4 are introduced for 20 min; and (6) the reversibility of these interactions are monitored by rinsing with NP/NP+NOM free solution. Dashed lines in the figure indicate a change in solution conditions.

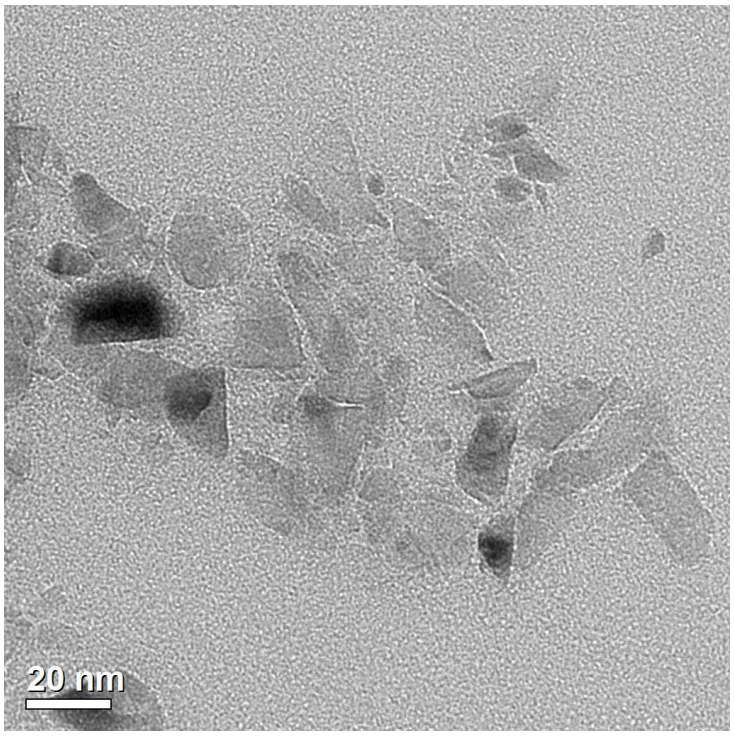

Figure A2.5. Transmission electron micrograph of PAH-DNP particles show a non-spherical morphology.

A2.5 References

1. Jacobson, K. H.; Gunsolus, I. L.; Kuech, T. R.; Troiano, J. M.; Melby, E. S.; Lohse, S. E.; Hu, D.; Chrisler, W. B.; Murphy, C. J.; Orr, G.; Geiger, F. M.; Haynes, C. L.; Pedersen, J. A. Lipopolysaccharide density and structure govern the extent and distance of nanoparticle interaction with actual and model bacterial outer membranes. *Environ. Sci. Technol.,* **2015,** *49,* 10642-10650.

2. Lohse, S. E.; Eller, J. R.; Sivapalan, S. T.; Plews, M. R.; Murphy, C. J. A simple millifluidic benchtop reactor system for the high throughput synthesis and functionalization of gold nanoparticles with different sizes and shapes. *ACS Nano,* **2013,** *7,* 4135-4150.

3. Bantan-Polak, T.; Kassai, M.; Grant, K. B. A comparison of fluorescamine and naphthalene-2,3-dicarboxaldehyde fluorogenic reagents for microplate-based detection of amino acids. *Anal. Biochem.,* **2001,** *297,* 128-136.

4. Noble, J. E.; Knight, A. E.; Reason, A. J.; Di Matola, A.; Bailey, M. J. A. A comparison of protein quantitation assays for biopharmaceutical applications. *Molecular Biotechnology,* **2007,** *37,* 99-111.

5. Qiu, T. A.; Torelli, M. D.; Vartanian, A. M.; Rackstraw, N. B.; Buchman, J. T.; Jacob, L. M.; Murphy, C. J.; Hamers, R. J.; Haynes, C. L. Quantification of free polyelectrolytes present in colloidal suspension, revealing a source of toxic responses for polyelectrolyte-wrapped gold nanoparticles. *Anal. Chem.,* **2017,** *89,* 1823-1830.

6. Zhang, M.; Soto-Rodríguez, J.; Chen, I. C.; Akbulut, M. Adsorption and removal dynamics of polymeric micellar nanocarriers loaded with a therapeutic agent on silica surfaces. *Soft Matter,* **2013,** *9,* 10155.

7. Kirschner, K. N.; Lins, R. D.; Maass, A.; Soares, T. A. A glycam-based force field for simulations of lipopolysaccharide membranes: Parametrization and validation. *J. Chem. Theory Comput.,* **2012,** *8,* 4719-4731.

8. Clifton, L. A.; Holt, S. A.; Hughes, A. V.; Daulton, E. L.; Arunmanee, W.; Heinrich, F.; Khalid, S.; Jefferies, D.; Charlton, T. R.; Webster, J. R.; Kinane, C. J.; Lakey, J. H. An accurate *in vitro* model of the *E. coli* envelope. *Angew. Chem. Int. Ed.,* **2015,** *54,* 11952-11955.

9. Nikaido, H. Molecular basis of bacterial outer membrane permeability revisited. *Microbiol. Molecular Biol. Rev.,* **2003,** *67,* 593-656.

A3. Supporting Information for Chapter 3: Quaternary-Amine Terminated Quantum Dots Induce Structural Changes to Supported Lipid Bilayers

A.3.1 Supplemental Figures

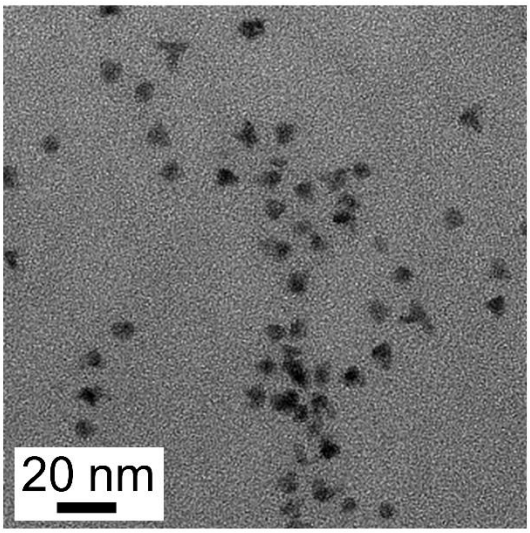

Figure A3.1. Representative transmission electron micrograph of the PDDA-QDs used in this study.

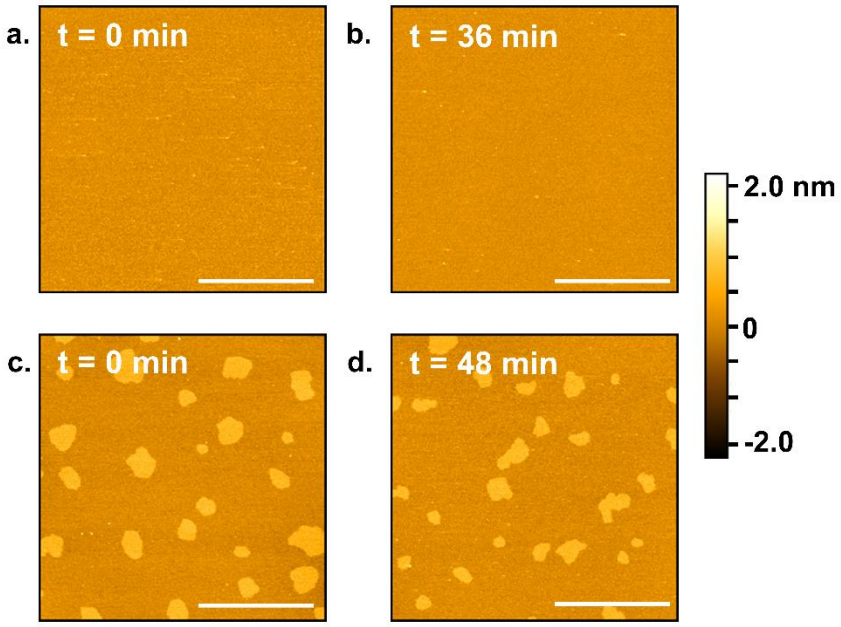

Figure A3.2. Time lapse images of DOPC bilayer (a) before and (b) after treatment with buffer instead of PDDA-QDs show that there are no structural changes observed over time. Time lapse images of 60/20/20 mol% DOPC/SM/Chol bilayer (c) before and (d) after treatment with buffer instead of PDDA-QDs show that there are no structural changes observed over time. The bilayer imaged later in time is not the same exact spot that the beginning image was taken at; however, multiple spots were analyzed and no features similar to those seen upon interaction with PDDA-QDs were observed. Scale bars are 2 μm. Z scale applies to all images. The time on each image indicates how much time the bilayer had been introduced to the QD-free buffer rinse.

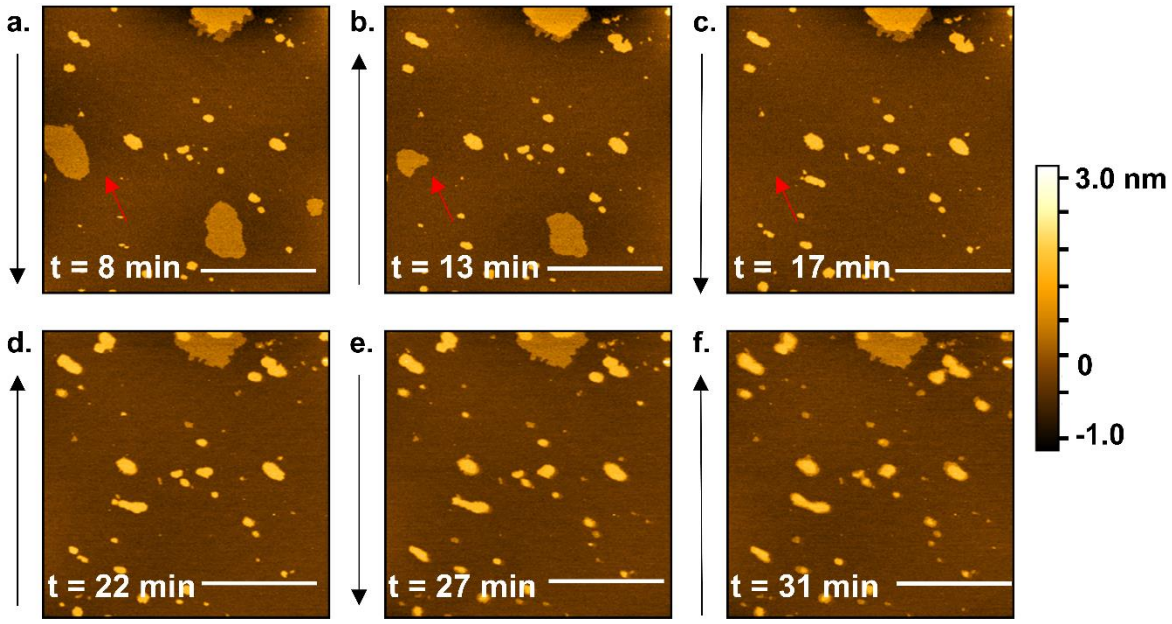

Figure A3.3. Time lapse images of 60/20/20 mol% DOPC/SM/Chol bilayer after exposure to 1 wt% PDDA polymer (average M_w 200,000-350,000 Da). The red arrow is to guide the reader's eye to the disappearance of the phase-segregated domains. Black arrows indicate the scan direction of the image. Scale bars are all 2 μm. Z scale applies to all images. The time on each image indicates how much time the bilayer had been introduced to the polymer prior to the image being captured.

A4. Supporting Information for Chapter 4: Atomic Force Microscopy of Phase-segregated Domain Bilayers: Considerations for Examining Bilayers across Multiple Techniques

A4.1. Matlab code for analysis for force-distance curves by AFM

The following Matlab code was written to analyze the breakthrough force from text files of force as a function of distance. In the section to follow, the Matlab code is given in Courier new font, whereas the annotation of the code is listed above the commands. The code without annotation is at the end.

The folder where the text files are located was designated ("folderName"):

```
folderName = 'VO256_PS050356'
```

In this case "VO256_PS050356" was the name of the file where the text files to be analyzed were saved. Force-distance curves were exported as text files from Nanoscope Analysis 1.8 (Bruker). This was done by selecting the files of interest in the browse data, right clicking, and saving the files as ACSII files. Channel 1 (deflection error) and channel 4 (height sensor) were saved (Note: ensure that "display units" and "extend" are checked). The output unit for force is picoNewtons.

A file name where the values of the force breakthrough are to be saved was specified ("dataname"). In this case "Forcebreakthroughoutput" was used as the final name of the text file that listed both the file name of the original text file (of force vs. distance) and the associated breakthrough force:

```
dataName = 'ForceBreakthroughoutput';
```

A list of file names (text files of force vs. distance curves) was generated from the text files found in the folder designated by "folderName":

```
fileList = dir(folderName);
```

The last number in the file list was specified to give the number of iterations for the for loop:

```
last = numel(fileList);
```

A cell array was preallocated to fill the output text file with the corresponding text file name (of force vs. distance) and the force breakthrough value:

```
peaks = cell(last,2);
```

Below starts the for loop to calculate the force breakthrough values. First a number of iterations of the for loop is set, where “3” is the first entry and “last” is the last entry:

```
for j = 3:last
```

The data from the file list associated with the file name was read:

```
C = importdata([folderName,'\',fileList(j).name]);
```

The x data (displacement in nanometers from the force-distance curves) were read from the text file (column 3):

```
nm = C.data(:,3);
```

The y data (force in picoNewtons from the force-distance curves in the Bruker files) were read from the text file (column 2):

```
pN = C.data(:,2);
```

A plot of force vs. distance can be generated, if desired:

```
plot(nm,pN)
```

One half of the points in the file (which were part of the flat baseline where no tip-sample interaction was observed) were used to estimate the background in the curves. The total number of ordered pairs in the file was designated as “length”:

```
length = numel(pN);
```

and the number of ordered pairs used in the baseline correction was given as “center”:

```
center = round(1*length/2);
```

The flat portion of the curve from the first point to “center” was fit with a first-order polynomial:

```
f = fit(nm(1:center),pN(1:center),'poly1');
```

The background level for the y values (force) associated with each inputted x value (distance) was determined:

```
background = f(nm);
```

The background was subtracted from the y (force) values above and the variable “pN” was renamed to be the force value with the background subtracted:

```
pN = pN - background;
```

The first derivative of the force value was found:

```
derv = diff(pN);
```

If desired, the first derivative can be plotted:

```
plot(derv);
```

The second derivative was then taken:

```
secDerv = diff(derv);
```

Again, if desired the second derivative can also be plotted:

```
plot(secDerv);
```

The minimum value in the second derivative (“M”) was determined; “I” is the index of the minimum values and indicates where the minimum of the second derivate is located within the vector:

```
[M,I] = min(secDerv);
```

“I” is located close to the local maximum of force values, which is equal to the desired force breakthrough value (“Forceb”):

```
Forceb = max(pN(I-2:I+2));
```

The Bruker file name was inputted into the first column and the “jth” row of our cell array “peaks”:

```
peaks(j,1) = cellstr(fileList(j).name);
```

and the maximum breakthrough force was inputted into the second column and the “jth” row of our cell array “peaks”:

```
peaks(j,2) = num2cell(Forceb);
```

and the for loop was ended:

```
end
```

A table was generated from the cell array:

```
peakTable = cell2table(peaks);
```

and finally turn that table was converted into a text file:

```
writetable(peakTable,dataName)
```

The non-annotated code can be found below for direct copy into Matlab:

```
folderName = 'VO256_PS050356';
dataName = 'ForceBreakthroughoutput';
fileList = dir(folderName);
last = numel(fileList);
peaks = cell(last,2);
      for j = 3:last
      C = importdata([folderName,'\',fileList(j).name]);
      nm = C.data(:,3);
      pN = C.data(:,2);
      plot(nm,pN)
      length = numel(pN);
      center = round(1*length/2);
      f = fit(nm(1:center),pN(1:center),'poly1');
      background = f(nm);
      pN = pN - background;
      derv = diff(pN);
      plot(derv);
      secDerv = diff(derv);
      plot(secDerv);
      [M,I] = min(secDerv);
      Forceb = max(pN(I-2:I+2));
      peaks(j,1) = cellstr(fileList(j).name);
      peaks(j,2) = num2cell(Forceb);
      end
peakTable = cell2table(peaks);
writetable(peakTable,dataName)
```

A4.2. Supplemental Figures

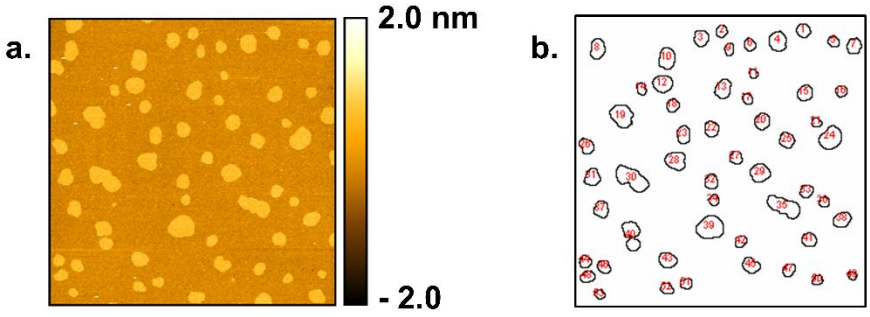

Figure A4.1. (a) atomic force microscopy image shown in Figure 4.2c on mica and (b) corresponding outlined mask creating using FIJI to determine the average perimeter, area, and fractional coverage by phase-segregated domains.

A.7. Contributions to other work

Throughout my time in graduate school with the Center for Sustainable Nanotechnology I have had the opportunity to contribute to various collaborative projects with my different groups across the country. Below I highlight my contributions to various published works and manuscripts in preparation.

A.7.1. Published work

Pham, S.N.*, Kuether, J.*, Gallagher, M., Tapia Hernandez, R.*, Williams, D.N., Zhi, B., **Mensch, A.C.,** Hamers, R.J., Rosenzweig, Z., Fairbrother, H., Krause, M.O.P, Feng, Z.V., Haynes, C.L. Carbon dots: a modular activity to teach fluorescence and nanotechnology at multiple levels, *J. Chem. Ed.*, **2017**, *94*, 1143-1149.

The goal of this work was to introduce the synthesis and characterization of nanosize carbon dots at various educational levels – from high school to upper-division college level. This work was initially presented in the form of a blog post for Sustainable-nano.com. As an editor of the blog, I received the draft and quickly realized the greater potential of the activity. I proposed that we reformat the blog post into a manuscript and in doing so made intellectual contribution in the form of helping to draft and organize the ideas into a manuscript was well as providing edits and feedback for subsequent drafts.

Hang, M.N., Gunsolus, I.L., Wayland, H.*, Melby, E.S., **Mensch, A.C.**, Hurley, K.R., Pedersen, J.A., Haynes, C.L., Hamers, R.J. Impact of nanoscale lithium nickel manganese cobalt oxide (NMC) on the bacterium *Shewanella oneidensis* MR-1. *Chemistry of Materials.* **2016**, *28* (4), 1092-1100.

The goal of this work was to understand to study the impact of nanoscale lithium nickel manganese cobalt oxide (NMC), a widely used cathode material in lithium-ion batteries, on the

Gram-negative bacterium *Shewanella oneidensis* MR-1. The major finding of this work was that incongruent dissolution of NMC nanomaterials led to toxicity to *S. oneidensis.* To fully understand these interactions, the nanosheets needed to be characterized with various techniques. The sheet-like nature of these materials, made characterization more difficult. I contributed to the characterization of these materials by performing atomic force microscopy imaging and subsequent size analysis. This lead to size characterization of the nanosheets being 0.88 ± 0.61 nm in height as determined by height analysis across 125 individual nanosheets. A representative image and line scan were published as supporting information in this manuscript and are summarized in Figure A7.1.

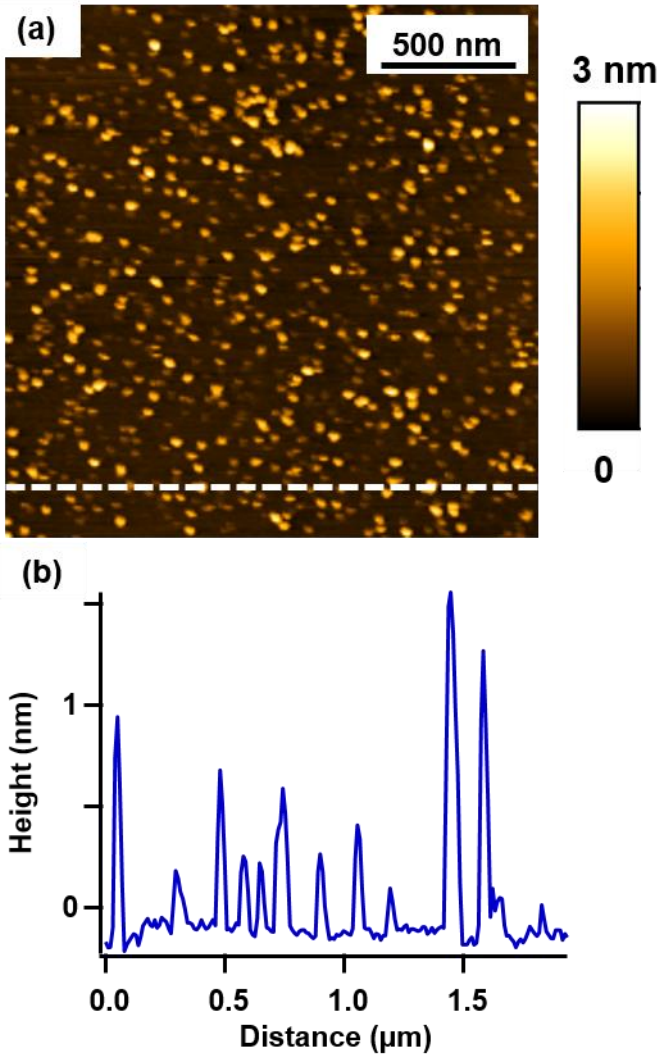

Figure A7.1. (a) Representative AFM image of NMC nanoparticles deposited on freshly cleaved mica. (b) Representative AFM height profile measured across individual NMC nanosheets.

Melby, E.S., **Mensch, A.C.**, Lohse, S.E., Hu, D., Orr, G., Murphy, C.J., Hamers, R.J., Pedersen, J.A. Formation of supported lipid bilayers containing phase-segregated domains and their interaction with gold nanoparticles. *Environmental Science: Nano.* **2016**, *3*, 45-55.

The goal of this work was to study the interactions between gold nanoparticles, functionalized with cationic or anionic ligands, and supported lipid membranes containing phase-segregated domains. We varied the composition of the bilayers by using different molar ratios of DOPC, cholesterol, and sphingomyelin. This was the first demonstration of these model bilayer systems being formed on quartz crystal microbalance with dissipation monitoring sensors, which have a silica coating on them. To provide supporting evidence that these membranes containing phase-segregated domain formed on silica surfaces I provided complementary atomic force microscopy imaging and analysis of membranes with and without phase-segregated domains on ultraflat SiO_2 surfaces. I observed as the amount of cholesterol and sphingomyelin were increased the amount of observed phase-segregated domains also increased. We quantified the fractional coverage of the domains by fitting histogram data of height distributions to a Gaussian distribution and dividing the area of the higher height distribution (the domains) by the total area of the image. I provided two figures, along with the appropriate description of methods and interpretation of data as contribution to this work. This work also provided the basis for bilayers characterized and investigated in Chapters 3 and 4 of this thesis.

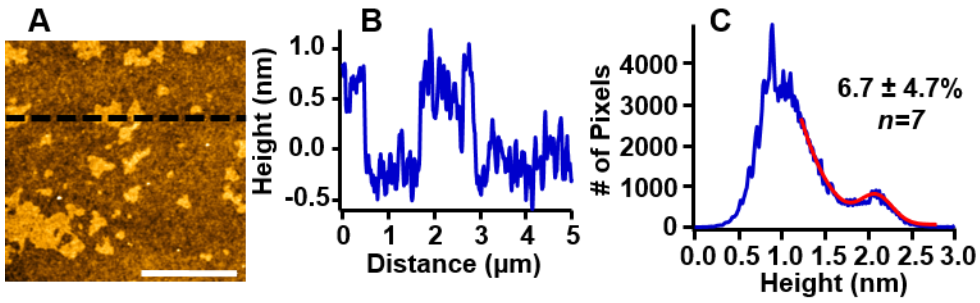

Figure A7.2. Atomic force microscopy confirms (A) the presence of distinct L_o and L_d phases with (B) the expected ~1 nm height difference between phases in a supported lipid bilayer consisting of 60/20/20 mol% DOPC/SM/Chol. (C) The coverage of L_o domains was determined by fitting the AFM height distribution. Scale bar is 2 μm. AFM images of other compositions investigated are provided in Figure A7.3.

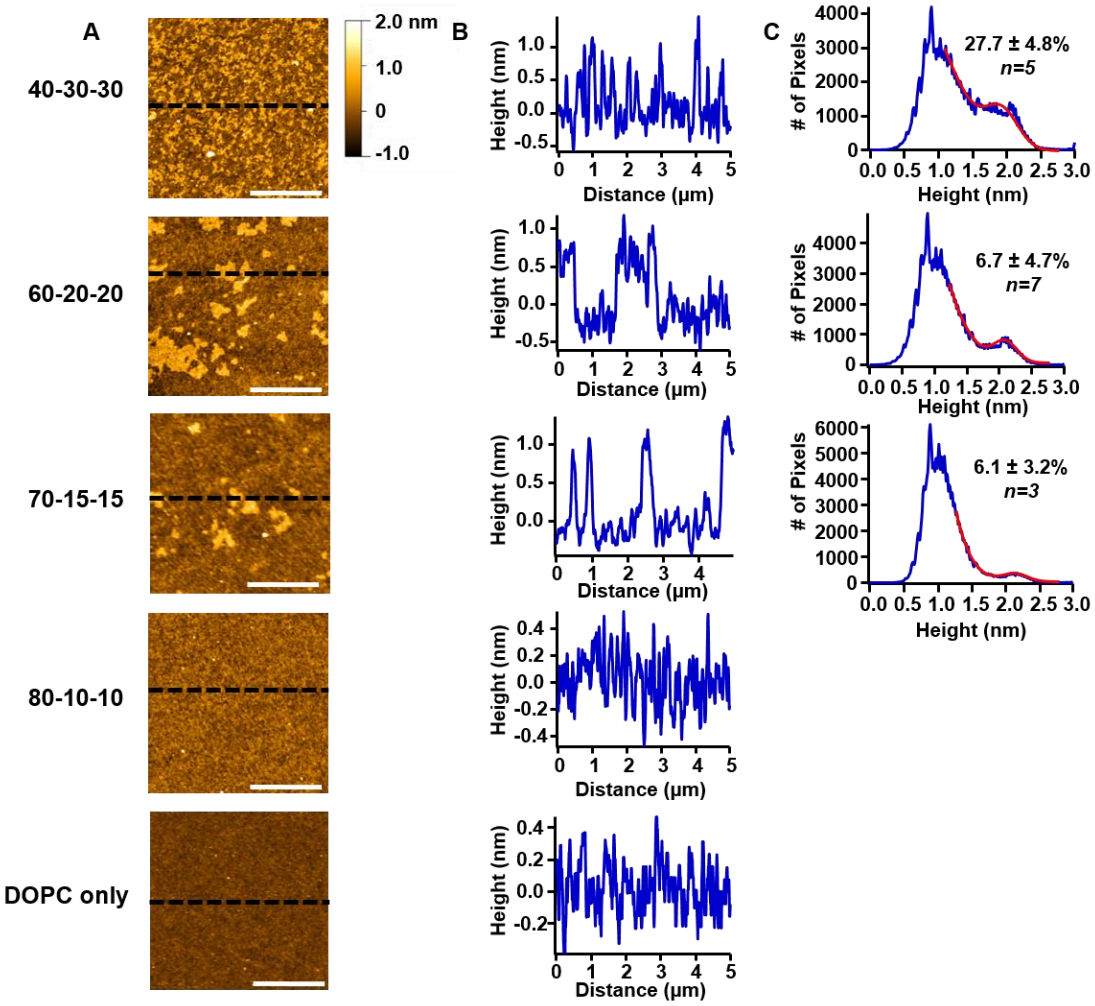

Figure A7.3. (A) Tapping mode AFM images of supported lipid bilayers formed from the indicated molar ratios of DOPC, SM, and Chol. (B) Representative line scans next to the images show the height difference between L_o and L_d phases to be ~1 nm. (C) Histograms showing the two distinct height regions. Fractional coverage estimates based on fitting the L_o domain peak at (~2 nm) in the histogram and determining a fractional area coverage are listed for the 40/30/30, 60/20/20, and 70/15/15 mol% DOPC/SM/Chol combinations. No phase-segregated domains were visible at 80/10/10 or pure DOPC composition. Scare bars are 2 μm and the z-axis applies to all images.

Troiano, J.M., Olenick, L.L, Kuech, T.R., Melby, E.M., Hu, D., Lohse, S.E., **Mensch, A.C.**, Dogangun, M., Vartanian, A.M., Torelli, M.D., Ehimiaghe, E.*, Walter, S.R., Anderton, C.R., Zhu, Z., Wang, H., Orr, G., Murphy, C.J., Hamers, R.J., Pedersen, J.A., Geiger, F.M. Direct probes of 4 nm diameter gold nanoparticles interacting with supported lipid bilayers. *Journal of Physical Chemistry C*. **2015**, *119*, 534-546.

The goal of this work was to use complementary analytical methods, including second harmonic generation spectroscopy, sum frequency generation spectroscopy, quartz crystal microbalance with dissipation, fluorescence spectroscopy, nuclear magnetic resonance spectroscopy, X-ray photoelectron spectroscopy, time-of-flight secondary ion mass spectrometry, and atomic force microscopy to investigate the interactions between supported lipid bilayers and gold nanoparticles. We showed that both anionic and cationic gold nanoparticles interact irreversibly with pure DOPC and 9:1 mixtures of DOPC:DOTAP membranes. I contributed to this work by optimizing atomic force microscopy under flow conditions to corroborate the results demonstrated by the other techniques listed. By matching the conditions of the other techniques we were able to make stronger arguments for our observations and conclusions. I contributed AFM images to two figures in the main text of the manuscript along with the methods and interpretation associated with them.

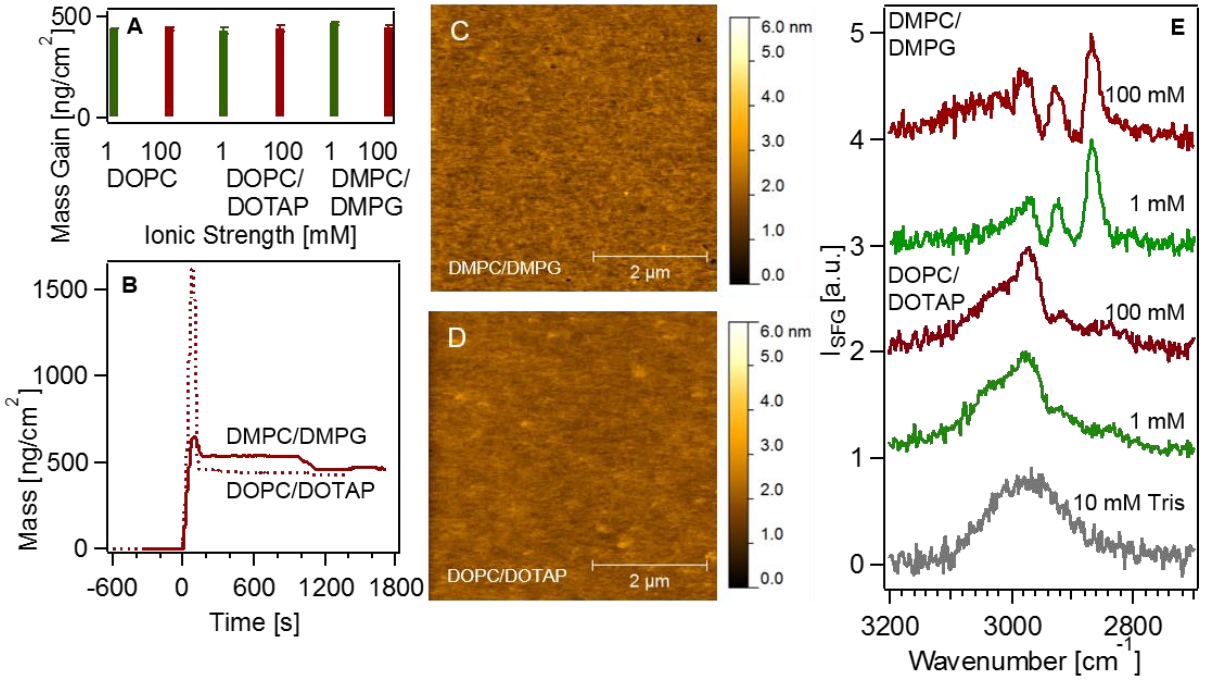

Figure A7.4. (A) Total acoustic mass gain, evaluated by QCM-D, for conditions indicated. (B) Formation of supported lipid bilayers from vesicles formed from 9:1 mixtures of DMPC/DMPG (solid line) and DOPC/DOTAP (dashed line) probed by QCM-D at 0.1 M NaCl. The small decrease in mass in the 9:1 DMPC:DMPG bilayer commencing at 1000 s is most likely due to the removal of loosely attached intact vesicles during rinsing with Ca^{2+}-free solution. (C-D) AFM (5×5 µm^2) images of bilayers formed from DMPC/DMPG and DOPC/DOTAP at 0.1 M NaCl. (E) Normalized ssp-polarized SFG spectra of supported lipid bilayers at pH 7.4 and in the presence of 0.01 M Tris (gray) for 0.001 (green) and 0.1 (red) M NaCl using vesicles formed from 9:1 DMPC/DMPG (top pair) and DOPC/DOTAP (bottom pair) mixtures.

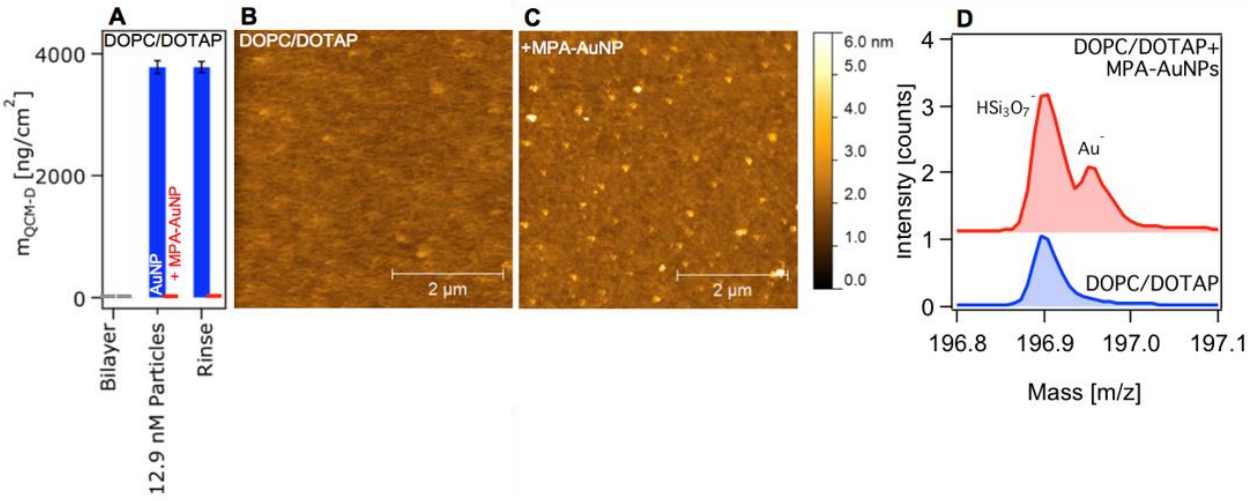

Figure A7.5. (A) Acoustic mass gains determined by QCM-D upon 60 min exposure of a supported lipid bilayer formed from a 9:1 mixture of DOPC and DOTAP to 12.8 nM positively charged PAH-coated and negatively charged MPA-coated 4-nm spherical AuNPs in 0.01 M Tris buffer and 0.1 M NaCl at pH 7.4. (B-C) Topography image of bilayers formed from a 9:1 mixture of DOPC and DOTAP in 0.01 M Tris, 0.1 M NaCl, pH 7.4 on an ultra-flat thermal SiO_2 substrate wafer before (B) and after (C) exposure to MPA-AuNPs (10 nM). Images from the same experiment carried out on a freshly prepared bilayer and adjusted to the same scale. (D) Normalized ToF-SIMS spectra of 9:1 DOPC:DOTAP bilayer before (bottom) and after (top) interaction with 1 nM MPA-AuNPs at room temperature and in 0.1 M NaCl and pH 7.4 (0.01 M Tris buffer) and subsequently rinsed with buffer. Bilayer samples were prepared in and then removed from the flow cell following rinsing and allowed to dry prior to analysis.

A.7.2 Work in preparation

Kuech, T. R.; Torelli, M. D.; Melby, E. S.; **Mensch, A. C**.; Orr, G.; Hamers, R. J.; Pedersen, J. A**.** Interaction of cationic polymer-functionalized diamond nanoparticles with supported lipid bilayers, *in preparation*.

The goal of this work was to understand how changing the cationic polymeric wrapping on nanodiamond impacted the subsequent interactions with supported lipid bilayers of various composition. The main technique used to study these interactions was quartz crystal microbalance with dissipation monitoring. However, I also provided complementary atomic force microscopy imaging of the bilayers before and after interaction with functionalized nanodiamond to provide a visual of the structural impact of these nanomaterials. This contribution took the form of an image in the main text in addition to the necessary methods and interpretation of the data.

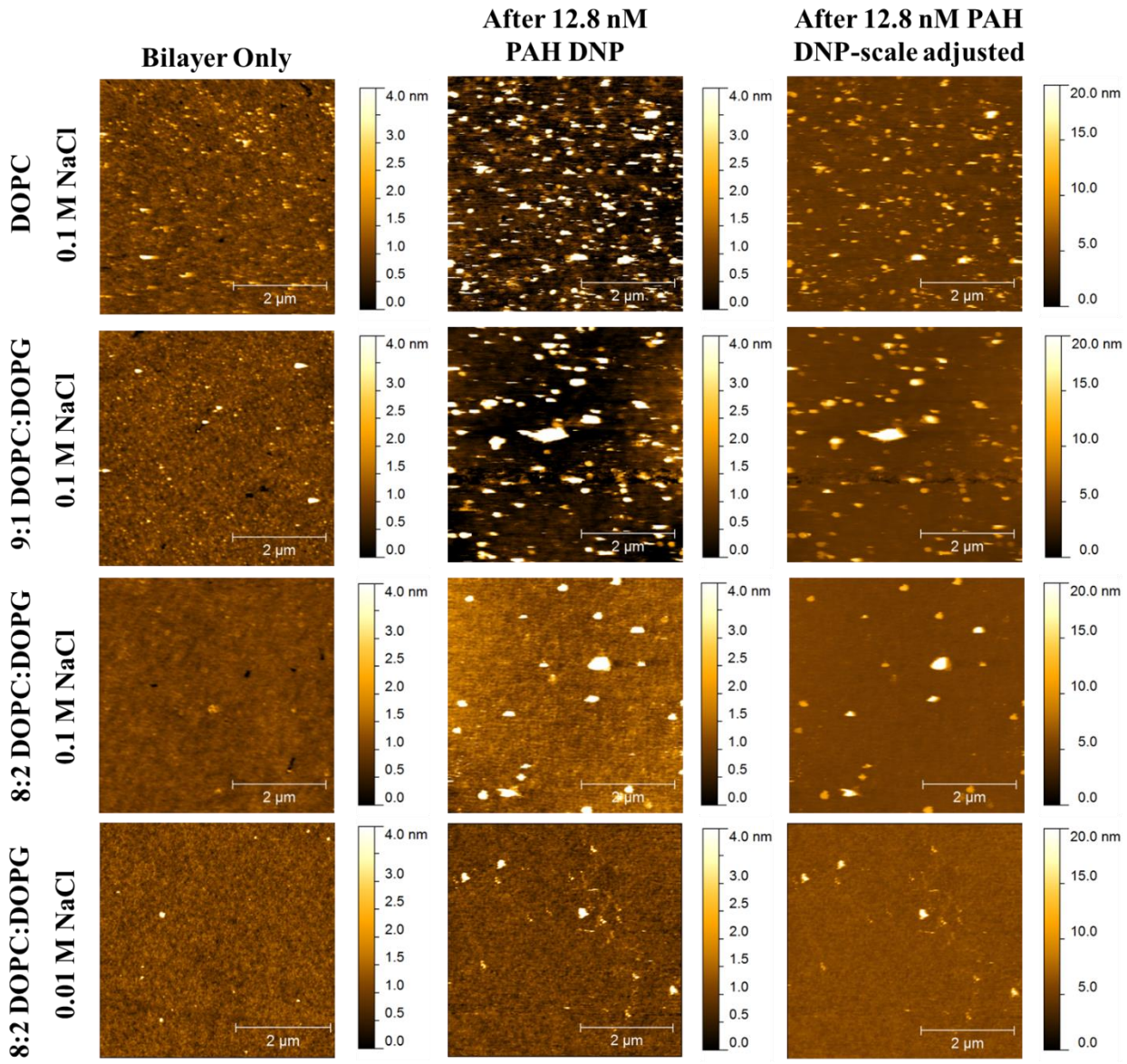

Figure A7.6. AFM of bilayers before and after exposure to PAH-ND with increasing DOPG concentration. Bilayers were imaged after 20 min of PAH-ND attachment. The last row of images is for 8:2 DOPC:DOPG at 0.01 M NaCl. The amount of particles attached to bilayers decreases as DOPG concentration increases, while the 8:2 DOPC:DOPG image at 0.01 M NaCl shows further reduced attachment. AFM images were taken at the same spot on each sample prior to particle introduction and after particle attachment and rinsing. Measurements were repeated in triplicate for all bilayers imaged.

Torelli, M. D.; Putans, R. A.; **Mensch, A. C.**; Pedersen, J. A.; Hamers, R. J. Effects of protein charge and material conductivity on non-specific binding of proteins to oligo(ethylene glycol)-functionalized surfaces. *ACS Appl. Mater. Interfaces.* (revision request 01/05/17)

The goal of this work was to investigate how the charge of proteins and the electronic properties of two materials (gold and diamond) contribute to surfaces resisting the non-specific binding of proteins. To do this both gold and diamond were functionalized with hexaethylene glycol and the binding of three different small proteins of various net charge was quantified. To ensure that we had a starting monolayer on the diamond surface, which are less well studied than monolayers on gold, I conducted AFM "nano-shaving" experiments on the diamond functionalized with hexaethylene glycol and verified that a monolayer was present on the diamond. We also wanted to compare the starting roughness of the two different substrates, so RMS measurements were made using AFM. These measurements took the form of an image in the supporting information of the manuscript.

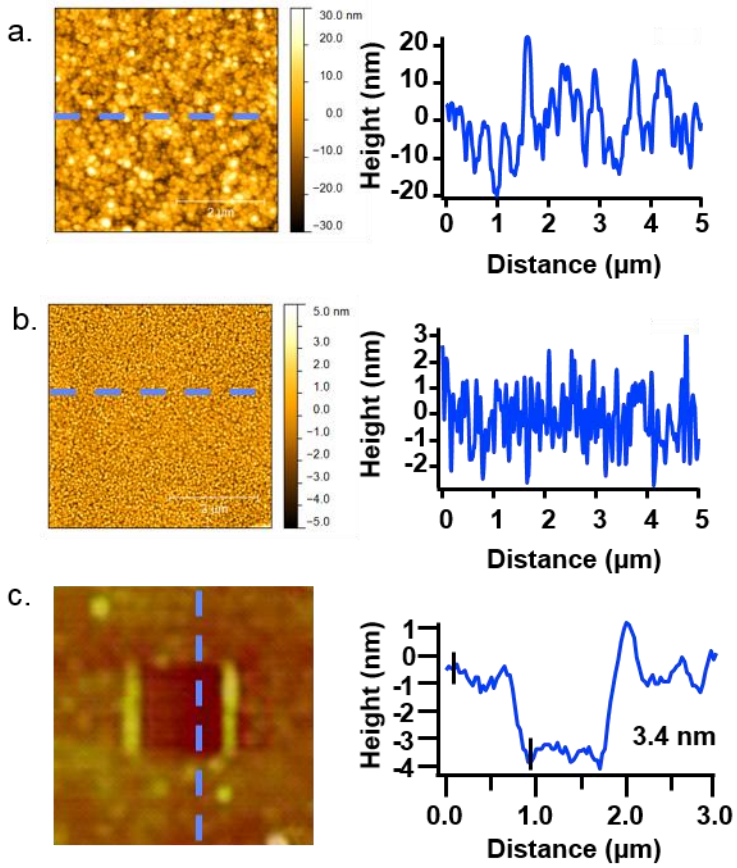

Figure A7.7. AFM analysis of surfaces prior to use. a) Ultrananocrystalline diamond thin film (RMS = 7.63 nm), b) Evaporated gold on Ti adhesion layer (RMS = 1.35 nm). After functionalization c) "nanoshaving" experiment on EG_6-OH functionalized ultrananocrystalline diamond (monolayer thickness = 3.4 nm).

Zhi, B.; Gallagher, M. J.; Frank, B. P.; Lyons, T. Y.; Qui, T. A.; Da, J.; **Mensch, A. C.**; Hamers, R. J.; Rosenzweig, Z.; Fairbrother, D. H.; Haynes, C. L. Investigation of phosphorous doping effect on polymeric carbon dots: fluorescence, photo stability and environmental impact, *in preparation*.

The goal of this work is to understand the impact that phosphorus doping has on the properties of nitrogen-doped polymeric carbon dots, specifically their fluorescence behavior, photostability, and toxicity towards the bacterium *Shewanella oneidensis*. To fully understand the properties of these materials they needed to be thoroughly characterized. I contributed to the size analysis of the particles using atomic force microscopy to corroborate size analysis done by transmission electron microscopy. Particularly, AFM can provide a height of the particles, whereas TEM is only two dimensions. We found that the citric acid carbon dots had a height of ~3.7 nm, whereas the malic acid carbon dots had a height of 3.5 nm. This information took the form of a figure in the supporting information of the manuscript in preparation.

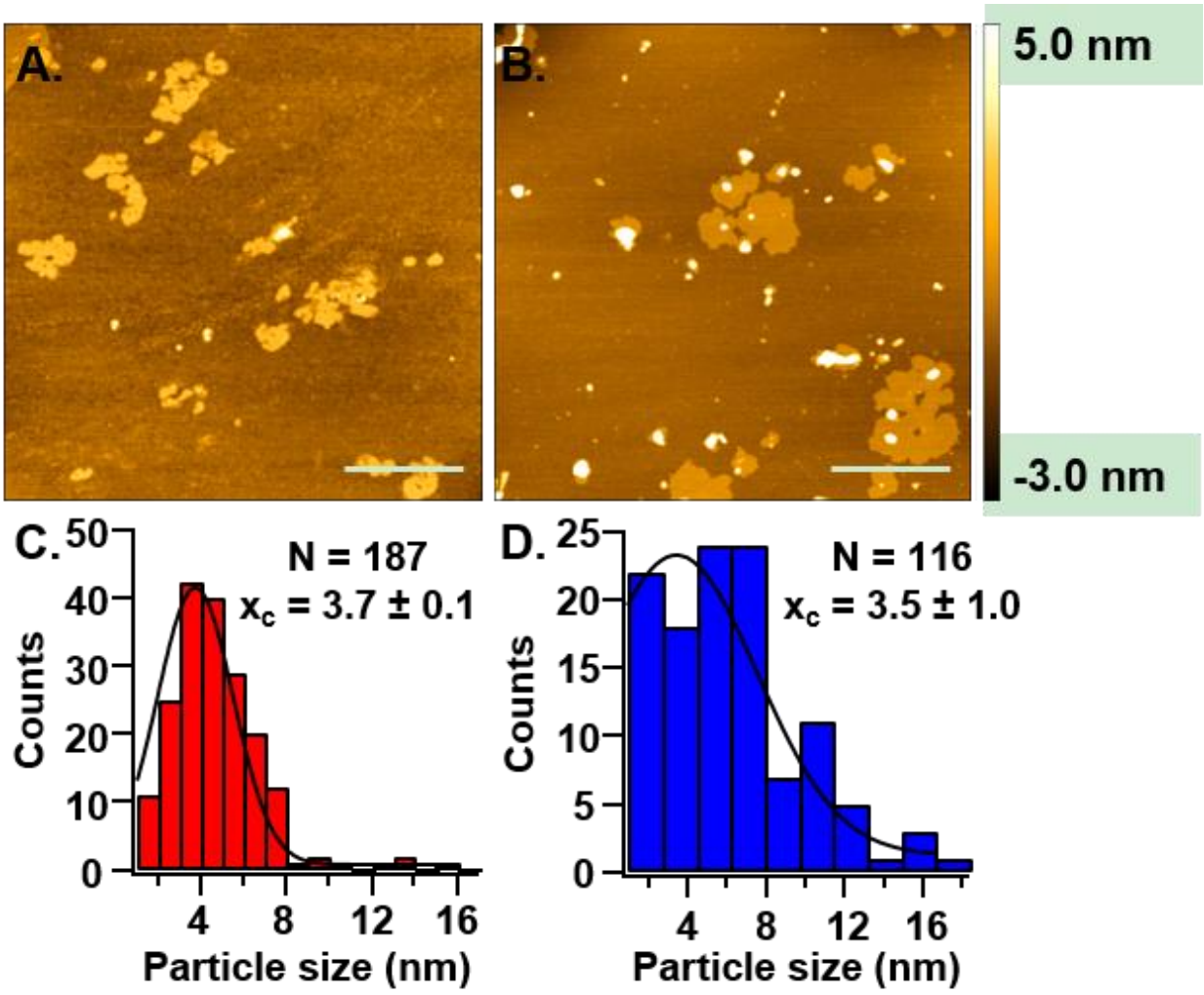

Figure A7.8. AFM images of (a) CACDs and (b) MACDs, particle height distribution of (c) CACDs and (d) MACDs

Olenick, L. L.; Troiano, J. M.; Vartanian, A. M.; Melby, E. S.; **Mensch, A. C.**; Zhang, L.; Qiu, T. A.; Bozich, J. S.; Lohse, S. E.; Zhang, X.; Kuech, T. R.; Millevolte, A.; Gunsolus, I. L.; McGeachy, A. C.; Dongangun, M.; Hu, D.; Walter, S. R.; Mohaimani, A.; Schmoldt, A.; Torelli, M. D.; Hurley, K. R.; Dalluge, J.; Chong, G.; Feng, Z. V.; Haynes, C. L.; Hamers, R. J.; Pedersen, J. A.; Cui, Q.; Hernandex, R.; Klaper, R. D.; Orr, G.; Murphy, C. J.; Geiger, F. M. Lipid corona formation from nanoparticle interactions with membranes, *in preparation.*

The goal of this work was to investigate the acquisition of a lipid corona upon interaction between polycationic nanoparticles and supported and suspended lipid bilayers. This work was extended to include biological assays to demonstrate how the removal of lipids from a membrane may impact the survival of organisms. This work contained a large array of experimental and computational analytical techniques to probe the acquisition of a lipid corona. I conducted single molecule tracking experiments at Pacific Northwest National Laboratory in collaboration with Julianne Troiano, Eric Melby, Dehong Hu, and Galya Orr to contribute to this work. We showed, by single molecule fluorescence microscopy, that cationic nanoparticles changed the fluidity of supported lipid bilayers by tracking the diffusion of individual lipid molecules. The diffusion coefficient of individual lipids increased from 0.0095 ± 0.0062 to 0.035 ± 0.011 $\mu m^2 s^{-1}$, after interaction with PAH-AuNPs. This work along with the other analytical techniques contributed to the idea of a "lipid corona." It is presented in the draft of the manuscript as a figure of single molecule trajectories before and after nanoparticle exposure.

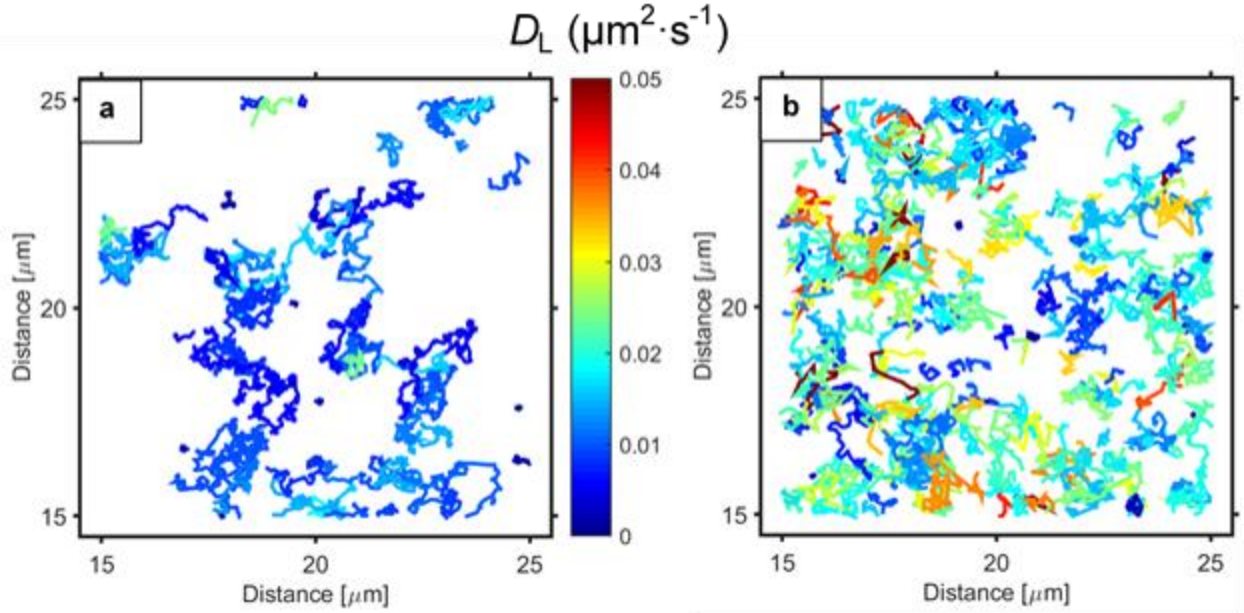

Figure A7.9. Lipid diffusion is altered by interaction with PAH-wrapped nanoparticles. Trajectories of individual Atto 647N DOPE lipid molecules in a 9:1 DMPC:DMPG bilayer. Reconstructed lipid trajectories before (a) and after (b) the addition of 1 nM PAH-AuNPs. Colors indicate lateral diffusion coefficients [D_L, μm^{2}s^{-1}] for individual lipid molecules.